DISSOLUTION RATES IN THE WAKE OF A WELDING BACKUP RING

by

GERMANO DE FREITAS

B.S., Universidade de São Paulo, Brazil
(1975)

Submitted to the Department of
Mechanical Engineering
in Partial Fulfillment of the
Requirements for the
Degree of

MECHANICAL ENGINEER

at the

MASSACHUSETTS INSTITUTE OF TECHNOLOGY

February 1986

Signature of Author _____
Department of Mechanical Engineering
January 6,1986

Certified by _____
Peter Griffith
Thesis Supervisor

Accepted by _____
Ain Ants Sonin
Chairman, Departmental Committee on Graduate Studies

DISSOLUTION RATES IN THE WAKE

OF A WELDING BACKUP RING

by

Germano de Freitas

Submitted to the Department of Mechanical Engineering
on January 6,1986 in partial fulfillment of the
requirements for the Degree of Mechanical Engineer

ABSTRACT

Failures in equipment used for steam generation in many nuclear power plants are responsible for two kinds of problems: a decrease in the safety operational conditions and an increase in the expenses caused by unscheduled plant outages. Among several types of problems that can occur in a power plant there is one which can be found either in the simplest conventional thermo-electric station or in the most sophisticated nuclear power plant: the problem originated by oxide removal in steam pipelines. Analyzing the data of corrosive-erosive wear of low carbon steel piplines of nuclear power plants owned by Northeast Utilities we can see that the locations which present the greatest metal removal rates are the bends and the wake of welding backup rings. This work consists of an experimental study to measure the mass transfer coefficient variation in a planar model simulated fitting, pipe, and backup ring made of plaster-of-paris. A two-phase air-water flow rig was built and tests were conducted at air velocities of 100, 125, and 150 ft/s with water flow rates in the range from 490 to 940 ml/min. Data obtained show four distinct mass transfer coefficient regions around the groove and approximate quantitative relations between the straight part mass transfer coefficient and the enhanced coefficients of the groove regions are suggested. The comparison between the average mass transfer coefficient obtained from the experiments with theoretical values calculated considering the flow conditions and using the Kunz and Yerazunis theory shows that good agreement exists between the experimental values and the theoretical predictions.

Thesis Supervisor: Peter Griffith
Title: Professor of Mechanical Engineering

ACKNOWLEDGEMENTS

I am happy because now it is time to say "thank you", but unfortunately it is also time to say "good bye" for many of those people who greatly helped me during this part of my life.

First of all, I have to thank God for the grace He has given me to carry out this work and, better than this, for the pleasure of meeting all these wonderful people in my way.

I wish to express my sincere gratitude and appreciation to my advisor, Professor Peter Griffith, whose guidance, encouragement, broad knowledge and experience have made the time of this research a most invaluable learning experience.

I would like to deeply thank the invaluable advice, incentive, and support given by two big friends, Othon L.P. da Silva and Ari Raynsford, who helped me in so many ways to overcome problems and difficulties I have had to face.

I would also express my gratitude to Mrs. Sandra Tepper for all the support and advice she has given me since my first days here until the present time, helping me with the typing of my research.

My sincere thanks to my officemates, Richard G. Keck, Keith M. Gawlik and Katsuhiro Yamamoto for their helpful suggestions, advice and, most of all, their friendship.

A special thanks to a special person who, even far away, has given me very good support and encouragement. Thank you, Dona Luzia, thank you very much for your great help.

Finally, the financial support provided by the Brazilian Navy and the Northeast Utilities is greatfully acknowledged.

To you,

because you have given me a lot of things I need: you have given me your love during all these years we have been together , peace of mind when I was in trouble , tenderness when I was nervous , material support taking care of our kids , our home , our health , and spiritual support as only you know how to give us . Without you , your help , your company, I know that it would not have been possible to me to finish my studies and obtain this degree . Now the work is done , the task is finished , but I will always be grateful for everything you did .

For all that you have given me , you deserve that I dedicate this work to you , but I wish to do this for another reason: above all, I dedicate this work to you , Vilminha , because I love you .

TABLE OF CONTENTS

List of Figures

Figure Page

CHAPTER 1

INTRODUCTION

1.1 Statement of The Problem

Many of the failures that occur in equipment used for steam generation in nuclear and fossil power plants are due to the phenomenon of material removal from the internal parts of such equipment. This material removal is often a consequence of an erosive-corrosive process experienced by parts made of low carbon steel operating under the usual temperature and pressure conditions found in a nuclear utility. As reported by Griffith et al. [16] some bends that had an expected lifetime of thirty years have had to be replaced after only eight years of service. The costs of the replacement material and of the scheduled or unscheduled outages of the utility are only one aspect of the problem. The other aspect is the potential safety hazard due to equipment failure. This can be many times more serious than the direct money loss.

These economic and security considerations are strong enough to justify the interest and the investment of resources to achieve a better understanding of the mechanism of corrosion-erosion in low carbon steel.

Some preliminary work sponsored by Northeast Utilities and others has been done on this subject since 1981 in the Mechanical Engineering Department at M.I.T. At present there is a research project in progress called "Erosive-Corrosive Wear in the Steam Extraction Lines of Power Plants." One of the aims of this research project is to establish a theory that can be used to predict the remaining lifetime of a steam extraction line. To reach this objective we need to know exactly how the corrosion-erosion mechanism works and what are the most essential variables affecting this phenomenon. As will be seen, one of these variables is the

solid-to-water mass transfer coefficient which plays an important role in both the magnetite dissolution and the erosion mechanism.

Examination of worn pipes shows that maximum wear occurs in those regions where there are abrupt changes in the flow direction, such as elbows, tees and in the wake of welding backup rings. A location which experiences one of the greatest metal removal rates in the extraction lines of power plants is the groove that sometimes exists in the welds between the pipes and the fittings.

Since we know that the mass transfer coefficient is an important variable acting on the dissolution process, and more that one of the most important places to be studied is the wake of a welding backup ring, the determination of the mass transfer coefficient variation in the vicinity of the grooves underneath the welds is essential for understanding the problem.

To obtain the data necessary for measuring the mass transfer coefficient variation in the vicinity of a groove, an experimental apparatus was built. The apparatus will be described in Sect. 3.2. Knowing the distribution of the coefficient along the region including the groove, we can correlate the enhanced mass transfer coefficient with that of the straight part of the section tested, and this ratio is a good approximation of how fast the worst region experiences a wear rate greater than the straight one.

1.2 Review of Previous Work

There is a reasonable amount of literature about the corrosion-erosion problem, and there are some references on the use of plaster-of-paris ($CaSO_4 \cdot 1/2\ H_2O$). The present work uses the technique of measuring mass transfer coefficients in a plane test section made of plaster-of-paris and plexiglas in order to provide a basis for predicting the dissolution effects in the groove of a welding backup ring. This review

is divided in two parts: how corrosion-erosion works and the utilization of plaster-of-paris models for studying it.

1.2.1 Corrosion-Erosion Works

Since 1981, a series of progress reports, graduate student theses, and projects have been done on the topic of errosive-corrosive wear in steam pipelines. The first progress report on this subject, which originated this research field in the Mechanical Engineering Department at M.I.T., was written in August 1981 by Griffith et al. [16].

With the purposes of (1) understanding the wear distribution in a complicated steamline, (2) determining the location of maximum wear, and (3) applying these results to analyze the extraction steamlines of Pilgrim 1 Utility, Vu [31] built a simplified scale model using two-inch glass pipes and bends. Vu's experimental set-up (Fig. 1) consisted basically of a blower, an entrance pipe, a water flowmeter and a test section which was made by three elbows and four plexiglass tubes. For visual studies of the flow he used glass elbows and for drop deposition measurements, copper elbows were utilized. Simulating the steam two-phase flow as an air-and-water mixture he discovered a very interesting fact about the wear mechanism in a bend: there are two distinct wear mechanisms in the vicinity of a bend steamline. On the outside of a bend erosion is caused by drop impingement on the metal oxide whereas, on the inside corrosion is caused by dissolution of the metal oxide in the flowing water film. He also concluded that in the droplet impact mechanism the drops, formed by the liquid phase entrained in the gas flow, always impinged on the outside of the bend where, as a consequence, the oxide layer was eroded. On the other hand, a secondary flow brought a high velocity liquid film, where a violent local turbulence involving separation and recirculation could occur if the bend was

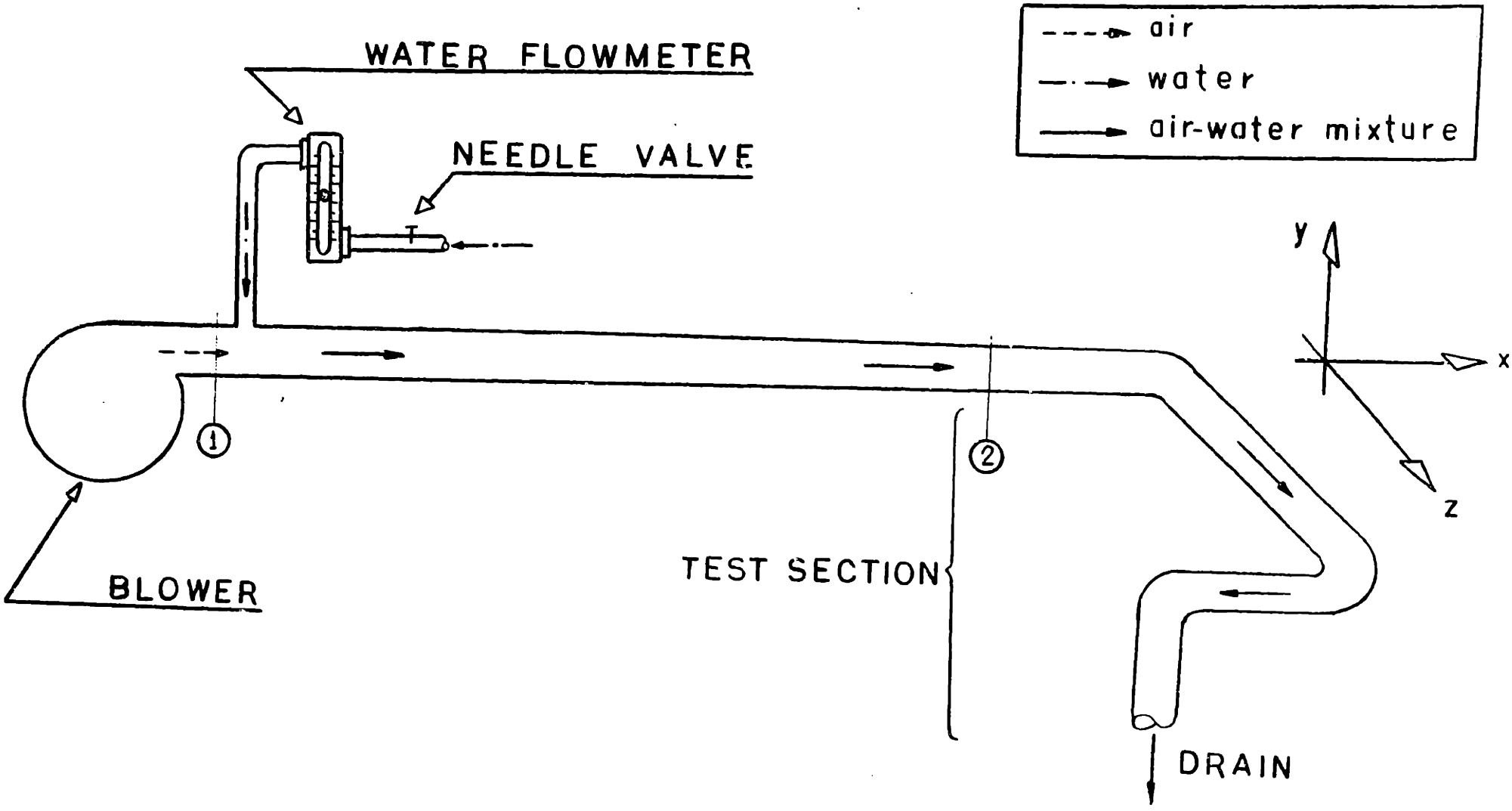

Figure 1-Schematic drawing of Vu's experimental set-up.

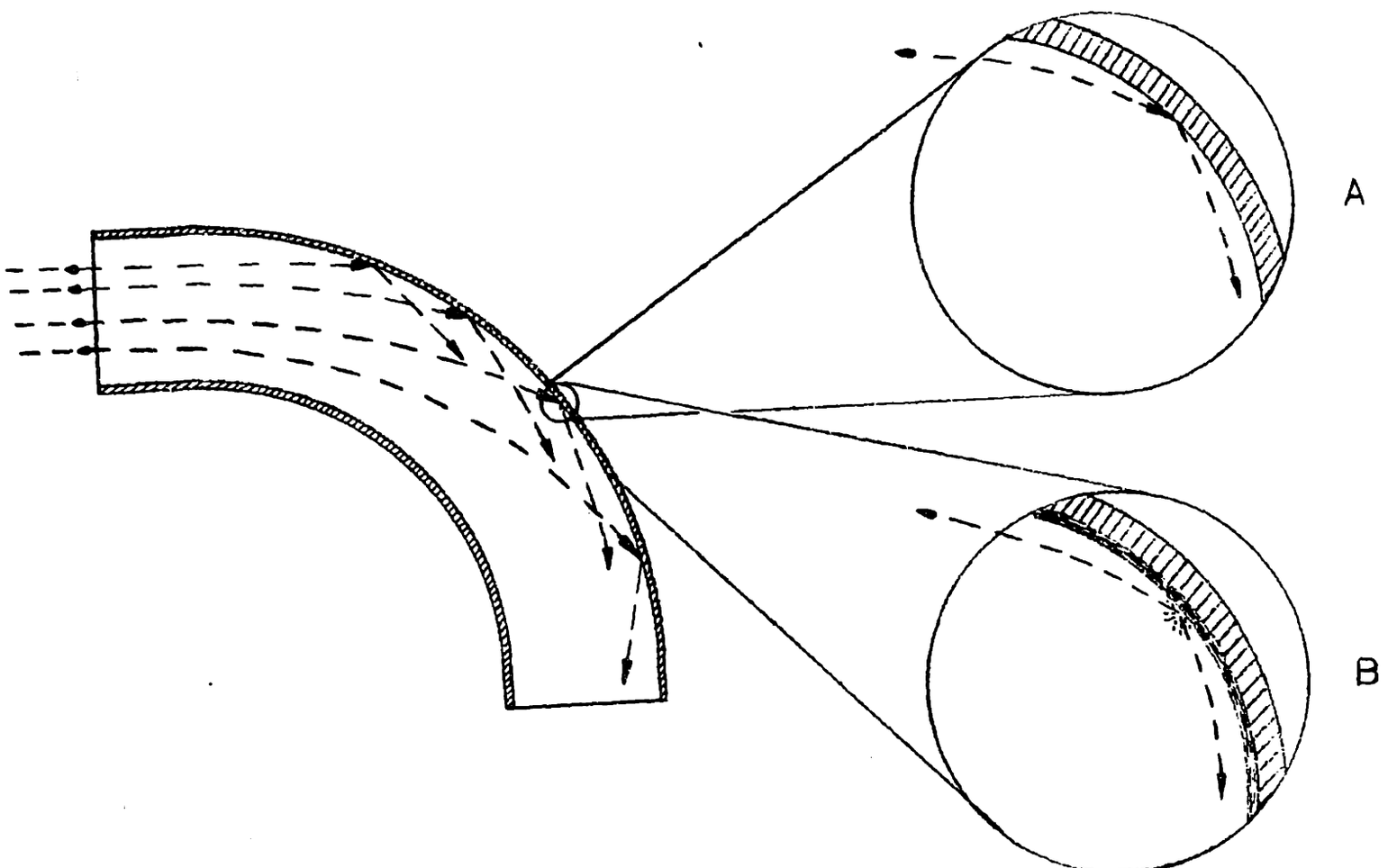

A- Impingement of droplets creates oxide layer (corrosion) which is eventually eroded away.

B- Impingement of droplets removes metal material.

Figure 2.a-Wear induced by droplet impingement.

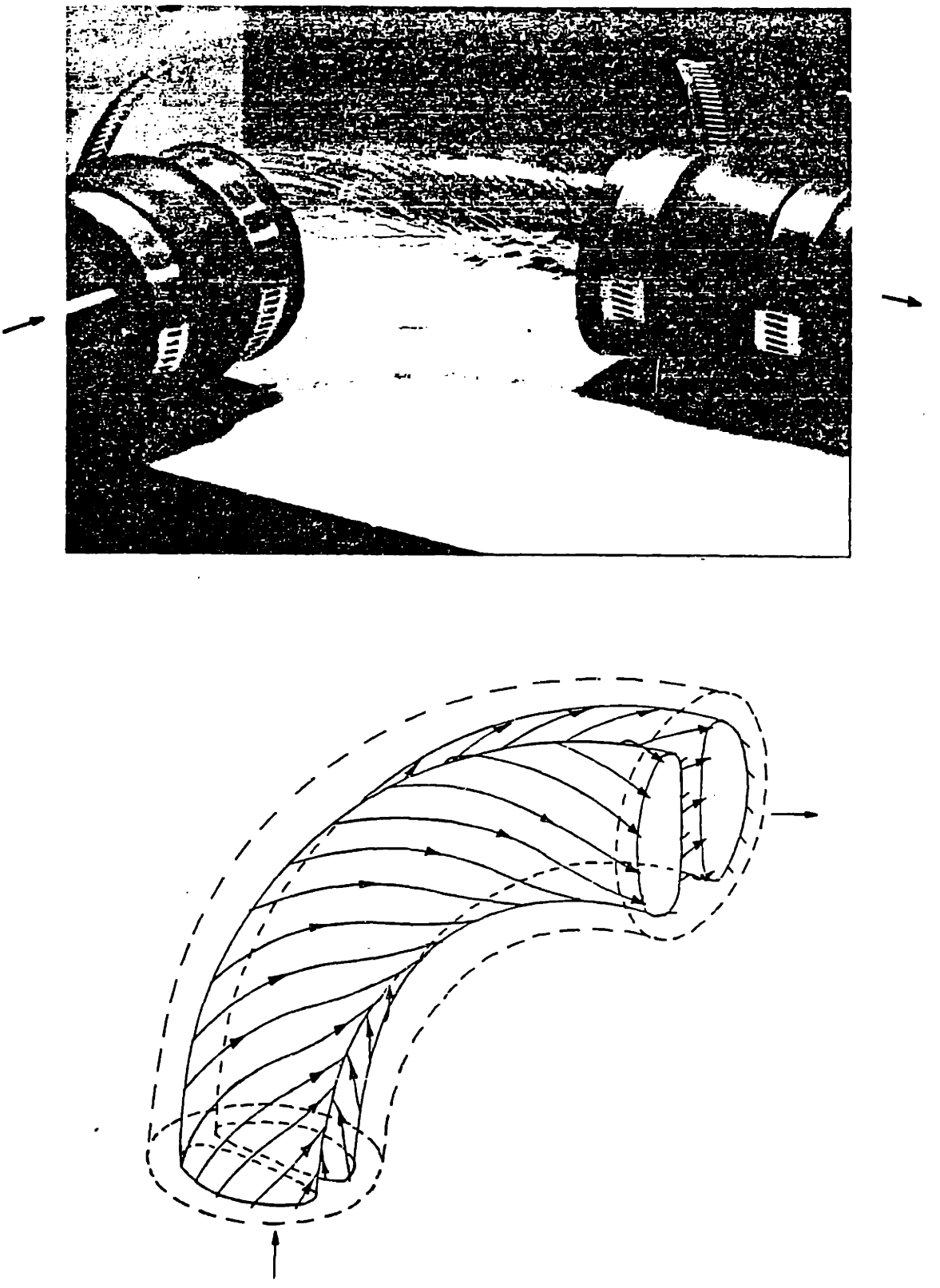

Figure 2.b-Double helical secondary flow in a bend.

out-of-round or tightly curved to the inside part of the bend. In this section an oxide layer was developed and the magnetite was continuously dissolved into the water film by the highly local turbulence, increasing the corrosion rate. Figures 2a and 2b show the droplet impingement wear and the secondary flow in the gas core of a bend as described by Vu.

Using a simplified model (Fig. 3) of Pilgrim 1's extraction line, Pak [23] conduced air-water experiments with the following objectives: investigating the criteria which must be satisfied to predict the mass transfer in steam lines from experiments; and predicting the maximum wear location in a bend for different bend orientations and various flow velocities and qualities. To reach his objectives Pak developed a coating which was made by Elmer's glue tinted with a water-color dye, for covering the inside part of the glass bends. This coating, compared to many other coating methods tested by Pak, best satisfied his experimental needs because it would wear away in the air-water flow, could be easily colored, and its thickness could be controlled reasonably well. From his work he confirmed V_u's conclusion about the two different wear mechanisms acting in a bend; that variations in quality and bend positions had no effect on wear locations; and finally that the inside wear location was not dependent on velocity, quality or bend orientation. He also found that generally the outside wear spot location was gas-velocity dependent, moving upstream as gas velocity increased.

Continuing work on corrosion-erosion staff, Sanchez-Caldera [27] extended more deeply the literature search and the work done by Vu, and made an analysis of the low carbon steel corrosion in a single-phase flow at varying velocities and temperatures. Summarizing the state-of-the-art on

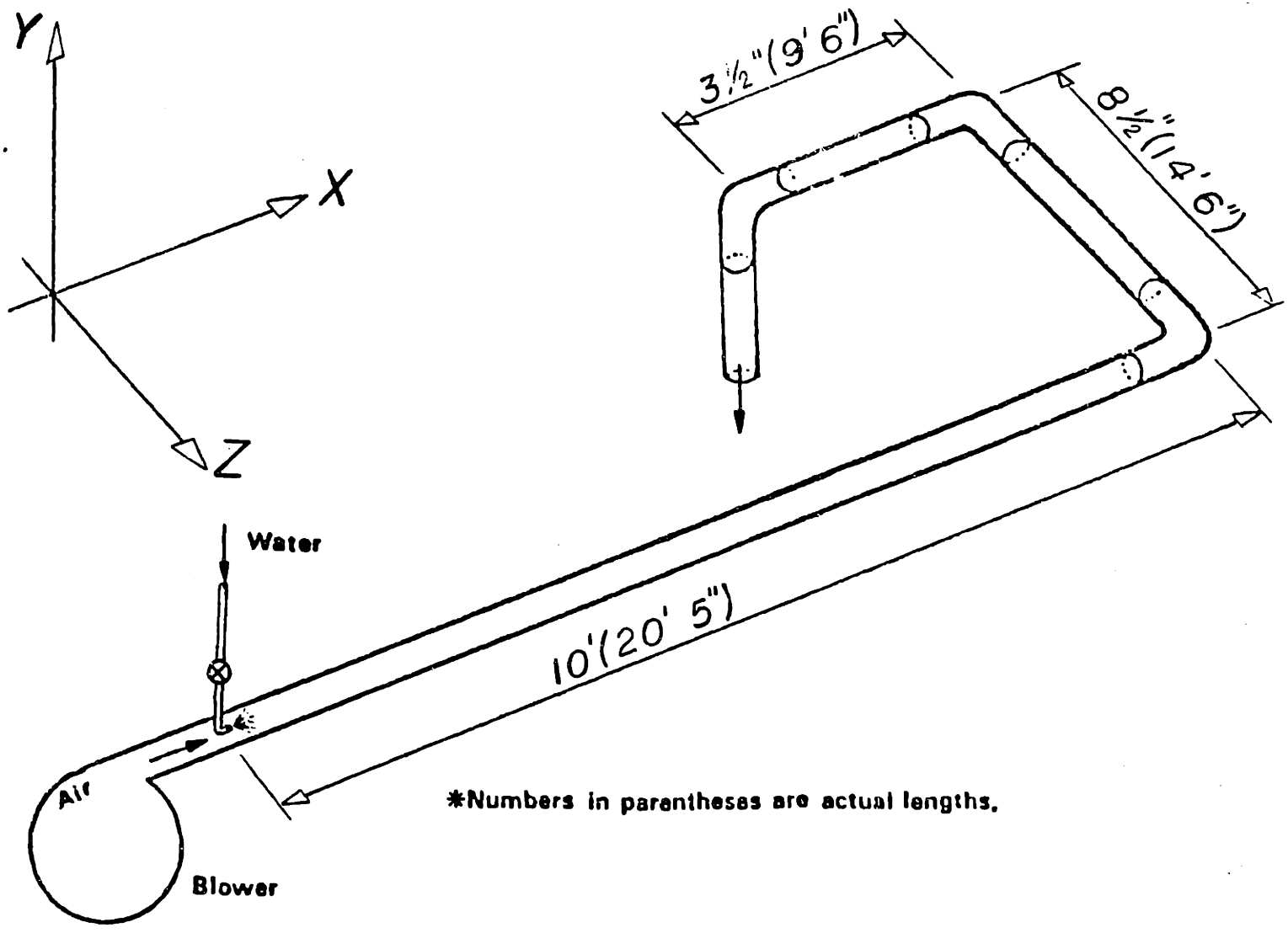

Figure 3-Pak's simplified model of Pilgrim 1's extraction line.

corrosion-erosion he developed a model for corrosion-erosion phenomena, given by Eq. (1.1).

$$\dot{m}_1'' = \frac{C_e \Theta}{\frac{1}{K} + f\left(\frac{1}{h_d} + \frac{\delta}{D}\right)} \qquad (1.1)$$

where

$\dot{m}_1''$ = wear rate ($mol/m^2 s$)

C_e = equilibrium concentration of iron species (mol/m^3)

Θ = porosity (m^2 open area/m^2 metal; $m^2 H_2O/m^2$)

h_d = mass transfer coefficient (m/s)

f = fraction of oxidized metal converted into magnetite at the metal-oxide interface (assumed to have a constant value of 0.5)

D = diffusion coefficient of iron species in water (m^2/s)

δ = oxide thickness (m).

The process occuring during a corrosion-erosion phenomenon and embodied in the above equation are pictured in Figure 4.

Sanchez-Caldera built a corrosion-erosion rig illustrated in Figure 5. The results of his experiments showed that there was a range of temperature (around 150°C) at which the wear rate has a maximum, and that the wear rate was directly related to the flow velocity and inversely related to the pH. He also found that, in general, the wear rate was increased by a high oxygen content (but a very high oxygen content could result in the passivation of iron).

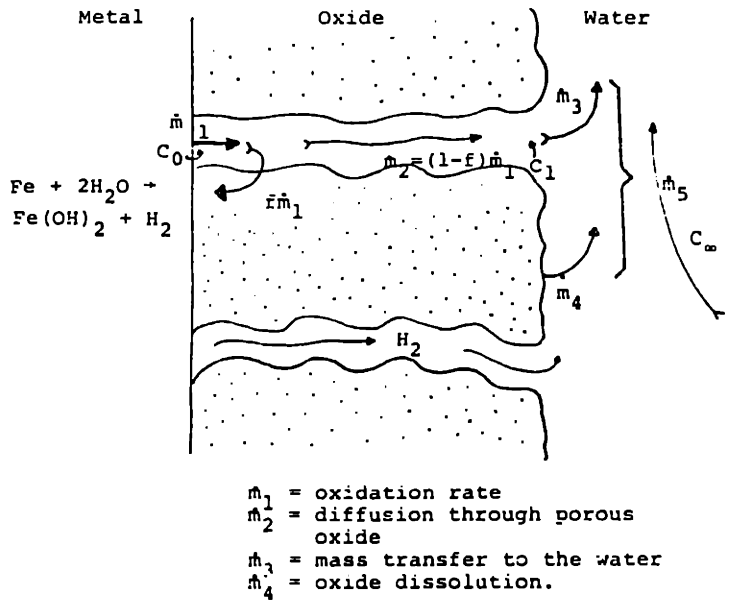

Figure 4-Process included in the corrosion-erosion model.

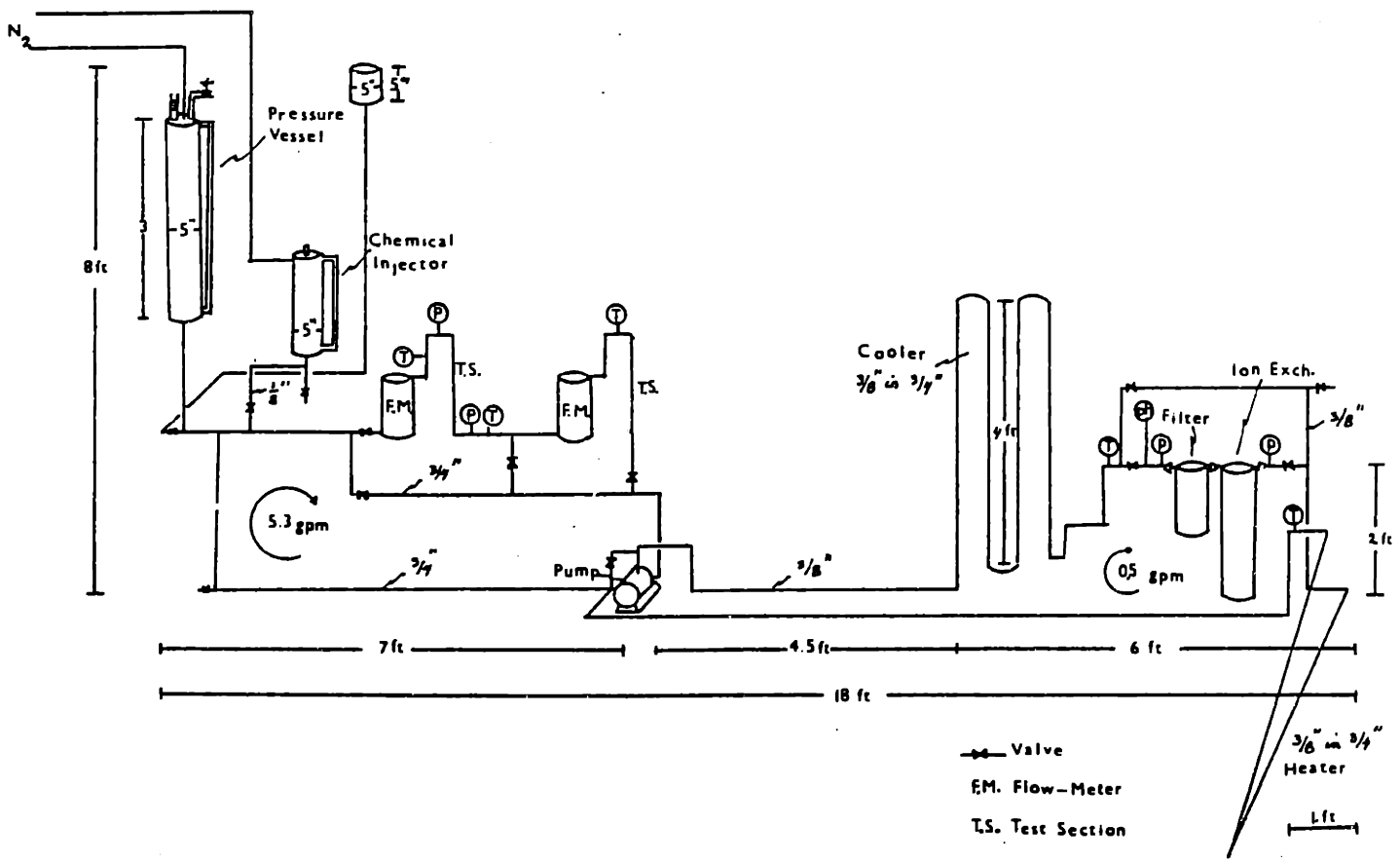

Figure 5-Corrosion-erosion rig built by Sanchez-Caldera.

Focusing on the two-inch tubes with air-water flow experiment, Berkow [6] analyzed the effects of novel bend geometries and bend inserts which would restrain the development of the secondary flow and prevent the droplet impingement. Using a test apparatus (Figure 6) similar to those used by Vu and Pak, he tested several insert and bend designs in order to investigate the wear mechanism. He concluded that the two-phase flow is really very sensitive to the piping system geometry and construction which affect both the wear rate and the maximum wear location; bends with a radius over diameter ratio of 1.5 (standard 1.5 r/d) induced a greater secondary flow than those of longer curvature (r/d = 2.0 or greater), but it was not observed if the dissolution-induced wear on the inner radius was more severe in one type (r/d = 1.5) than the other (r/d = 2.0). Testing out-of-round bends of 1.5 r/d he observed that the sharp form induced a high turbulence increasing the mass transfer associated with the local flow separation and recirculation, and consequently increasing the dissolution rate, too. From his experiences with several types of inserts he concluded that one of them could effectively protect the outer surface of the bend from droplet impingement.

The most recent work on this subject was done by Gawlik [15]. He modified the approach given in the earliest experiments using a model that was an exact replica of the steam extraction line E-103A of Pilgrim 1. He experimented with three different flow regimes to determine how the wear locations vary with gas velocity changes getting data for every bend and the straight section in the model. His experimental rig can be seen in Figure 7. He used the same coating procedure developed by Pak and compared his experimental results with ultrasound data on the remaining wall thickness in the last two bends and interconnecting straight section of line E-103A.

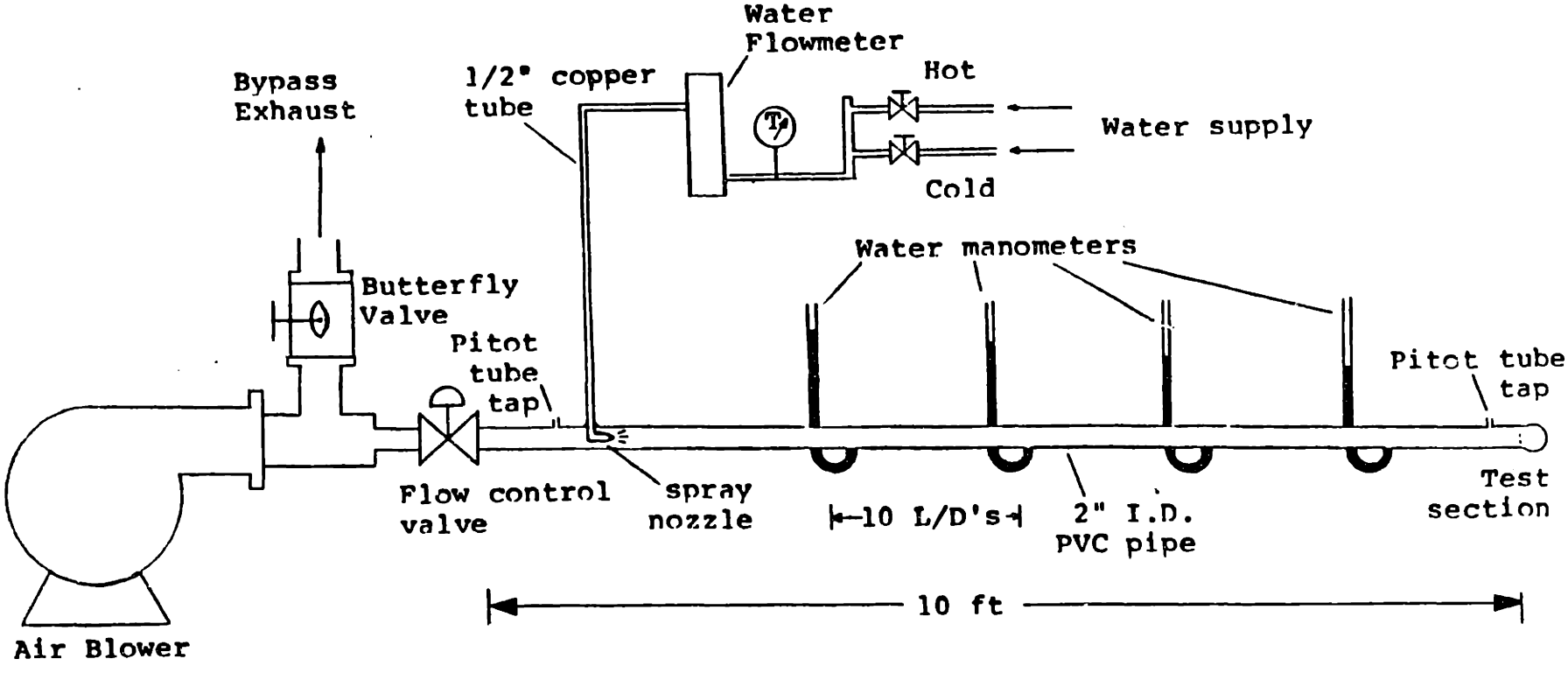

Figure 6-Schematic drawing of Berkow's apparatus.

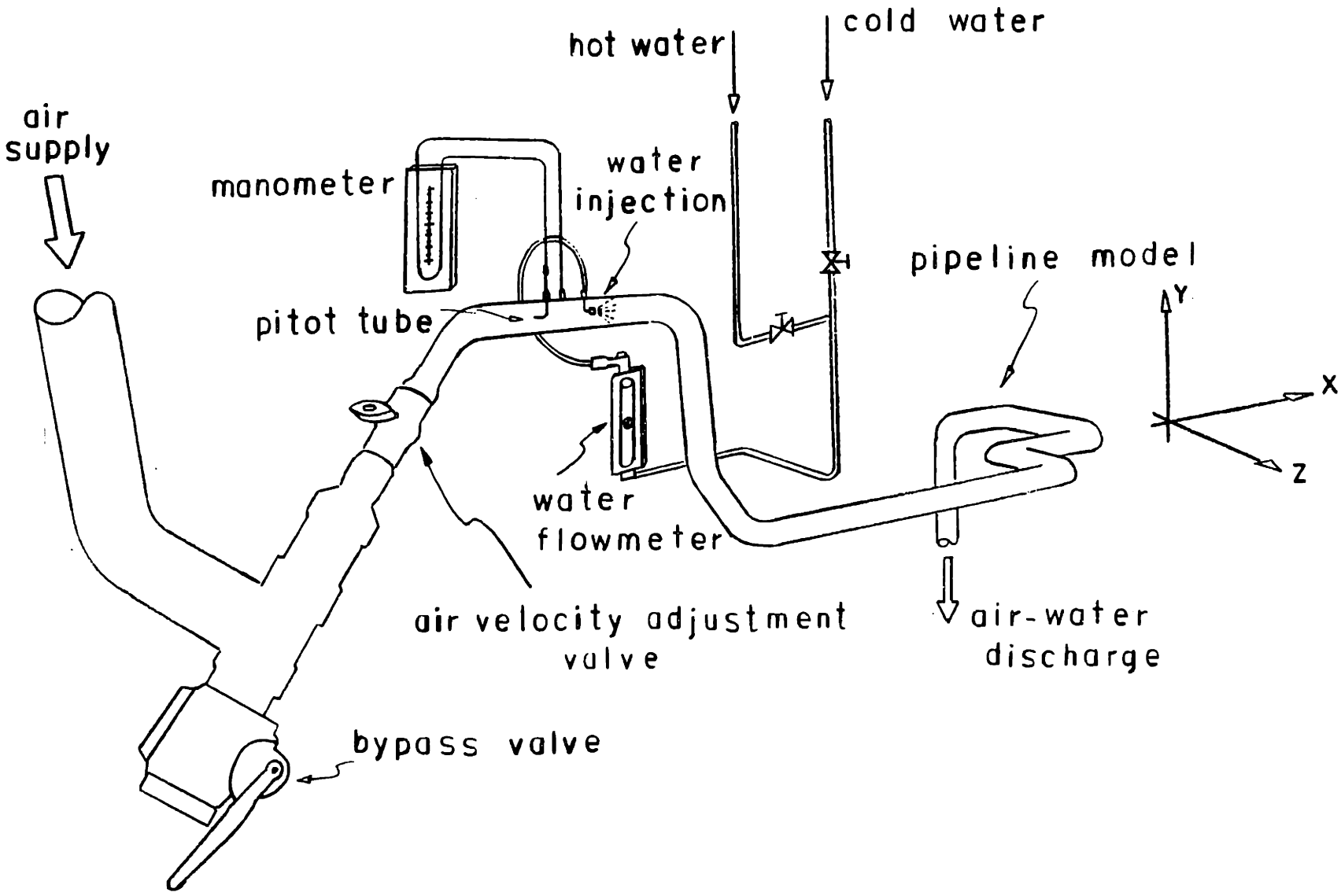

Figure 7-Gawlik's model of Pilgrim 1's extraction line.

From the results of his tests and the ultrasound data, Gawlik concluded that the location of the wear spots for the last bend of the pipe line did not change very much over the range of velocities used and that the wear location on the inside of the last two bends agreed well with the wear pattern in the actual line whereas the wear location on the outside did not reproduce the same actual line pattern. He also made some predictions about the wear locations in a bend based on the behaviour observed in his model.

1.2.2 Plaster-of-Paris Techniques

Plaster-of-paris is the commercial name of calcium sulfate half-hydrate ($CaSO_4 \cdot 1/2\ H_2O$). Its largest application is for repairing of plaster walls and ceilings, and it is an old friend of all contractors because it can easily hide wall defects and irregularities. This compound can also be used for crafting and molding, and until a few years ago was used to make temporary fillings by dentists. Based on the fact that it is only slightly soluble in water at room temperature, it can be used as a flow visualization aid in a similar manner to the production of streaks by differential evaporation of surface coatings on the boundaries of air streams, as observed by Bradshaw [10].

Allen [1] used this property to visualize the pattern of motion on the surface of a model made of plaster-of-paris and immersed in a water stream. He studied the flow around a circular cylinder mounted normal to a flat plate (Figure 8), concluding that this technique for obtaining flow patterns could be very helpful to geologists interested in the mechanisms of sedimentary structure generation found in rocks and modern deposits. Further, Allen published two other reports [2,3] using this technique applied to planar plaster surfaces.

Studying dissolution profiles in a soluble surface adjacent to a turbulent channel flow, Blumberg [9] calculated the average mass transfer coefficient of a plaster plate immersed in a water channel. In his work, Blumberg remarked the distinction between convective transport processes in which the convective surface was fixed and acted as an invariant solid boundary for the flow and those processes where the surface was modified by the convective process. In the first type the flow distribution played the major role in the heat or mass transfer rate distribution. In the second one the mass transfer rate distribution redefined the surface imposing a new boundary condition to the flow which originated a new distribution of transfer rates that, again, changed the surface shape (Figure 9). One of his conclusions was that irregularities on a soluble surface introduced a nonuniformity in the rates of mass transfer with the highest rates located at the reattachment point and the lowest rates at the separation and recirculation regions.

A method that permits measuring the mass transfer coefficient in a simulated steam line component (tube or bend) made of plaster-of-paris and subjected to a single or two-phase flow was presented by Coney, Wilkin and Oates at the Specialists Meeting on Erosion-Corrosion in Les Renerdieres, France [13]. Their work was supported by the Central Electricity Research Laboratories, U.K., and the paper (1) reviewed published information on mass transfer in geometries of interest in boilers, (2) noted that insufficient data were available in the area of two-phase heat or mass transfer for bends and other complex geometries of interest in power plants, (3) described the method of measuring mass transfer by the utilization of plaster-of-paris models, and (4) presented the results of calculations on rates of magnetite

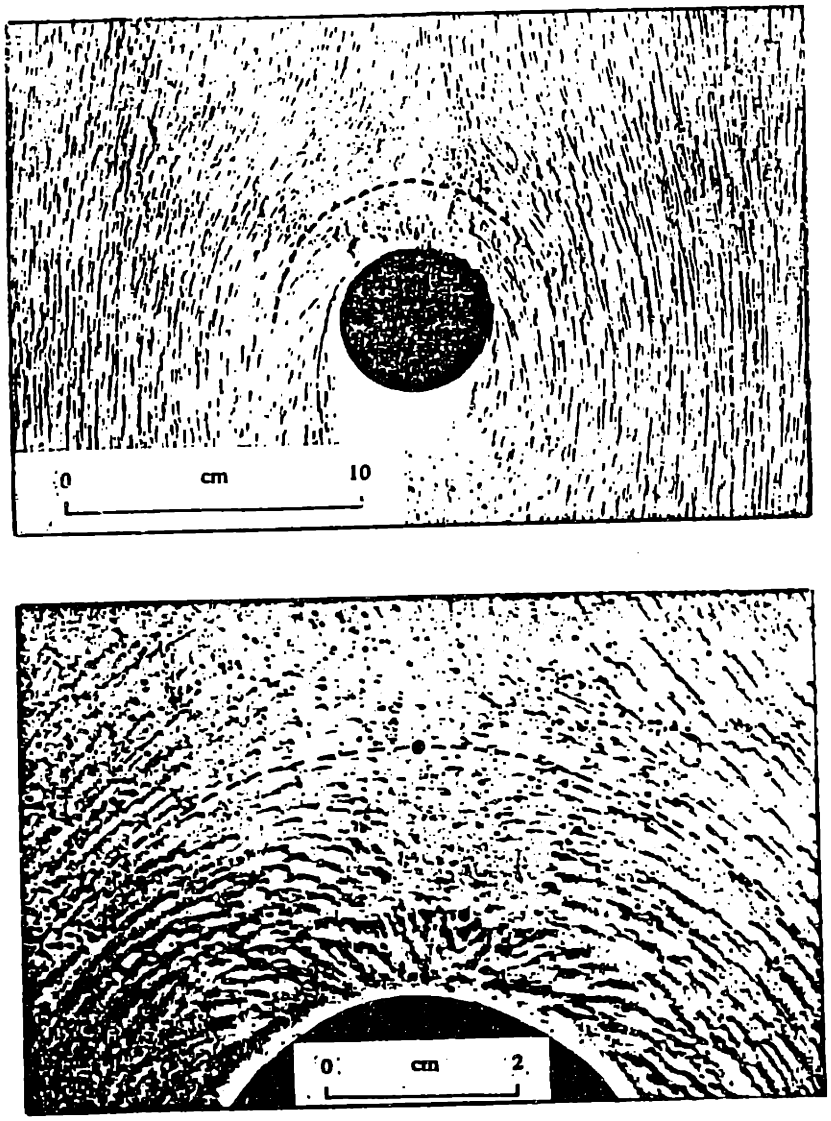

Figure 8-Flow visualization on the surface of a flat plate with a circular cylinder mounted normal to the plate (Allen).

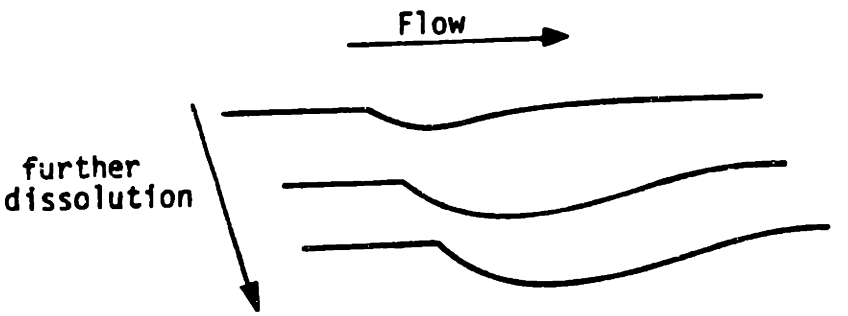

Figure 9-Boundary surface modification due to the mass transfer distribution.

dissolution for combinations of temperature, pH, oxygen concentration, flow rate, steam fraction, and tube geometry.

As an extension of this paper, another was published by Sprague et al. [29] and presented at the European Two-Phase Flow Group Meeting in Zurich. The purpose of these experiments was to investigate the local mass transfer rates under two-phase conditions as a function of quality and mass flow rate. This paper discussed the mechanisms of erosion-corrosion with the objective of aiding the prediction of mass transfer coefficients and erosion-corrosion metal loss rates in power plant boilers operating in a range of 30 to 40 bars pressure.

1.3 The Present Work

The objective of this work was to obtain data which would enable the calculation and analysis of mass transfer coefficient behavior in a planar model simulating a fitting, pipes and backup ring made of plaster-of-paris and submitted to a two-phase air-water flow simulating the steam-water two-phase flow that exists in an extraction pipeline of a power plant like Pilgrim 1 or Millstone.

To achieve this purpose a test rig was designed and built in the Heat Transfer Laboratory of M.I.T. The test rig was designed so that experiments could be conducted using air-water mixtures, in which the air velocity and the water flow rate could vary, and test sections molded with plaster-of-paris on a plexiglass base. The test section could be placed on the rig where the plaster-of-paris was worn out by the air-water flow. After a time interval, usually one or two hours, this section was removed, measurements were made, and pictures taken. Then the test section was reinstalled for another run at the same flow rate and the process repeated.

Running a set of sixteen test sections under different flow conditions, we obtained the data with which the dissolution rates and the mass transfer coefficients were calculated.

An analysis of each experiment was made using the Kunz and Yerazunis theory, associated with the Wallis' annular flow model and the Chenoweth-Martin correlation, in order to predict theoretical values of the mass transfer coefficients. They were then compared to the average coefficient values measured in the experiment.

Based on the final geometry presented by the groove after the experiments, we could consider that there was four distinct regions around this type of singularity and it was possible to relate the mass transfer coefficient of each region to the average mass transfer coefficient of the straight part of the test section.

CHAPTER 2

THEORETICAL BACKGROUND

2.1 Introduction

The analysis of mild steel components (Figures 10.a,b,c and d) used for a certain number of years in a power plant has revealed specific patterns of material loss in the internal surfaces. This loss of material, small and uniform in some cases or large and random in others, is caused by a phenomenon or process known as corrosion-erosion, which creates many other functional and safety problems in equipment used in many industrial fields. Corrosion-erosion is also an economic problem, hence there is a great interest in describing, researching, and trying to identify and understand the variables involved with the purpose of minimizing the effects of material loss and the related security hazards and economic losses. For these reasons, the corrosion-erosion process has been studied in universities and research institutes around the world, and many researchers have dedicated the major part of their time looking for alternative solutions that can, at least, decrease the extent of this problem.

The description of the process and its consequences can be found in many publications, such as those mentioned in the first chapter and as well as the following: Bignold et al. [7], Keller [20,21], and Apblett [4].

We now know that the corrosion-erosion process depends on many variables, such as temperature, fluid velocity, metal composition, flow geometry, solubility, pH, oxygen concentration, and others of less

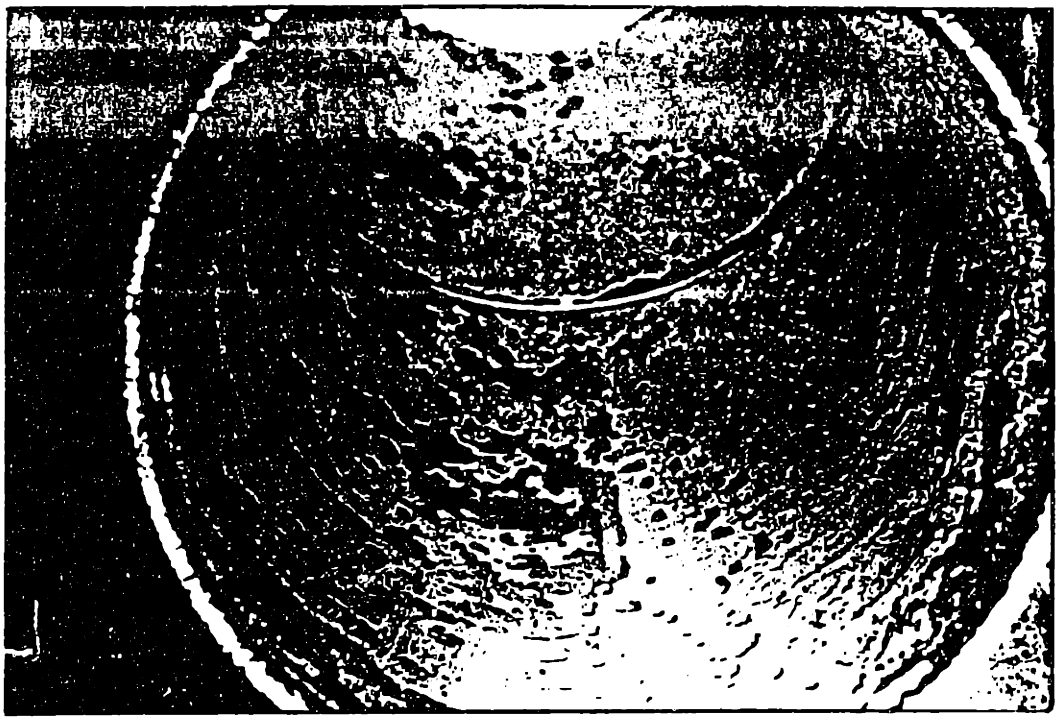

FIGURE 10.a Overview of Outside of Millstone Unit 1 Bend (Keck).

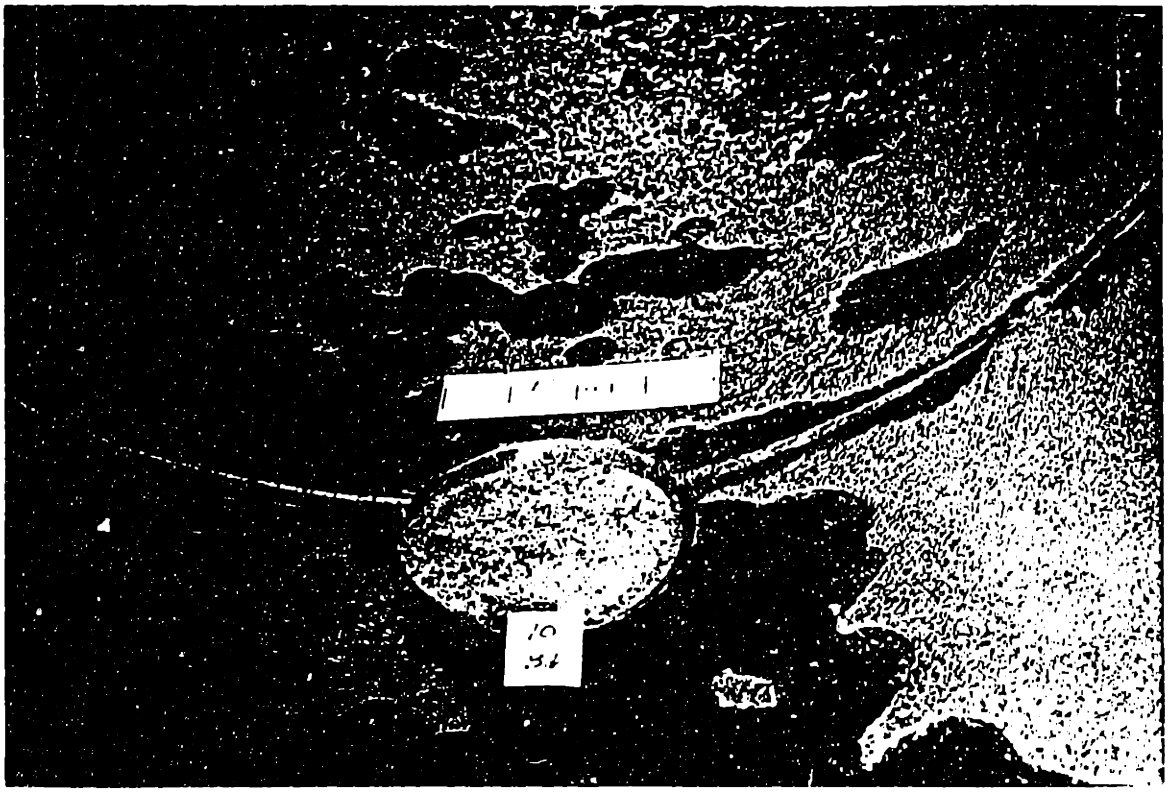

FIGURE 10.b Cut from Circumferential Weld, on Bottom (Keck).

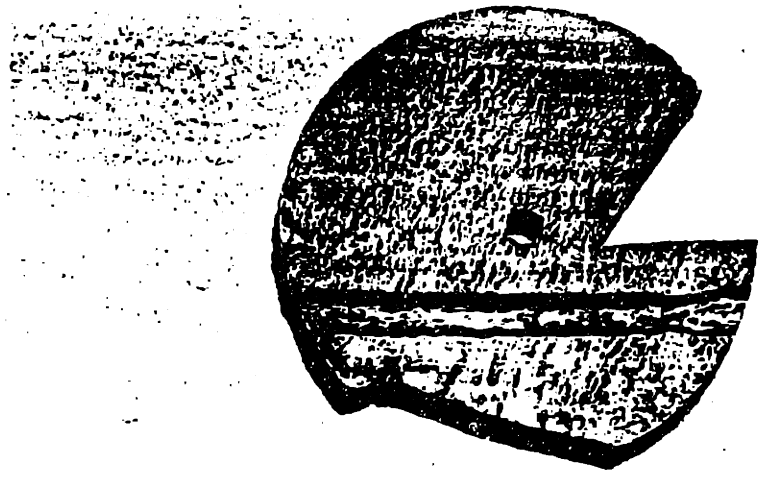

FIGURE 10.c Weld Joint Sample from the Extraction Line of Millstone Unit 1.

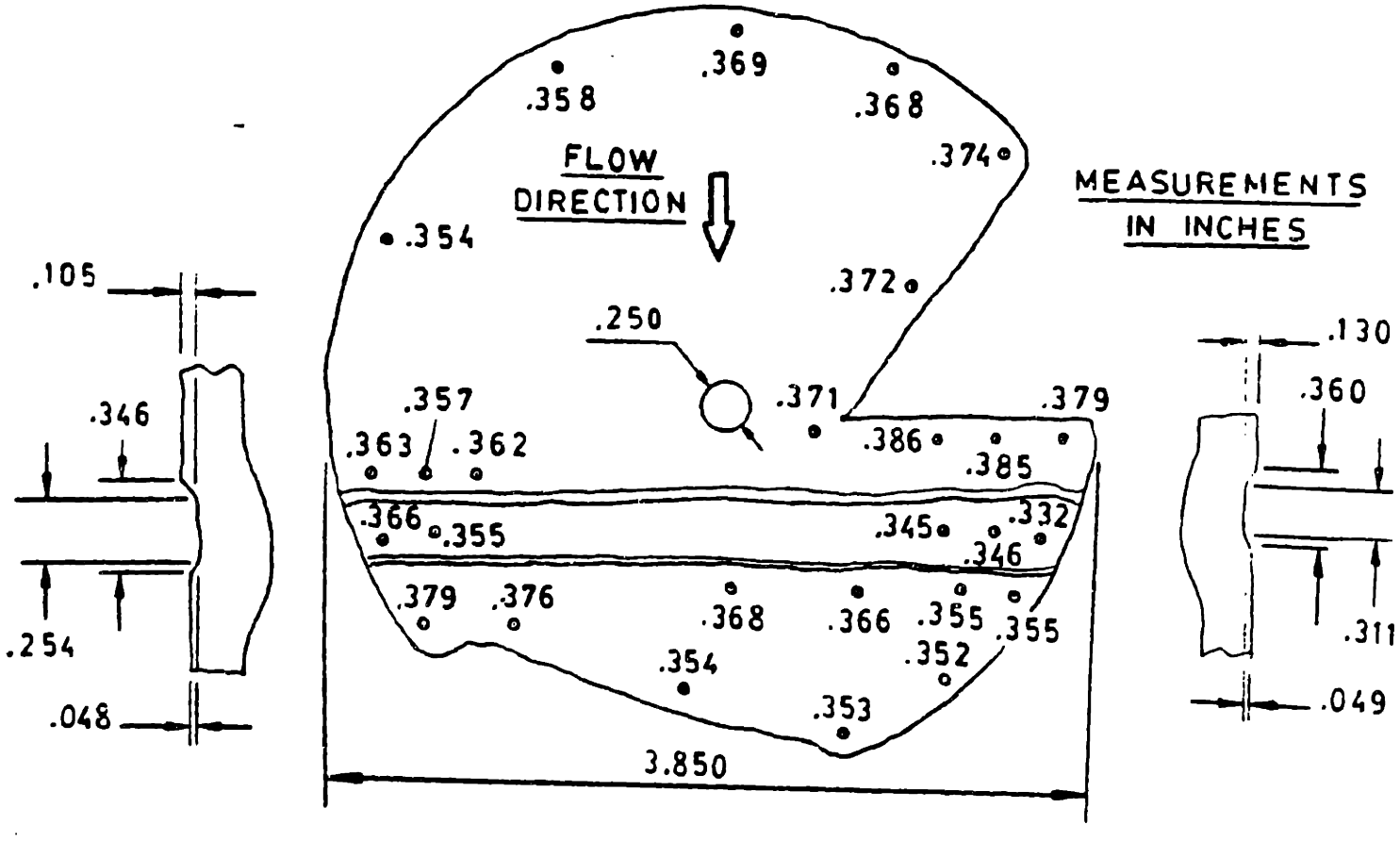

FIGURE 10.d Thickness Measurements of the Weld Joint Sample.

importance. Some authors have concluded that in some situations erosion has the same weight as corrosion, but others have suggested that erosion plays a secondary role in the basic mechanism, which acts essentially as a dissolution process where the mass transfer and the geometry are the basic factors Bignold et al. [8] and Sydberg et al. [30].

The results obtained by Coney et al. and Blumberg suggested that the latter hypothesis seems to be the more reasonable for a case in which a singularity is present on the boundary surface, such as the case of the groove existing underneath a welding ring, which is the case in which we are particularly interested.

2.2 Heat and Mass Transfer Analogy

Some relationships and dimensionless groups are necessary to describe the heat transfer process and others to describe the mass transfer process. From the simularities between each relationship and dimensionless group used to describe one process or other we have the analogy between heat and mass transfer, which allows us to use many heat transfer data to predict mass transfer and vice-versa. Nevertheless, we have to keep in mind that there are limits in using this analogy, for example, the case of heat transfer in bends, which has been pointed out by Coney et al. Throughout this work we will make use of the heat and mass transfer analogy, but it is always important to keep in mind that this analogy must be used with caution and sometimes is not applicable at all.

The dimensionless groups that describe the heat transfer process are the Reynolds, Nusselt, and Prandtl numbers whereas the same Reynolds number combined with the Sherwood and Schmidt numbers describe the mass transfer process.

These groups are defined as follows:

Reynolds Number: $$Re = \frac{Vd}{\nu} = \frac{\rho V d}{\mu} \quad (2.1)$$

Nusselt Number: $$Nu = \frac{hd}{K} \quad (2.2)$$

Prandtl Number: $$Pr = \frac{\nu}{\alpha} \quad (2.3)$$

Sherwood Number: $$Sh = \frac{h_d d}{D} \quad (2.4)$$

Schmidt Number: $$Sc = \frac{\nu}{D} = \frac{\mu}{\rho D} \quad (2.5)$$

$\bar{V}$ = velocity (m/s)

d = diameter or hydraulic diameter (m)

ρ = density (kg/m^3)

ν = kinematic viscosity (m^2/s)

μ = dynamic viscosity ($kg/m^2 s$)

h = heat transfer coefficient (W/m^2 C)

k = thermal conductivity (W/m^2 C)

α = thermal diffusivity (m^2/s)

h_d = mass transfer coefficient (m/s)

D = diffusivity (m^2/s)

The relationships describing both processes are similar, too, as can be seen in the Table 2.1.

HEAT TRANSFER		MASS TRANSFER	
$Nu = Nu(Re,Pr)$	(2.6)	$Sh = Sh(Re,Sc)$	(2.9)
$\frac{Q}{\rho C_p} = (\alpha+\epsilon)\frac{dT}{dy}$	(2.7)	$J = (D+\epsilon)\frac{dC}{dy}$	(2.10)
$Q = h(T_w-T_\infty)$	(2.8)	$J = h_d(C_w-C_\infty)$	(2.11)

Q = heat flux (W/m^2s)

J = mass flux (kg/m^2s)

C_p= specific heat (J/kg C)

ϵ = eddy diffusivity (m^2/s)

T = temperature (^oC or K)

C = concentration (kg/m^3)

y = distance from the wall surface (m)

subscript w = wall property

subscript ∞ = bulk property

TABLE 2.1-Heat and mass transfer relationships.

Correlations with the general form of (2.6) and (2.9) are largely applied and useful in the study of heat and mass transfer. They can be obtained from a dimensional analysis of a certain problem or phenomenon and from correlating data obtained from experiments that reproduce the type of problem in which we are interested. Usually these experiments are carried out on scale models and the results, as obtained, can be extrapolated considering similarity factors such as geometry, flow regime, a range of dimensionless group values, and others.

2.3 Previous Work and Correlations

2.3.1 Berger and Hau

A correlation formulated by Berger and Hau was used in Pak's thesis and in the preliminary calculations of the Second Progress Report of the Corrosion-Erosion Project. Coney et al. also used this correlation, which compared favorably with their experimental results.

Berger and Hau measured mass transfer coefficients by the electrochemical method in a fully developed flow in smooth pipes, over the range $8 \times 10^3 < Re < 2 \times 10^5$ and Schmidt numbers in the range between 10^3 and 6×10^3, and concluded that, when the concentration boundary layer was fully developed, their results could be described by:

$$St_d = 0.0165\, Re^{-0.14} Sc^{0.67} \tag{2.12}$$

where St_d means the Stanton number for mass transfer, defined as:

$$St_d = \frac{Sh}{ReSc} = \frac{\frac{h_d d}{D}}{\frac{Vd}{\nu}\,\frac{\nu}{D}} = \frac{h_d}{V} \tag{2.13}$$

Analogously we can have for heat transfer,

$$St = 0.0165\, Re^{-0.14} Pr^{0.67} \tag{2.14}$$

with the corresponding Stanton number for heat transfer given by:

$$St = \frac{Nu}{RePr} = \frac{\frac{hd}{K}}{\frac{Vd}{\nu}\frac{\nu}{\alpha}} = \frac{h\alpha}{VK} \tag{2.15}$$

Using published data together with their results they developed another empirical relation which can be used in the ranges $0.6 < Sc$ or $Pr < 10^4$ and $10^4 < Re < 10^6$ for predicting heat or mass transfer rates

$$Sh = 2 + cRe^{a} Sc^{1/3} \tag{2.16}$$

or

$$Nu = 2 + cRe^{a} Pr^{1/3} \tag{2.17}$$

where a and c are given by:

$$a = 0.86 - \frac{1}{(4.7\ Sc)^{1/3}} \tag{2.18}$$

$$c = 0.0165 + 0.011\, Sc\ \exp(-Sc) \tag{2.19}$$

For Sc or $Pr > 10$, a simpler form of equations (2.16) or (2.17) can be used

$$Sh = 0.0165\, Re^{0.86}\, Sc^{1/3} \qquad (2.20)$$

2.3.2 Kunz and Yerazunis

An analysis considering annular two-phase flow over a wide range of film Reynolds and Prandtl numbers was presented by Kunz and Yerazunis [22]. Using (1) velocity and temperature profiles across the liquid film obtained from the transport equations for turbulent flow, (2) shear-stress distribution resulting from the Navier-Stokes equations applied to flow in the annular film, and (3) heat-flux distribution derived by applying the energy equation to the annular liquid film, they concluded that it was possible to correlate the friction Stanton number (St*) with the liquid Reynolds (Re_L) and liquid Prandtl (Pr_L) numbers. Their results can be shown in a graphical form (Figure 11) relating the variation of the product $Pr_L^{-} St^*$ with Re_L and $\bar{Pr}$.

These parameters are defined as follows:

Friction Stanton Number:

$$St^* = \frac{h}{\rho_L v^* Cp_L} \qquad (2.21)$$

Superficial liquid Reynolds Number:

$$Re_L = \frac{4\Gamma}{\mu_L} \qquad (2.22)$$

Liquid Prandtl Number:

$$Pr_L = \frac{\nu_L}{\alpha} \qquad (2.23)$$

where:

v^* = friction velocity = $\sqrt{\frac{\tau_w g_c}{\rho_L}}$ (m/s)

Γ = liquid flow per unit of surface width or circumference (kg/m s)

τ_w = shear stress at the wall (kg/m^2)

g_c = gravitational constant (kg m/kgf s^2)

subscript L = liquid phase

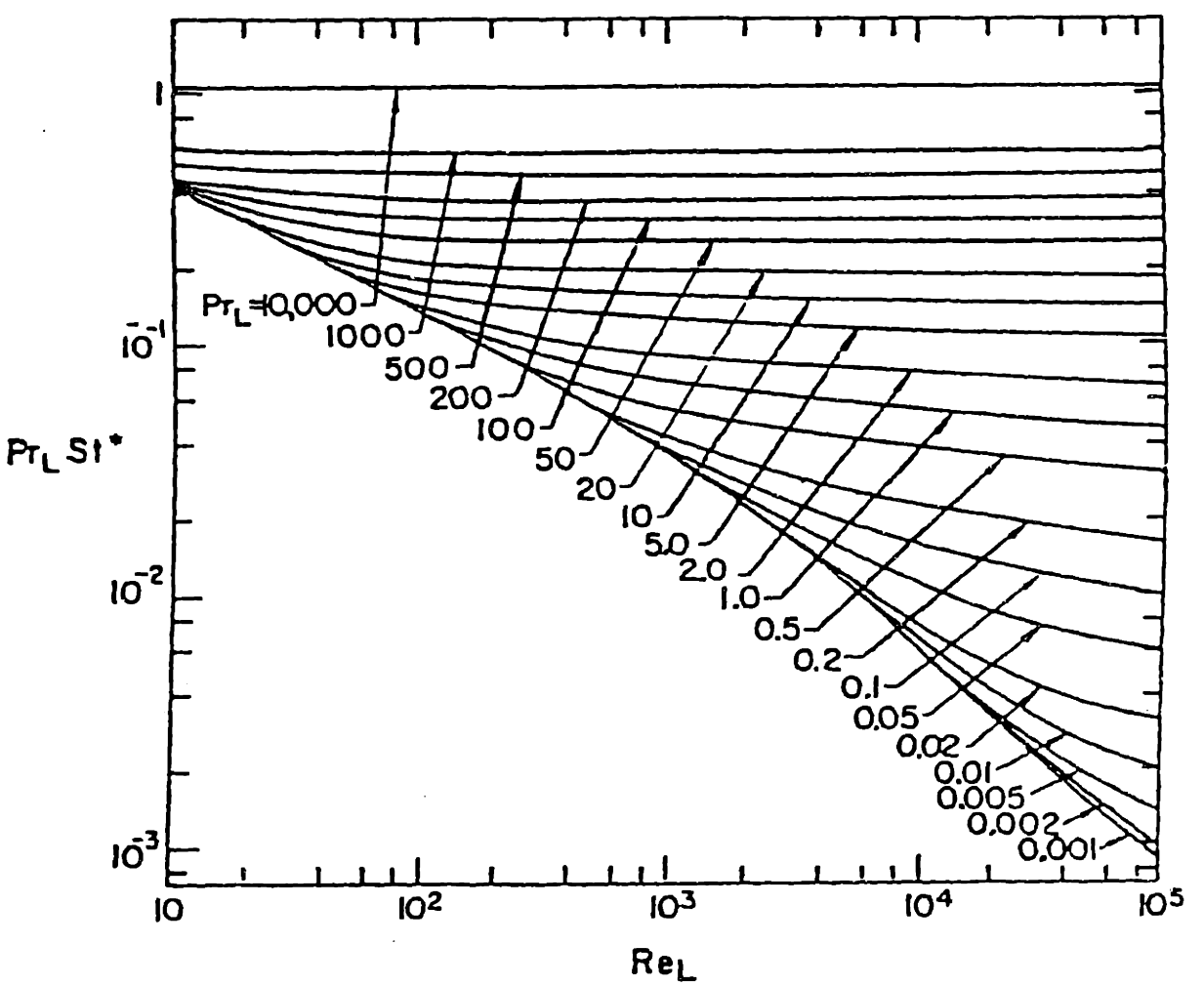

Figure 11-Kunz and Yerazunis results for the variation of Pr.St* with Re_L and Pr_L.

The wall shear stress (τ_w) which is used to calculate the friction velocity and the friction Stanton number was obtained using the Lockhart and Martinelli method.

In order to use Kunz and Yerazunis results to obtain the mass transfer coefficient (h_d) we have to know the friction velocity (v^*) which depends on the shear stress at the wall (τ_w). The shear stress at the wall can be obtained from a force balance over a section of infinitesimal length dz, as is represented in Figure 12, and to make the force balance we need to have an estimate of the pressure drop across the section.

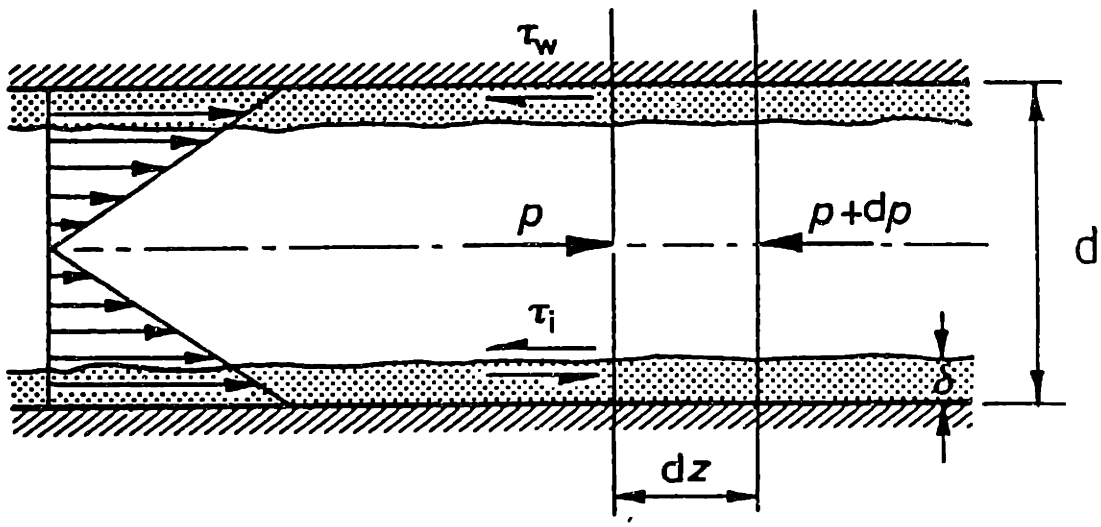

Force balance on the combined phases : $$-\left(\frac{dp}{dz}F\right) = \frac{4\tau_w}{d}$$

Force balance on the vapour phase alone: $$-\left(\frac{dp}{dz}F\right) = \frac{4\tau_i}{(d-2\delta}$$

Figure 12-Force balance over a section of infinitesimal length dz and shear stress distribution in horizontal annular flow.

In their work, Kunz and Yerazunis compared the results of their analysis with experimental and theoretical results of other investigators, concluding that there is a good agreement over the range of liquid Prandtl numbers from 10^{-3} to 10^{4}.

Making a simple block diagram, we need:

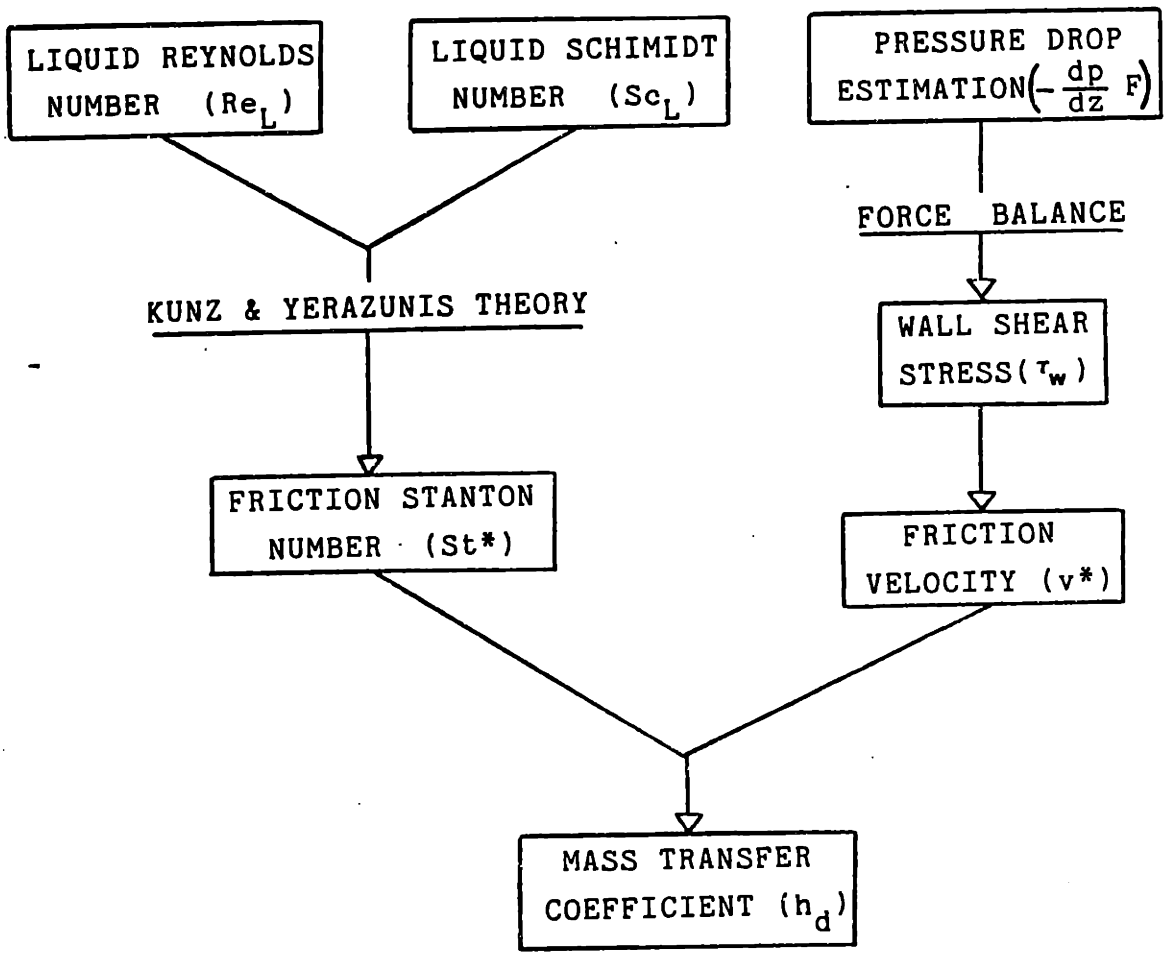

Figure 13-Mass transfer coefficient determination using Kunz and Yerazunis theory.

The main problem now is in estimating the pressure drop. In the original paper, as stated previously, Kunz and Yerazunis used the Lockhart and Martinelli method for predicting the two-phase flow pressure drop. This method is the most generally accepted for this type of estimation, but the Lockhart-Martinelli correlation was developed for conditions close to atmospheric pressure and for small-diameter pipes. When data obtained by other researchers (Lester et al., Becker and Chenoweth and Martin) are compared with Lockhart-Martinelli's predictions, one can see discrepancies among the pressure drop results.

According to Collier [12] the agreement between the data obtained by Lester with the Chenoweth and Martin correlation is better than with the Lockhart-Martinelli correlation, and, therefore, the correlation given in Chenoweth's and Martin's paper [11] is recommended for pipe bore sizes greater than 5 cm.

To see how these methods for two-phase flow pressure drop predictions work, we will briefly review the two-phase flow methods of analysis in the next section.

2.4 Two-Phase Flow

One of the most concise and clearest definitions of two-phase flow is that given by Wallis at the beginning of his book. Answering the question "What is two-phase flow?", he wrote: — "A phase is simply one of the states of matter and can be either a gas, a liquid, or a solid. Multiphase flow is the simultaneous flow of several phases. Two-phase flow is the simplest case of multiphase flow."

Despite being the simplest case of multiphase flow, its theoretical analysis is not so simple as can be inferred from Wallis' answer. There are

basically two general approaches to formulating models for a two-phase flow analysis: the more established approach is to derive the control volume balance equations, such as the treatment given by Collier [12] or Wallis [32]; the more recent one consists in averaging the local and instantaneous equations in time or space as can be seen in Ishii [17] or in Delhaye et al. [14].

In a single-phase flow, an observer of a point located in the flow channel will see one continuous material, whereas in the case of a two-phase flow there are many internal configurations that can be assumed and the observer will see one phase continuously, as in annular flow, or two-phases intermittently as in bubbly flow [18].

Two-phase flow methods of analysis are extensions of those used for single-phase flow and its procedure consists in (1) writing down the basic mass, momentum, and energy conservation equations and (2) trying to solve them by using simplified assumptions. These assumptions usually give the name of the method, so the three types of methods used are: the homogeneous flow model, the separated flow model, and the flow pattern method.

The easiest method is the homogeneous flow model which assumes that (1) there is no relative velocity between the two phases, (2) the liquid and vapor phases are in thermodynamic equilibrium, and (3) a suitably defined single-phase friction factor is used for two-phase flow. The mixture, with mean fluid properties, is then considered as a single-phase flow whose balance equations are solved.

The separated flow model assumes that the two phases are artificially segregated and two sets of balance equations are obtained, one set for each phase. These equations are combined with other information, such as, area

of the channel occupied by each phase or velocities of each phase, and frictional interactions between the phases and with the walls. In its simplest form, each stream, liquid or vapor, is assumed to travel at a mean velocity and, when these mean velocities are equal, the balance equations are reduced to those of the homogeneous flow model.

The third and more elaborate method is the flow pattern model, described in Wallis' book. This method considers that the phases are arranged in one of four prescribed geometries based on several configuration types or flow patterns that a gas and a liquid flow can assume when they are together within a channel (see Figs. 14.a and 14.b). The flow patterns considered by Wallis were bubbly, slug, annular and drop flow. For each of these idealized representations the basic equations are solved according to assumptions that consider the intrinsic characteristics of each configuration.

2.4.1 Pressure Drop Evaluations

Evaluations of pressure drop are based on the methods of analysis, hence one can predict the pressure loss using the homogeneous, the separated, or the flow pattern method. In order to obtain the two-phase pressure drop gradient using either the homogeneous or the separated flow method we use the frictional pressure gradient calculated from the Fanning equation for the total liquid plus vapour flow, assumed to flow as a liquid, multiplied by a factor known as the two-phase frictional multiplier, as follows:

$$\left(-\frac{dp}{dz}_F\right) = \left(-\frac{dp}{dz}_F\right)_{f_o} \Phi_{f_o}^2 \qquad (2.24)$$

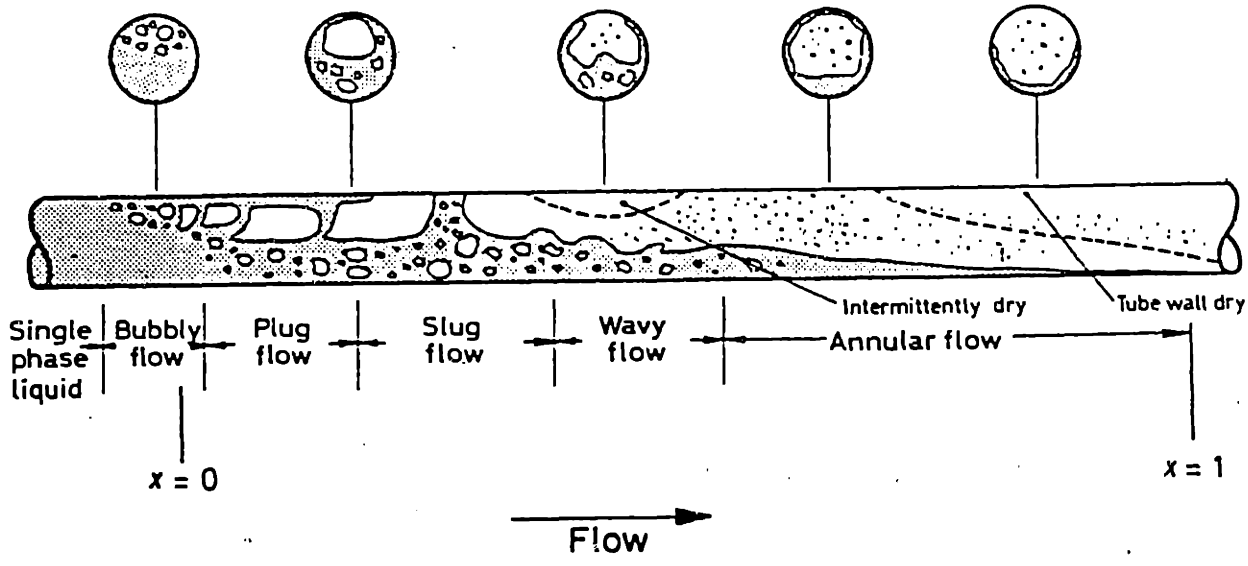

Figure 14.a-Flow patterns in a horizontal tube evaporator.

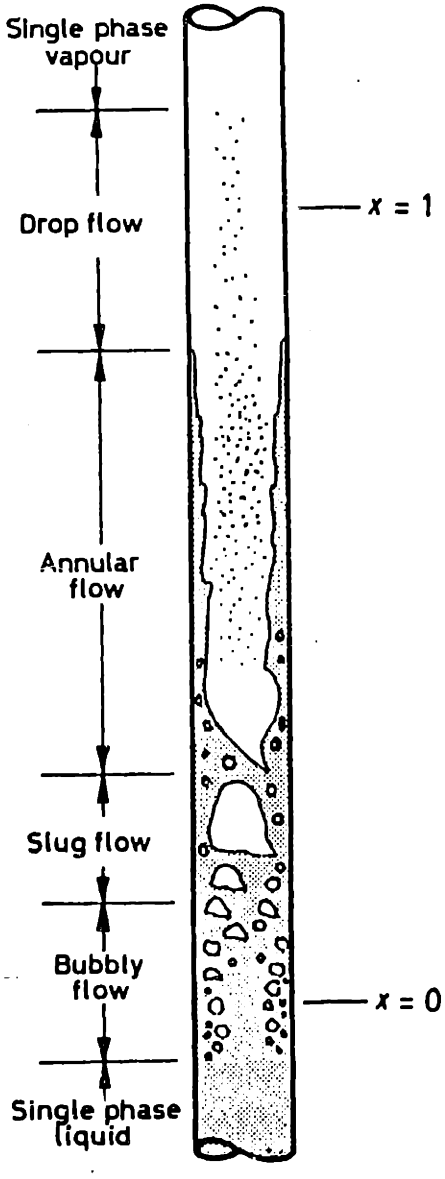

Figure 14.b-Flow patterns in a vertical tube evaporator.

$$\left(-\frac{dp}{dz}_F\right)_{f_o} = \frac{2 f_{f_o} G^2 v_f}{d} \qquad (2.25)$$

where:

$\left(-\frac{dp}{dz}_F\right)$ = two-phase frictional pressure gradient

$\left(-\frac{dp}{dz}_F\right)_{f_o}$ = single-phase frictional pressure gradient

$\Phi^2_{f_o}$ = two-phase frictional multiplier

f_{f_o} = friction factor for the toal flow considered as a liquid

$G = \frac{W}{A}$ = mass velocity (kg/m^2 s)

W = mass flow rate (kg/s)

A = flow cross section area (m^2)

v = specific volume (m^3/kg)

subscript F = frictional

subscript f = liquid

subscript f_o = total flow assumed to be a liquid

subscript g = gas or vapour.

In the homogeneous flow model the two-phase frictional multiplier can be represented as a function of quality, specific volume, and dynamic viscosity:

$$\Phi_{f_o}^2 = \left[1 + x\left(\frac{v_{fg}}{v_f}\right)\right]\left[1 + x\left(\frac{\mu_{fg}}{\mu_f}\right)\right]^{-\frac{1}{4}} \tag{2.26}$$

On the other hand, using the separated flow model, it is possible to show that the two-phase frictional multiplier based on a pressure gradient for total flow assumed to be a liquid ($\Phi_{f_o}^2$) can be obtained as a function of the two-phase frictional multiplier for liquid-alone flow (Φ_f^2) and the quality:

$$\Phi_{f_o}^2 = \Phi_f^2 (1 - x)^{1.75} \tag{2.27}$$

In order to obtain either the multiplier $\Phi_{f_o}^2$ or Φ_f^2, several expressions were developed in terms of other independent flow variables.

2.4.1.1 Lockhart-Martinelli Correlation

This correlation gives Φ_f^2 related to a parameter X, defined as:

$$X = \frac{\left(-\frac{dp}{dz}_F\right)_f}{\left(-\frac{dp}{dz}_F\right)_g} \tag{2.28}$$

Using experimental data, Lockhart and Martinelli found that the two-phase frictional multipliers for liquid-alone (Φ_f^2) and gas-alone (Φ_g^2) flow can be correlated with X considering four types of flow regimes, as shown in Figure 15, whose curves are well represented by the relationships:

$$\Phi_f^2 = 1 + C X^{-1} + X^{-2} \tag{2.29}$$

and

$$\Phi_g^2 = 1 + CX + X^2 \tag{2.30}$$

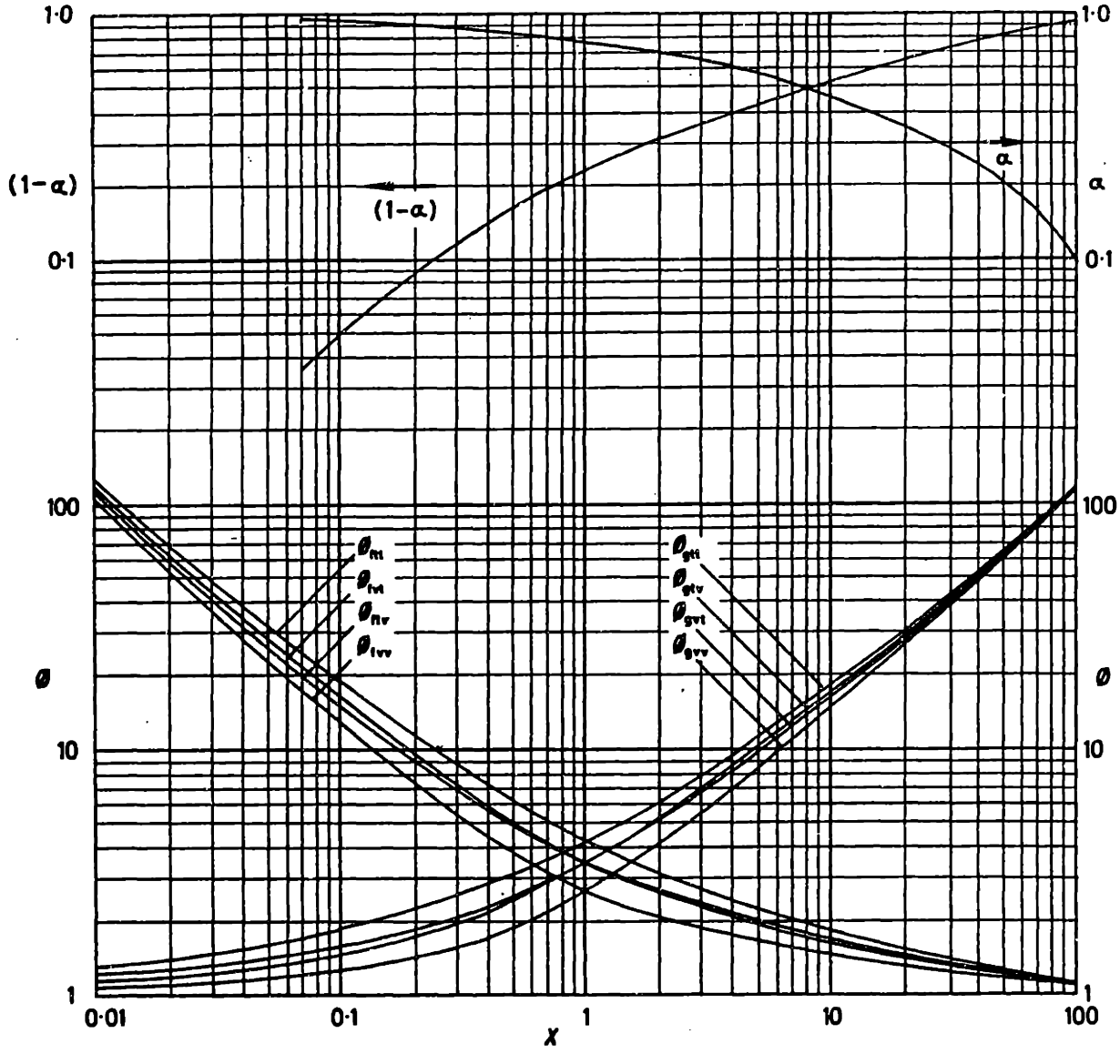

	LIQUID		GAS	
FLOW REGIMES :	turbulent	-	turbulent	(tt)
	viscous	-	turbulent	(vt)
	turbulent	-	viscous	(tv)
	viscous	-	viscous	(vv)

Figure 15-Lockhart-Martinelli correlation.

where C assumes the following values according to the flow regime:

liquid	gas	symbol	C
turbulent	turbulent	tt	20
viscous	turbulent	vt	12
turbulent	viscous	tv	10
viscous	viscous	vv	5

TABLE 2.2 Values of C Considering the Four Types of Flow Regimes

2.4.1.2 Chenoweth and Martin Correlation

The Chenoweth and Martin correlation was also based on an extensive series of experiments made in 1-1/2 inch to 3-inch pipes, using air and water mixtures at pressures from atmospheric to 100 psia, and for a wide range of two-phase flow conditions in horizontal pipes. Their results are shown in Figure 16 and Table 2.3 where the two-phase multiplier (Φ_{fo}^2)

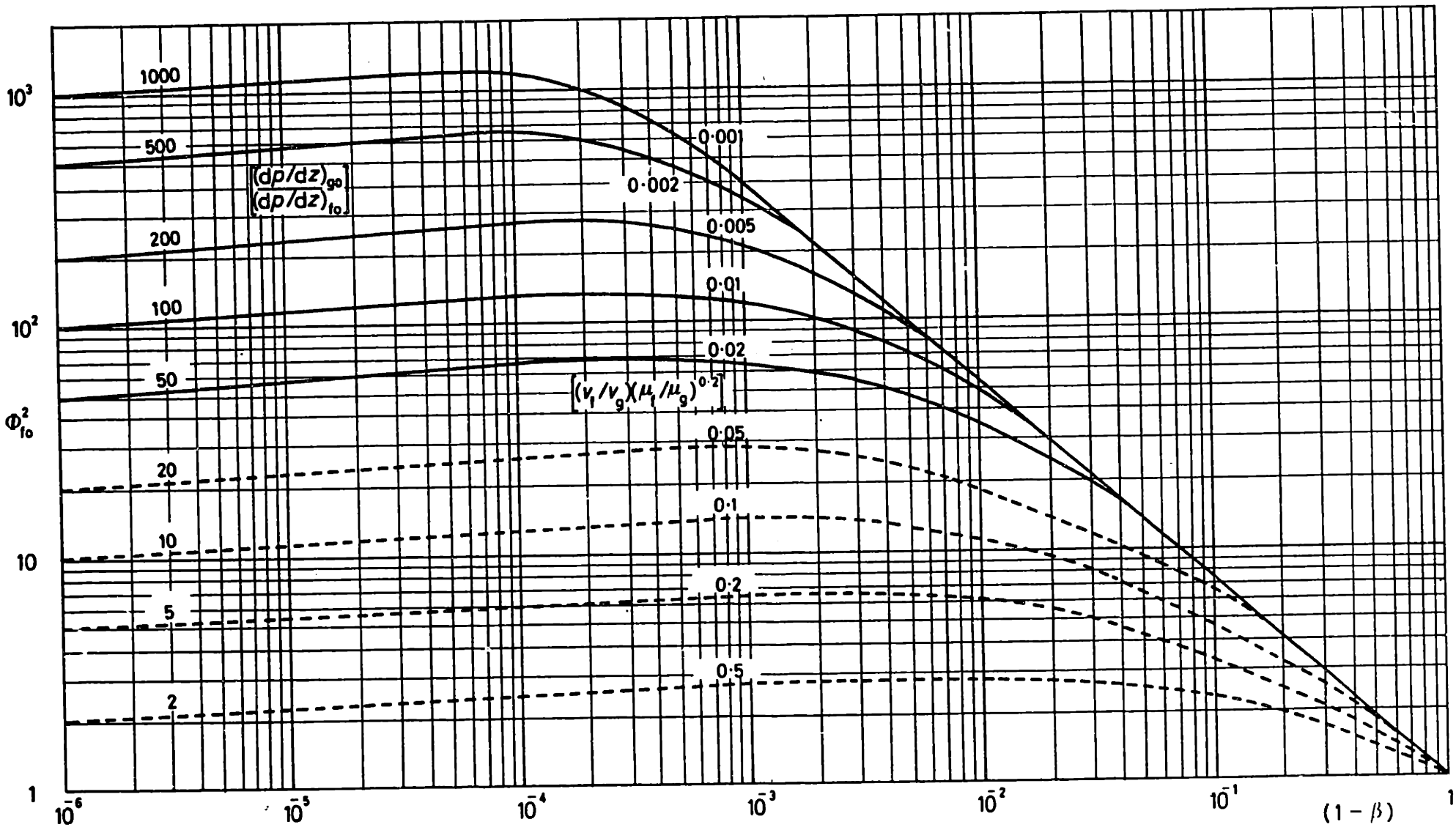

Figure 16-Chenoweth-Martin correlation.

$(1-\beta)$	$\frac{(dp/dz_F)_{go}}{(dp/dz_F)_{fo}}$	50	100	200	500	1000
	0	50.00	100.00	200.00	500.00	1000.00
	$1x10^{-5}$	56.50	113.00	225.00	565.00	1125.00
	$2x10^{-5}$	58.50	117.00	235.00	585.00	1175.00
	$4x10^{-5}$	62.00	124.00	248.00	620.00	1230.00
	$7x10^{-5}$	63.50	127.00	254.00	635.00	1200.00
	$1x10^{-4}$	64.50	129.00	258.00	645.00	1150.00
	$2x10^{-4}$	66.00	132.00	255.00	580.00	950.00
	$4x10^{-4}$	67.50	129.00	249.00	470.00	680.00
	$7x10^{-4}$	65.00	121.00	219.00	385.00	470.00
	$1x10^{-3}$	62.00	115.00	199.00	325.00	370.00
	$2x10^{-3}$	58.00	99.00	153.00	215.00	215.00
	$4x10^{-3}$	50.00	82.00	105.00	120.00	120.00
	$7x10^{-3}$	41.00	60.00	71.00	72.50	72.50
	$1x10^{-2}$	34.50	48.00	53.00	53.00	53.00
	$2x10^{-2}$	24.00	29.20	29.20	29.20	29.20
	$4x10^{-2}$	15.00	16.10	16.10	16.10	16.10
	$7x10^{-2}$	9.90	9.90	9.90	9.90	9.90
	$1x10^{-1}$	7.40	7.40	7.40	7.40	7.40
	$2x10^{-1}$	4.05	4.05	4.05	4.05	4.05
	$4x10^{-1}$	2.22	2.22	2.22	2.22	2.22
	$7x10^{-1}$	1.38	1.38	1.38	1.38	1.38
	1.00	1.00	1.00	1.00	1.00	1.00

TABLE 2.3- Two-phase frictional multiplier(ϕ^2_{fo}) as a function of the superficial liquid volumetric fraction (1-ß) and the single-phase frictional pressure drop gradient ratio $\left((dp/dz_F)_{go}/(dp/dz_F)_{fo}\right)$ (Chenoweth-Martin).

can be obtained as a function of the superficial liquid volumetric fraction $(1-\beta)$ and the ratio $[dp/dz_F)g_o/(dp/dz_F)f_o]$ or the property index $[(v_f/v_g)(\mu_f/\mu_g)^{0.2}]$ which is the inverse of the single-phase frictional pressure gradient ratio.

2.4.1.3 Wallis Analysis for Annular Flow

Considering a steady horizontal flow and developing the one-dimensional equations of motion in annular flow by using average values of the interfacial and wall shear stresses, and then imposing force balances for the gas core and the combined flow, Wallis related the pressure gradient with the interfacial and wall shear stresses through the equations:

$$\left(-\frac{dp_F}{dz}\right) = \frac{4\tau_i}{d\sqrt{\alpha}} \tag{2.31}$$

and

$$\left(-\frac{dp_F}{dz}\right) = \frac{4\tau_w}{d} \tag{2.32}$$

where: α = void fraction

subscript i = interface

The interfacial shear stress was assumed as:

$$\tau_i = \frac{1}{2}(C_f)_i \rho_g v_g^2 = \frac{1}{2}(C_f)_i \rho_g \frac{j_g^2}{\alpha^2} \tag{2.33}$$

being:

$$j_g = \frac{Q_g}{A} = \frac{Q_g \cdot A_g}{A_g \cdot A} = V_g \alpha = \text{vapour volumetric flux} \qquad (2.34)$$

by making the following assumptions:

a) the interfacial shear stress depends on the difference between the gas velocity and some characteristic interface velocity;

b) the gas velocity is much greater than the liquid velocity and consequently one may neglect the liquid velocity.

Finally, the interfacial friction factor, $(C_f)_i$, is given as a function of the dimensionless film thickness (δ/d):

$$(C_f)_i = 0.005 \left[1 + 300 \frac{\delta}{d} \right] \qquad (2.35)$$

As can be seen in Fig. 17, there is a good agreement between Eq. (2.35) and various air-water data obtained by other authors.

2.5 The More Appropriate Method

These pressure drop evaluation methods briefly described are some of the many methods that can be found in the literature. Each one has imperfections as a result of the simplifications and hypotheses assumed through its development.

The correct selection of a method or correlation depends on a very careful and critical analysis to determine which method is the most appropriate for the specific conditions we are dealing with. The best method for one case may be merely satisfactory for another and simply not applicable in yet another.

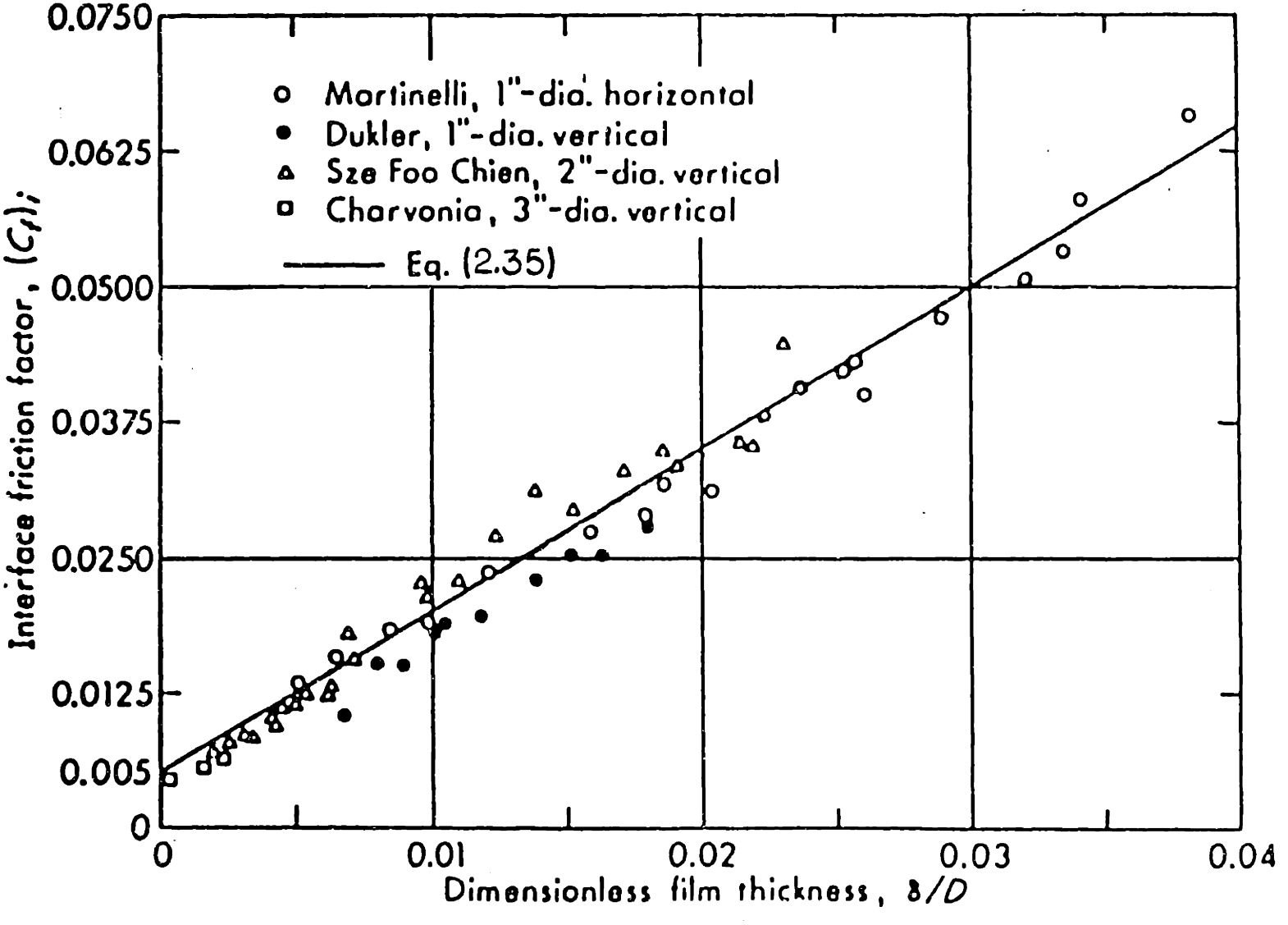

Figure 17-Comparison between equation (2.35) and various air-water data (Wallis).

There is no general rule for this selection. The best general guideline is to match the data base in the correlation and application. Each case has to be carefully analyzed, with all possibilities taken into account and, if having exhausted these attempts we have not found the best method, we will certainly have found a more appropriate one.

CHAPTER 3

EXPERIMENTAL EQUIPMENT

3.1 Experimental Apparatus Objective

The objective of the apparatus design was to carry out experiments using air-water mixtures simulating the steam two-phase flow that occurs in an extraction line. The air velocity and the water flow rate could be changed from one experiment to another, but during any given experiment it was maintained at as constant a level as possible. We tried to keep air and water temperatures constant, with only minimum differences between both to assure almost constant fluid properties. Finally, the test section, made of plaster-of-paris molded on a plexiglas base, could be changed to measure the loss of material after each experiment.

3.2 Apparatus Description

A schematic drawing and a photograph of the apparatus used is shown in Figures 18.a and 18.b, respectively. To describe the several components of the apparatus, let's divide it into six parts named as follows: air inlet system, transition length, developing length, water inlet system, test section, and discharge.

3.2.1 Air Inlet System

The system supplied air to the experiment from a 35 HP compressor and through 6- and 3-inch PVC pipe lines. The air velocity was adjusted by the inlet and the bypass valves. Before leaving the air inlet section, the gas flow velocity and temperature were measured respectively by a thermometer and a pilot tube plus a water manometer.

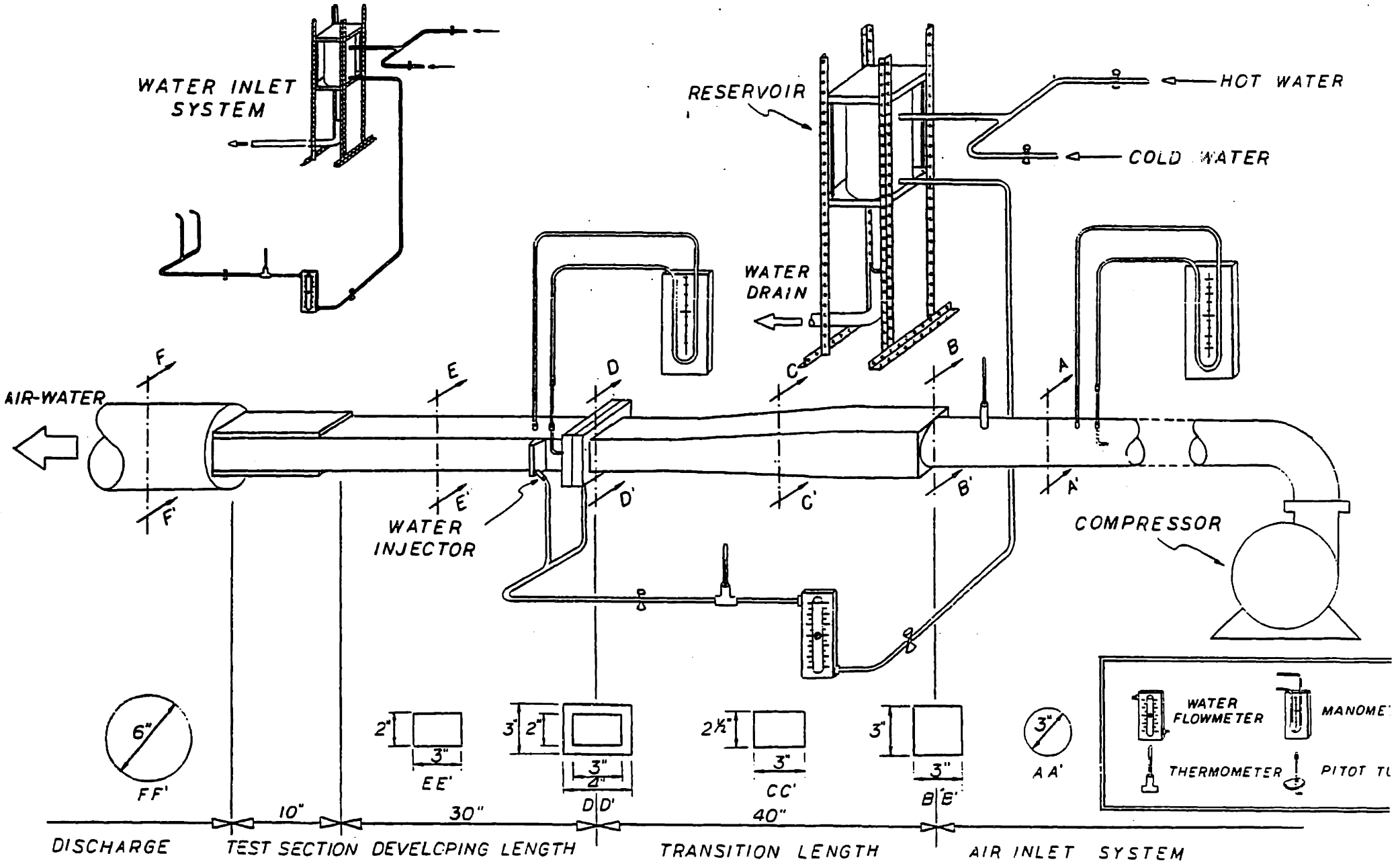

Figure 18.a-Schematic drawing of the experimental apparatus.

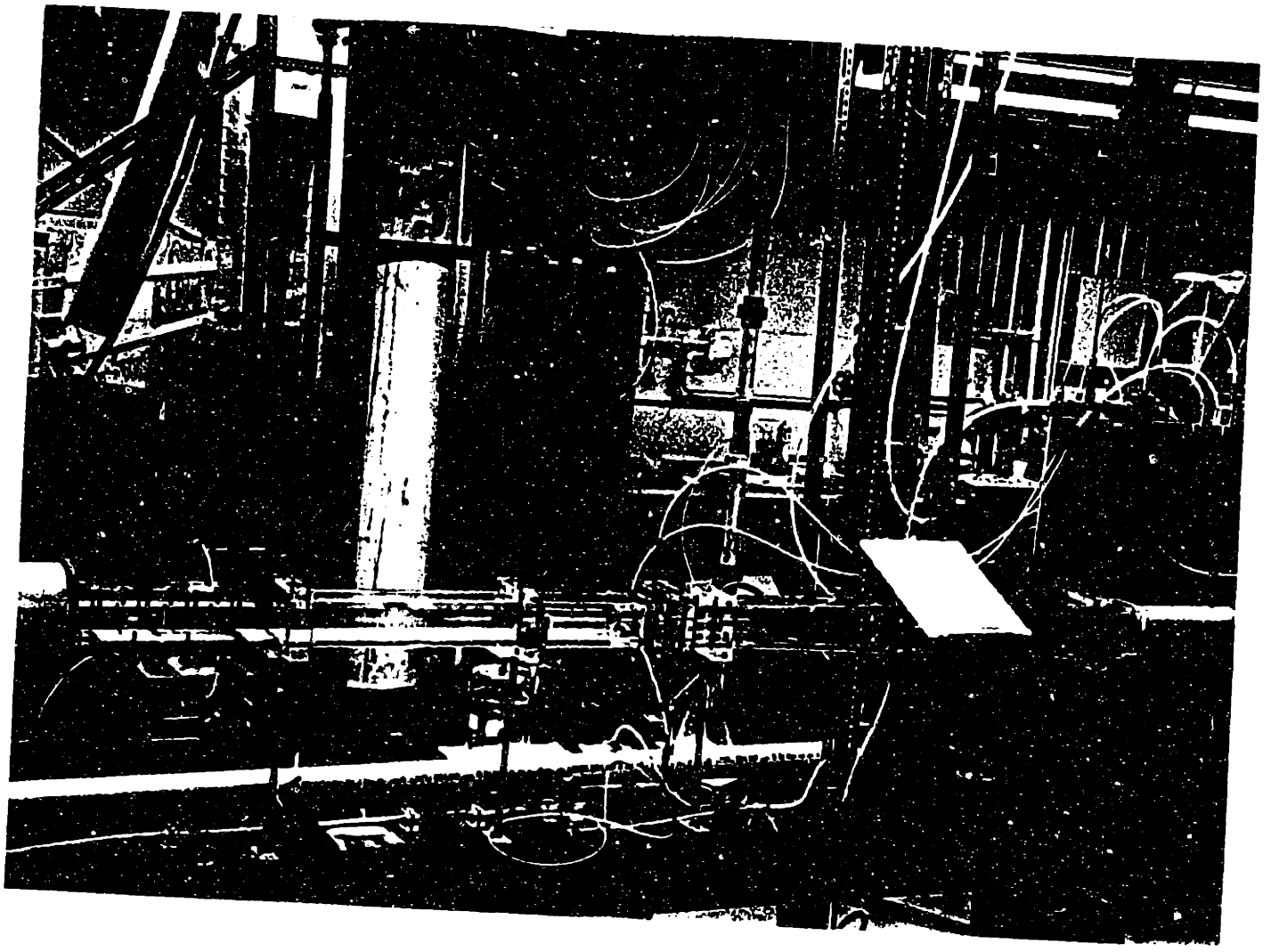

Figure 18.b-Photograph of the experimental apparatus.

3.2.2 Transition Length

A section of pipe called transition length was necessary to change the circular cross section of the 3-inch PVC pipe (air inlet system) to the rectangular cross section (3" x 2") of the next two parts of the apparatus. This section had walls made of 5/16" and 1/2" thickness plexiglas, with a length of 40", and its cross section was progressively narrowed from a 3" x 3" square to a 3" x 2" oblong.

3.2.3 Developing Length

This part was 30" long and had a constant rectangular cross section. The water was injected by two stainless steel tube injectors (1/8" O.D.) located on either side of the beginning of the section and immediately above (almost tangential) the bottom, forming a very thin water film which was developed until reaching the test section. The center line gas velocity was measured once more by a pitot tube and a water manometer. Applying the continuity equation between sections AA' and EE' (Figure 18.a) made it possible to calibrate the manometer to provide the average velocity reading for this section (EE').

3.2.4 Water Inlet System

Cold and hot water were provided to a variable height reservoir. Controlling the hot and cold water flow rates by admission valves one could control the water temperature, and adjusting the reservoir height it was possible to maintain a constant water flow rate for the experiment. The water necessary to form the film was supplied by the reservoir flowing in 1/2-inch diameter plastic and copper pipes, a flowmeter, and some control valves. Before entering the developing length section the water flux was

divided between two 1/4-inch plastic tubes which were coupled to the stainless steel injectors by two standard poly-flow connections 1/4" to 1/4" (Figures 19.a and 19.b).

3.2.5 Test Section

The sketch of the test section can be seen in Figure 20. This section was composed of three pieces of plexiglas, a rubber seal, and a molded plaster-of-paris plate. It could be placed in or removed from the apparatus by screws. After finishing an experiment, the remaining plaster-of-paris layer could be taken away, a new plate could be molded on the plexiglas base, and another experiment carried out.

3.2.6 Discharge

This was the simplest part of the apparatus. It consisted of a 6-inch PVC pipe which received the air and water used in the experiment and discharged the mixture in a reservoir at atmospheric pressure.

3.3 Measurement Methods

3.3.1 Mass Transfer Coefficient and Dissolution Rate

The mass transfer coefficient is easily obtained using Eq. (2.11) if we know the mass flux (J) and the concentration difference between the wall and the bulk ($C_w - C_\infty$):

$$h_d = \frac{J}{C_w - C_\infty} \qquad (2.11a)$$

Referring to Fig. 21, the mass flux can be calculated from the dissolution rate (w) and the density (ρ), as follows:

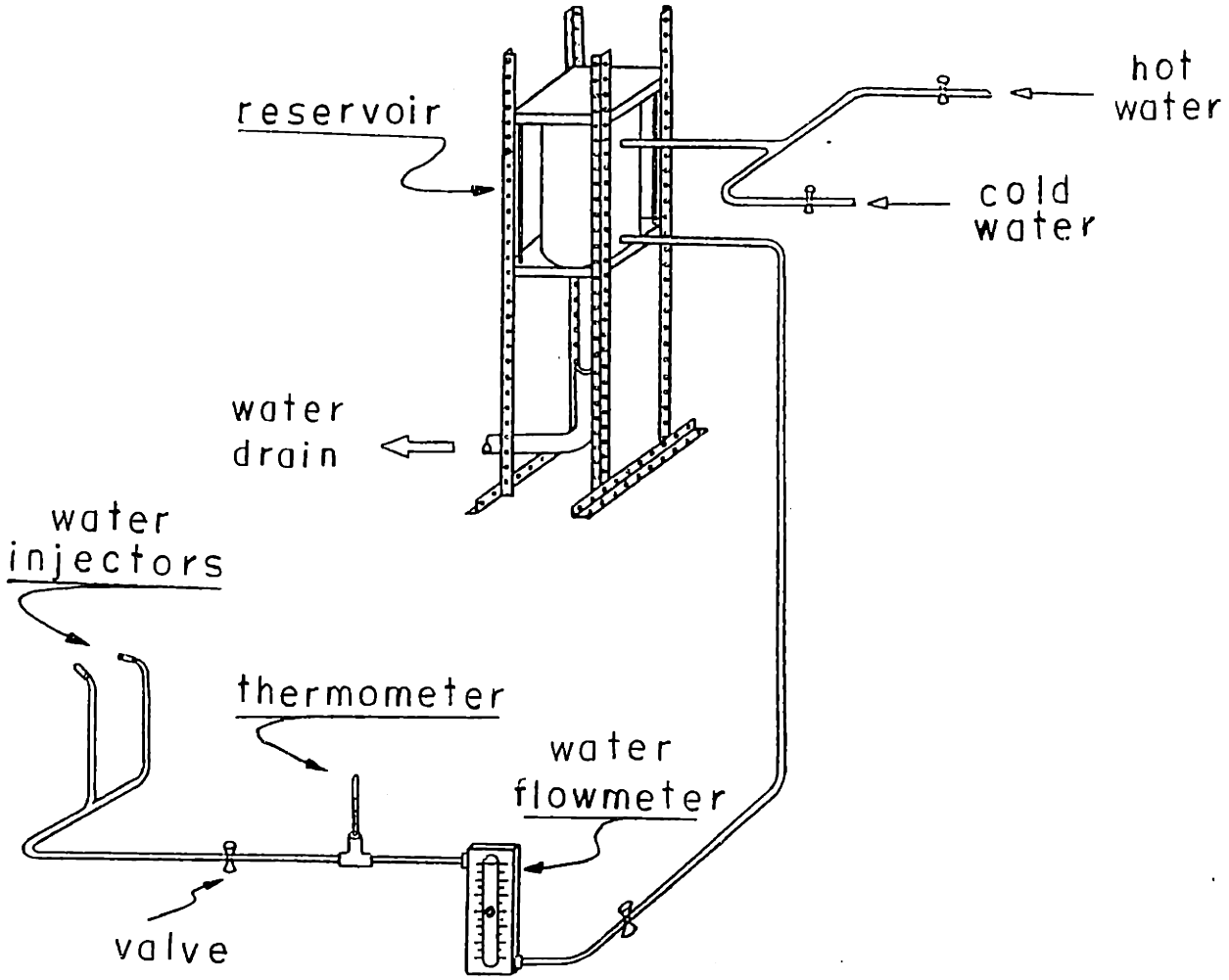

Figure 19.a-Water inlet system.

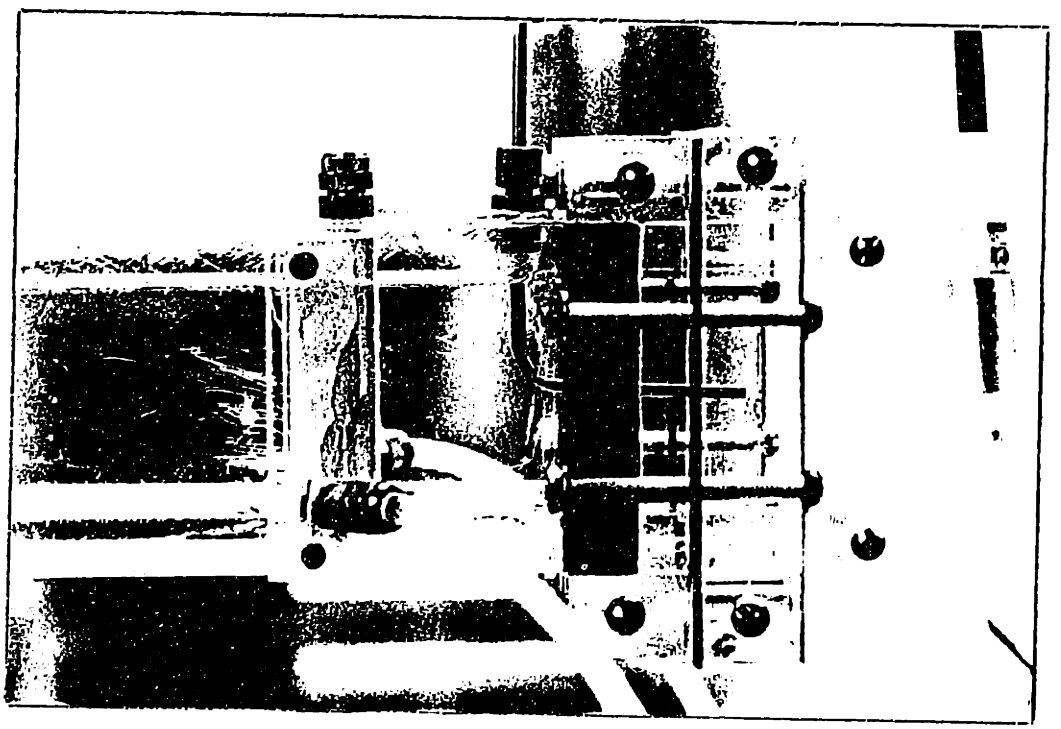

Figure 19.b-Photograph showing the water injectors.

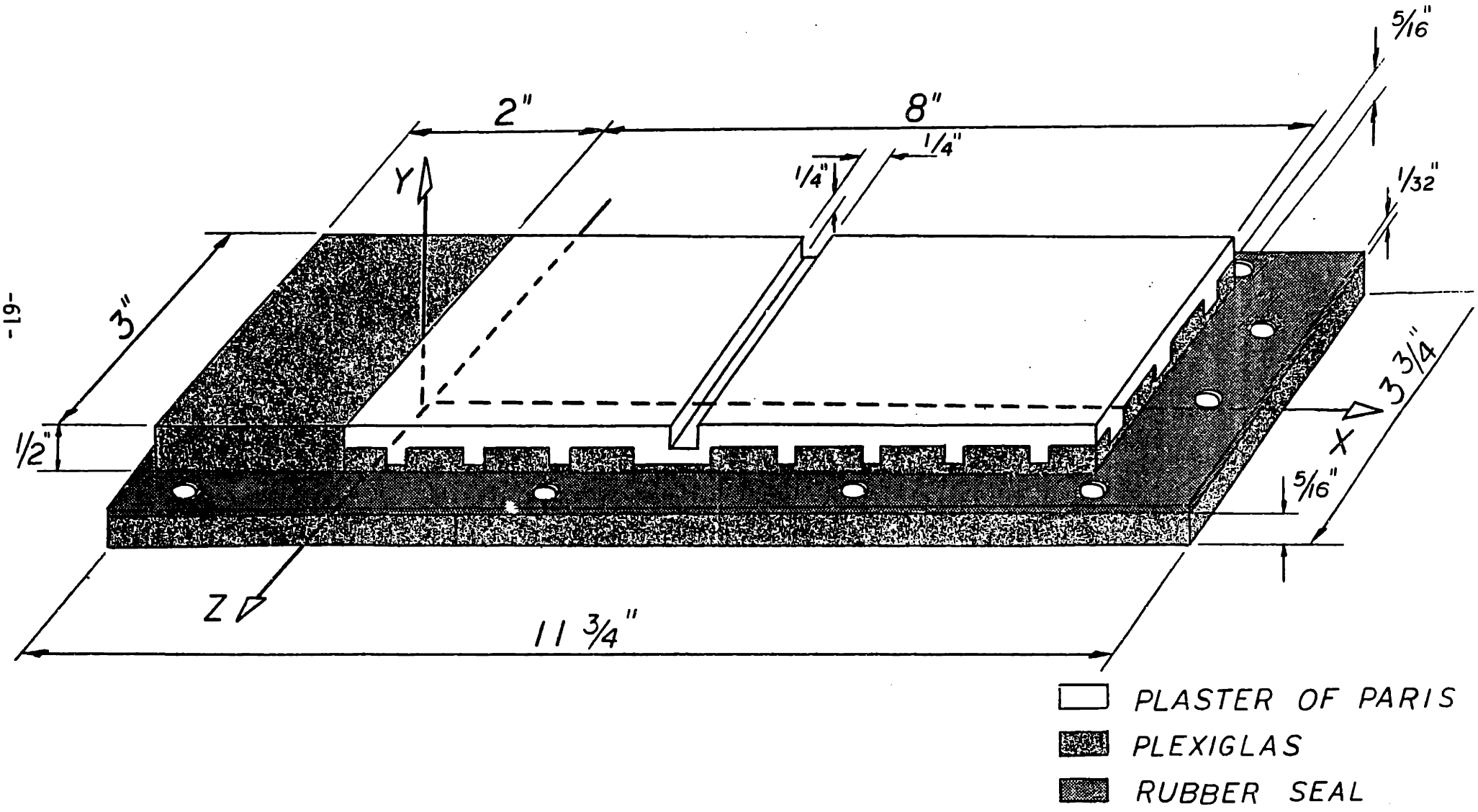

Figure 20-Dimensions of the test section.

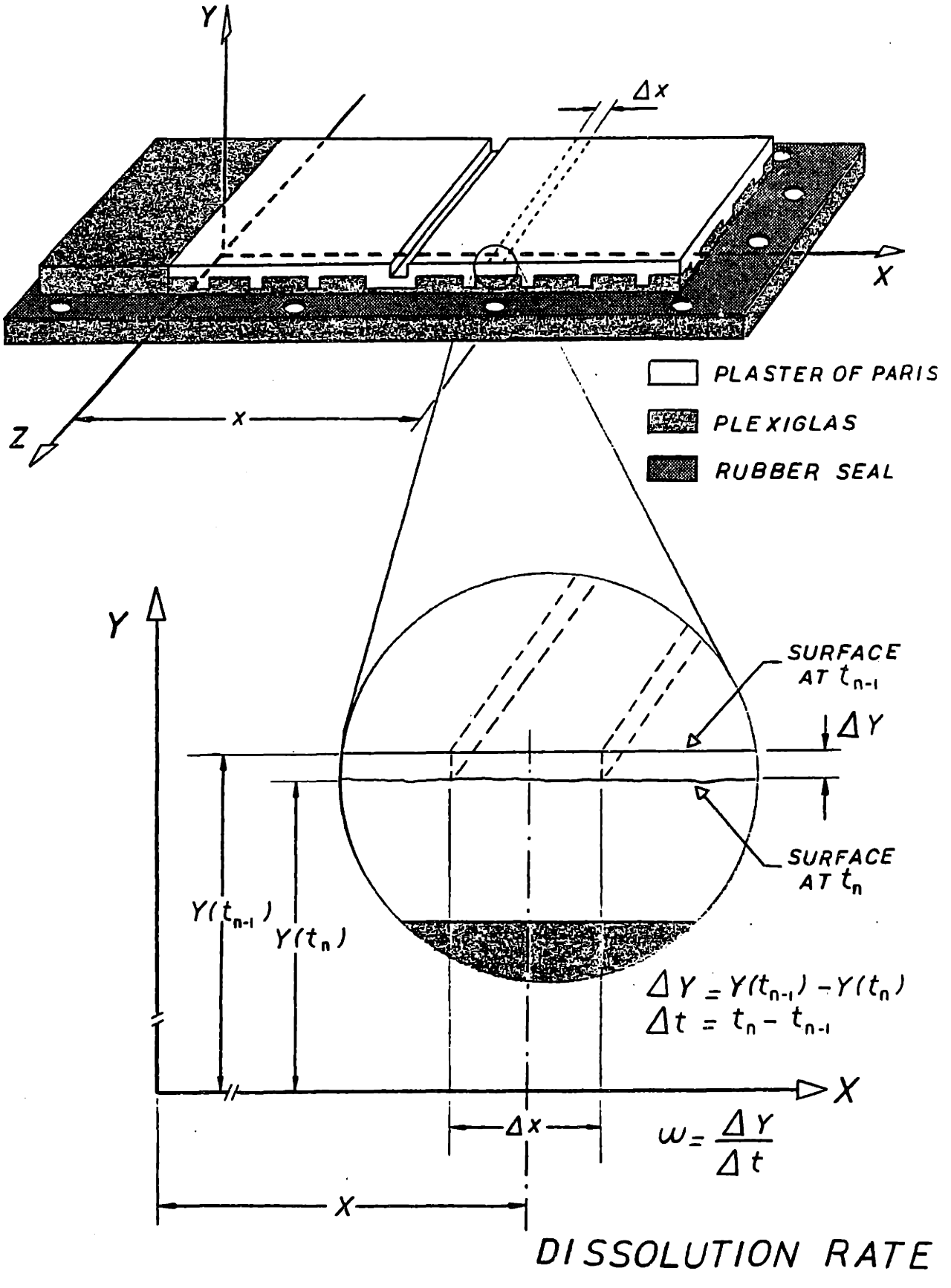

Figure 21-Dissolution rate in a length Δx of the test section.

$$J = w \rho \quad (kg/m^2\ s) \tag{3.1}$$

where

$$w = \frac{\Delta y}{\Delta t} \tag{3.2}$$

$\Delta y = y(t_{n-1}) - y(t_n)$

$\Delta t_n = t_n - t_{n-1}$

$y(t_n)$ = plaster plus plexiglas base thickness at time t_n

t_n = time of the n^{th} measurement

b = plate width.

The density of two plaster samples was measured and found to be 1225 kg/m^3, after checking that the sample's weight had not changed during a period of at least seven days.

3.3.2 Concentration and Solubility

The concentrations were obtained by measuring the solution (water plus calcium sulfate) conductivity with a conductivity meter. This is a very simple method which is based on the fact that the conductivity of a solution varies with the solute concentration. Therefore, if we make conductivity measurements of solutions whose concentration values are known

we can plot a graph of conductivity versus concentration as shown in Fig. A-2, Appendix A. Having this graph and a measured conductivity value it is possible to obtain the corresponding concentration of the solution.

A modified test section was designed and used to collect solution samples for measuring its conductivity in order to find out its bulk concentration. This section had two collector tubes placed in the middle (x = 4") and at the end (x = 8") of the plaster plate (Figs. 22 and 23). With these two values and knowing that the bulk concentration at the beginning (x = 0) of the plate was zero, we could sketch the bulk concentration variation along the plate. This variation was almost linear, as can be seen in Fig. A-3, Appendix A.

The wall concentration was considered to be equal to the solubility of the plaster, whose value obtained was 2585 kg/m^3 at 25°C). This value is very close to the values found by Coney, et al. (2524 kg/m^3 at 20°C) and calculated by Blumberg (2520 kg/m^3 at 23° C).

3.3.3 Diffusion Coefficient

The diffusion coefficient of the plaster solution, necessary to calculate the Sherwood and Schmidt numbers, was calculated by the Nerst equation for diffusion coefficients of electrolytes at infinite dilution (D_0) using ionic conductances given in Table 411 of the Smithsonian Physical Tables [28]. The correction for the effect of finite dilution was made considering the data for $MgSO_4$ and $ZnSO_4$ obtained from Table 16, Appendix 8.10, of Electrolyte Solutions [25]. The calculations, as well as the diffusion coefficients obtained for the temperature range used in the experiments, are presented in Appendix A.

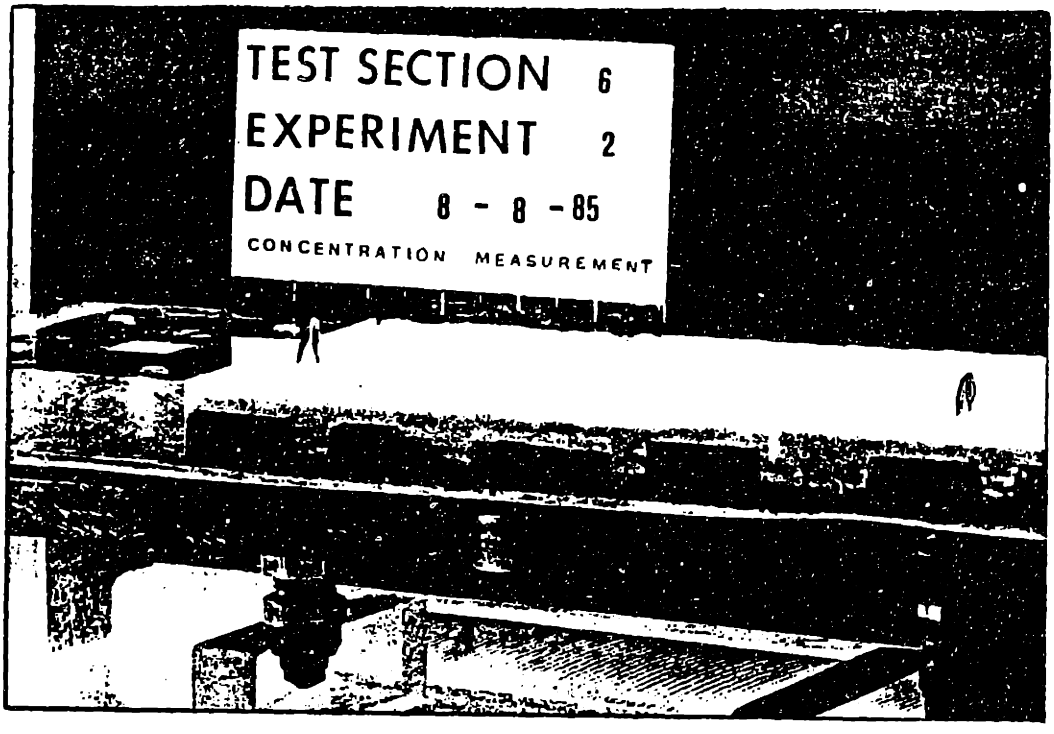

Figure 22-Modified test section photograph.

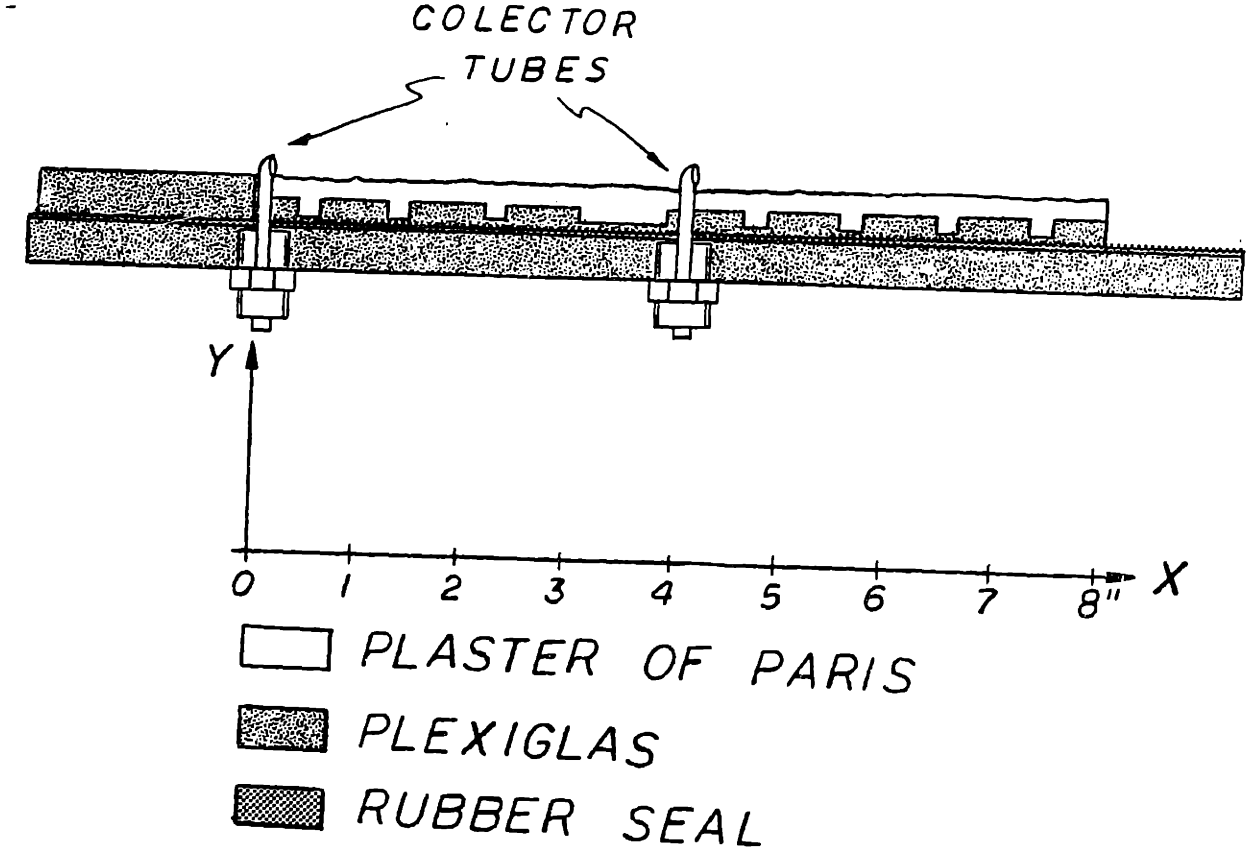

Figure 23-Sketch of the modified test section.

CHAPTER 4

EXPERIMENTAL RESULTS

4.1 Review of Experimental Objectives

The experimental apparatus was designed to carry out the following objectives:

1. To try to reproduce the final geometry presented in a sample of a weld joint with a groove from the extraction line of Millstone Utility, in a planar test section made of plaster of paris;
2. To measure the dissolution rate in the straight part of the test section and in the region around the groove to see how much faster the material was removed from the singularity than from the regular surface; and
3. To calculate the mass transfer coefficient knowing the dissolution rate, the plaster density, and the concentration variation of the plaster in the bulk of the liquid film.

After having calculated the mass transfer coefficients, these values were compared with theoretical values predicted using the Kunz and Yerazunis theory.

Comparing the final shape of the groove in the Millstone extraction line's sample with that obtained in the test sections, we could see that, beyond the geometric similarities, some coincidences were presented, such as:

1. The removal rates on the vertical walls of the groove were greater that the removal rates on the bottom of the groove and on the straight parts upstream and downstream from the singularity; and
2. The enhanced removed rate downstream from the groove was extended for a length greater than that upstream.

4.2 Variations on the Flow Conditions

We have done a set of fifteen experiments using three values of air velocities (100, 125, and 150 ft/s) combined with five values of water flow rates(490,600,700,810, and 940 ml/min). Another experiment was carried out with the modified test section mentioned in Section 3.4.2 to collect solution samples for measuring their conductivity and obtaining their concentrations.

The experiments were labeled as shown in Table 4.1. The label was composed of two numbers: the first referred to the number of the test section used in the experiment and the second referred to the order of the experiment done with the same test section, hence the experiment labeled 3.2 was the second experiment carried out with the test section number 3.

EXPERIMENT	V_{air}(ft/s)	Q_{H_2O}(ml/min)
1.1	100	490
2.1	100	600
3.1	100	700
4.1	100	810
5.1	125	490
6.1	125	600
8.1	125	700
9.1	125	810
10.1	125	940
1.2	150	490
2.2	150	600
3.2	150	700
4.2	150	810
5.2	150	940
6.2	various	various
7.2	100	940

TABLE 4.1-Flow conditions used in the experiments.

4.3 Measurements Obtained from an Experiment

After the plaster surface preparation (Section D.2), measurements of the plate thickness and of the groove geometry were taken using a micrometer and a caliper. The points where the measurements were taken can be seen in Figures 24.a and 24.b.

Each experiment was carried out during a certain number of time intervals (Δt's) depending on how fast the removal rate was for each case; for example, experiment 1.1 was carried out during four time intervals of one hour each, and the experiment 5.2 during two time intervals: the first time interval lasted two hours and the second lasted only one hour because the plaster plate was very thin at the end of this time interval.

After each experiment time interval the test section was removed from the apparatus and another plate thickness and groove geometry measurement set was taken as made at the beginning of the experiment. When the experiment was finished we had obtained a number of measurement sets equal to the numbers of time intervals plus one.

Combining these measurements it was possible to obtain the thickness variation along the plate during each time interval, and dividing the thickness variation by the time interval value, we obtained the dissolution rate (w).

During each experiment the air velocity and the water flow rate were maintained constant and we tried to keep the temperature values of each fluid as close as possible. The temperature of the fluids was taken and recorded every ten

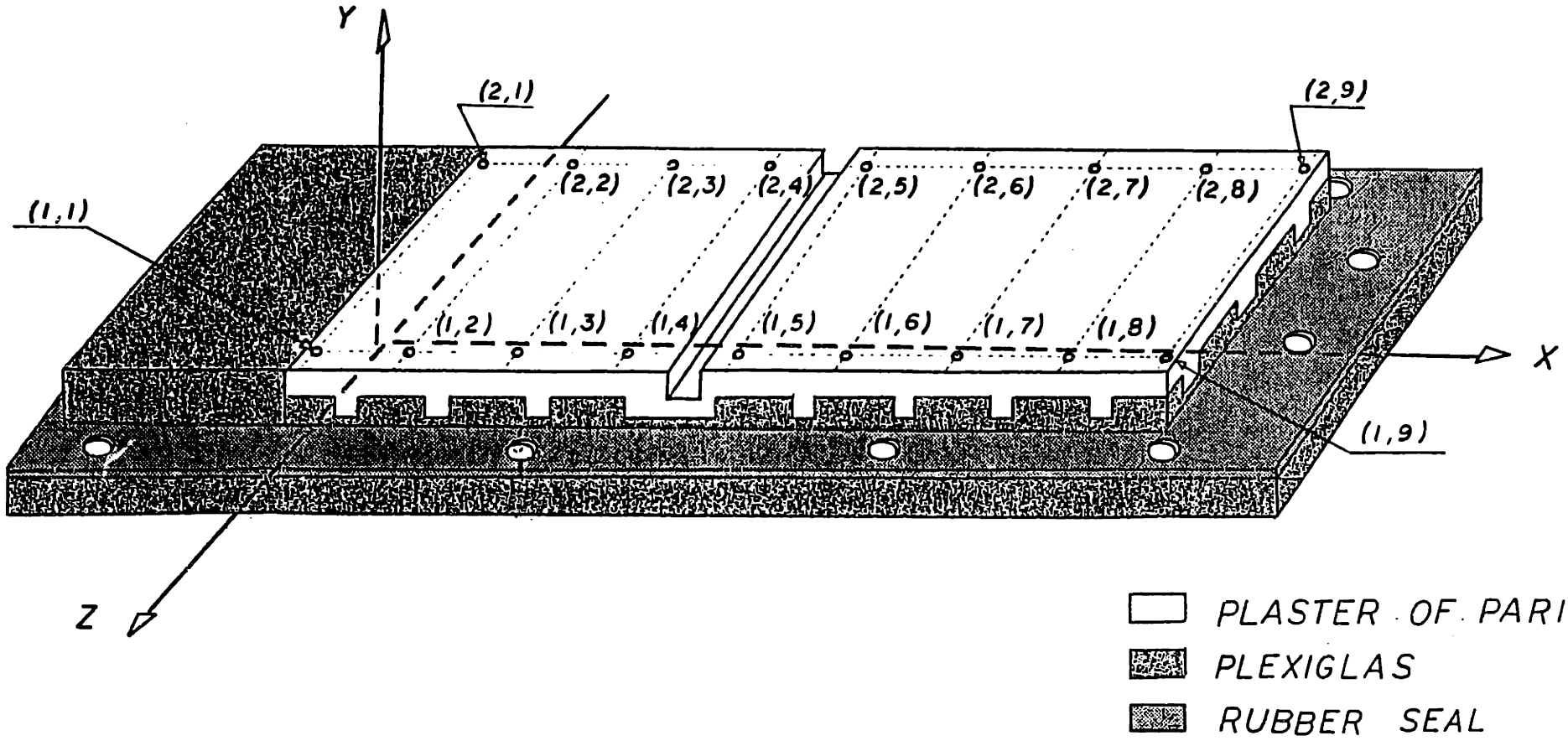

Figure 24.a-Measurements points in the straight part of the test section.

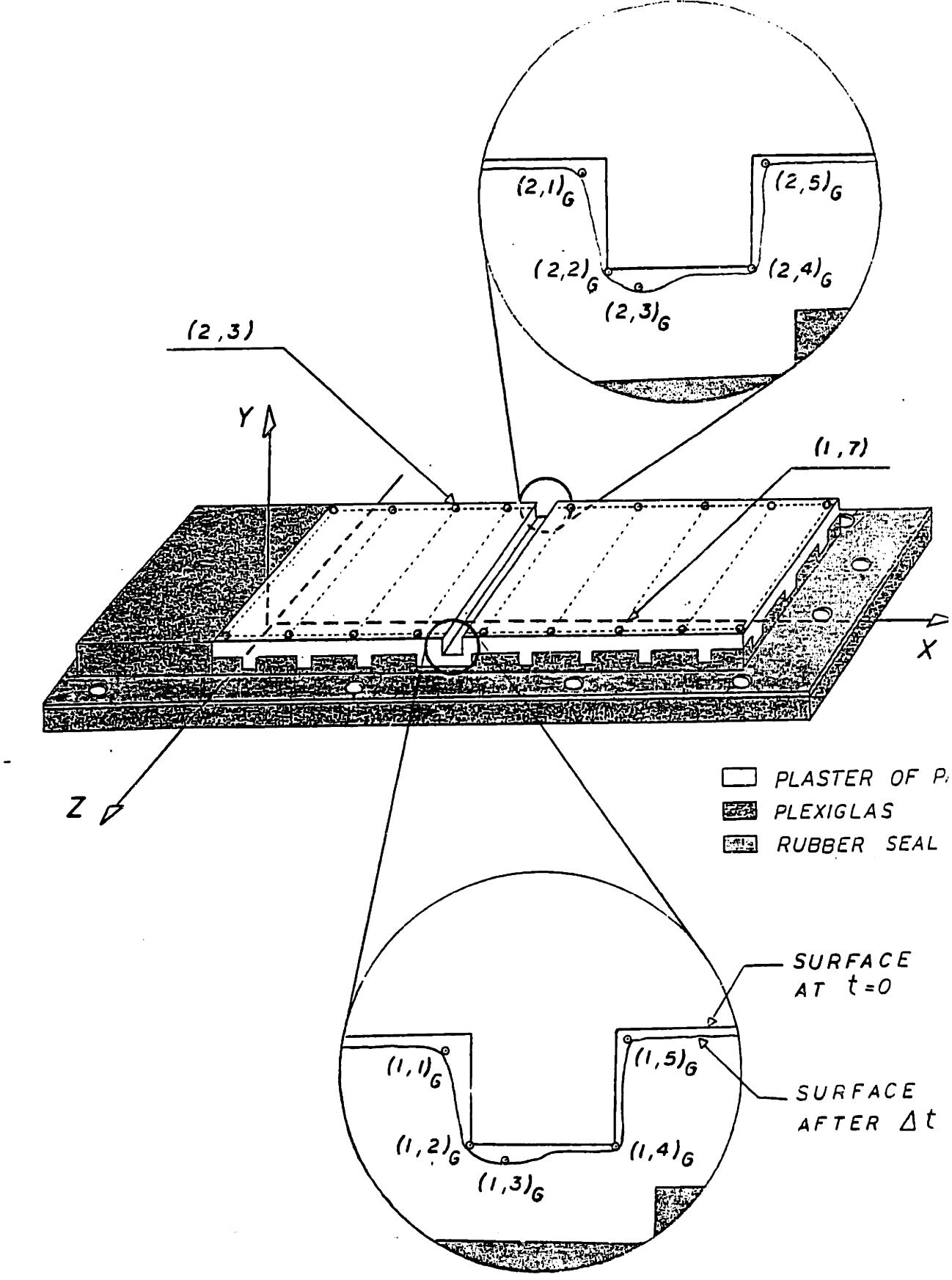

Figure 24.b-Measurement points in the groove region of the test section.

minutes. These temperatures were averaged for the time intervals with the purpose of obtaining the average fluid properties used to calculate the mass transfer coefficients through the theoretical model.

4.4 Experimental Results

The measurements taken for the experiments are presented in Appendix C. Referring to Figure 25, we divided the test sections into eight regions, each region one inch in length, and the region containing the groove was divided into six sub-regions. The seven straight regions were named from A to G and the six sub-regions from I to VI.

As said before, we combined each one of the three air velocities with five water flow rates, so one set of experiments related to one air velocity comprised five experiments, whose results will be presented in the next Sections.

4.4.1 Set of Experiments With V_{air} = 100 ft/s

The dissolution rates and the mass transfer coefficients calculated from the thickness measurements and considering a time interval of 120 minutes are shown in Tables 4.2.a, 4.2.b, 4.3.a, and 4.3.b.

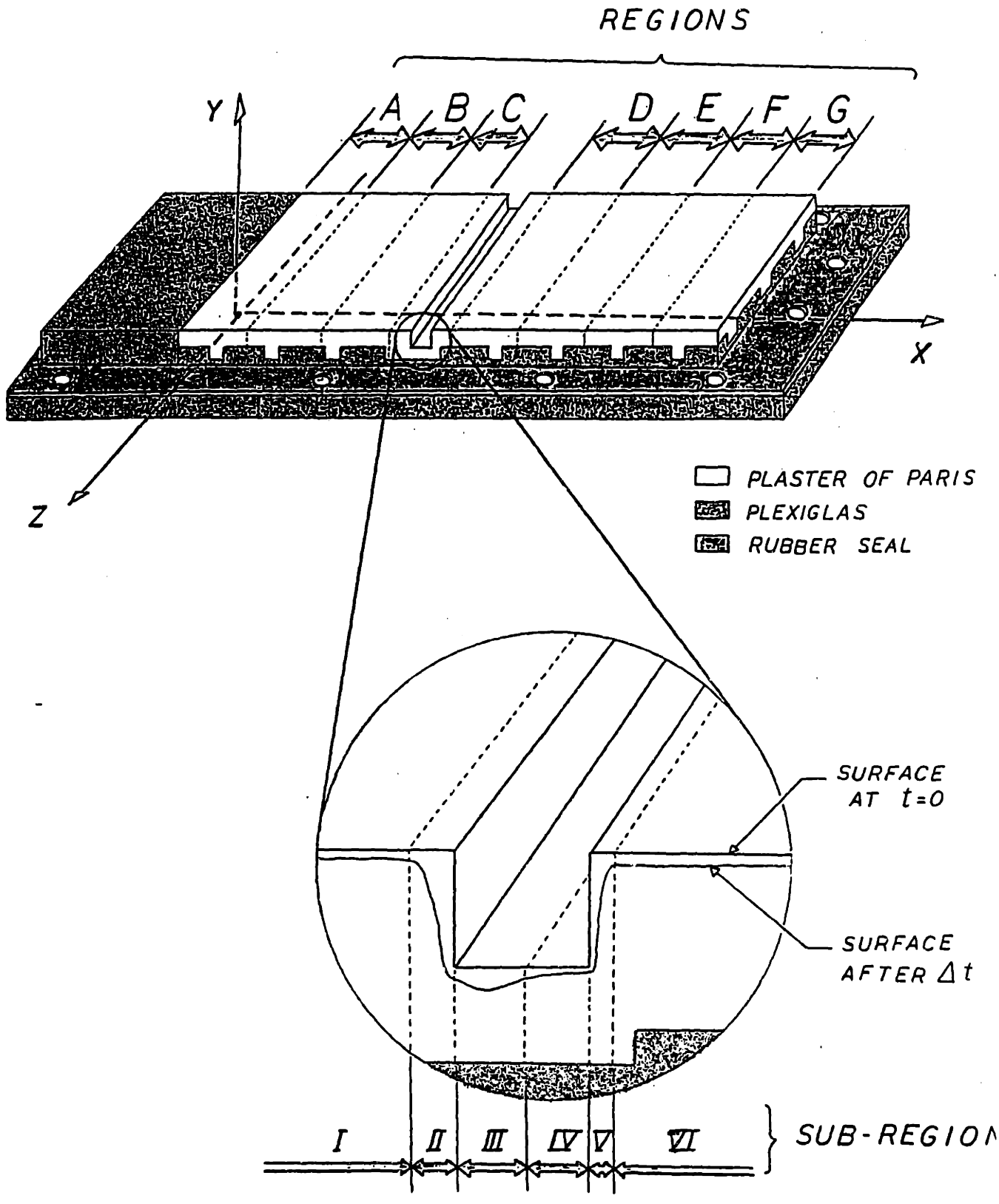

Figure 25-Test section regions and sub-regions.

Q_{H_2O} (ml/min)	REGIONS						
	A	B	C	D	E	F	G
490	7.01	6.99	7.47	10.46	9.93	8.89	9.78
600	8.05	8.56	8.89	8.99	9.53	9.75	10.49
700	8.92	9.07	9.14	10.26	10.46	11.23	11.63
810	11.05	11.15	10.46	10.31	11.33	11.40	11.79
940	12.22	12.73	13.34	13.21	13.79	13.87	14.66

TABLE 4. 2 .a-Dissolution rates($x10^8$ m/s) in the straight regions (V_{air}= 100ft/s and Δt=120 min).

Q_{H_2O} (ml/min)	SUB-REGIONS					
	I	II	III	IV	V	VI
490	8.69	30.73	5.82	3.35	38.30	8.84
600	9.83	34.29	8.64	3.71	34.82	8.59
700	10.06	27.66	8.71	5.67	42.72	10.01
810	11.51	31.47	7.70	4.42	49.48	8.66
940	13.69	36.93	11.84	7.49	32.87	13.39

TABLE 4. 2 .b-Dissolution rates($x10^8$ m/s) in the groove sub-regions(V_{air}= 100 ft/s and Δt=120 min).

Q_{H_2O} (ml/min)	REGIONS						
	A	B	C	D	E	F	G
490	3.98	3.90	4.07	5.43	5.03	4.39	4.70
600	4.57	4.78	4.85	4.67	4.82	4.81	5.04
700	5.06	5.06	4.98	5.33	5.30	5.35	5.59
810	6.27	6.22	5.70	5.36	5.74	5.63	5.66
940	6.93	7.10	7.27	7.07	6.98	6.84	7.04

TABLE 4. 3 .a-Mass transfer coefficients($x10^5$ m/s) in the straight regions(V_{air}= 100 ft/s and Δt=120 min).

Q_{H_2O} (ml/min)	SUB-REGIONS					
	I	II	III	IV	V	VI
490	4.67	16.49	3.12	1.79	20.44	4.71
600	5.28	18.39	4.63	1.98	18.58	4.57
700	5.41	14.84	4.67	3.01	22.80	5.33
810	6.19	16.88	4.12	2.36	26.40	4.61
940	7.36	19.81	6.34	4.00	17.54	7.13

TABLE 4.3.b-Mass transfer coefficients($\times 10^5$ m/s) in the groove sub-regions(V_{air} = 100 ft/s and Δt=120 min).

4.4.2 Set of Experiments with V_{air} = 125 ft/s

The dissolution rates and the mass transfer coefficients for this set of experiments are presented in Tables 4.4.a., 4.4.b., 4.5.a., and 4.5.b.

Q_{H_2O} (ml/min)	REGIONS						
	A	B	C	D	E	F	G
490	9.93	9.09	9.42	9.55	10.03	10.21	10.46
600	10.46	11.63	11.63	12.88	12.98	13.08	13.18
700	10.69	12.50	12.50	13.11	13.03	12.80	13.28
810	11.48	12.42	13.23	13.64	13.77	14.17	15.19
940	13.89	13.97	13.64	14.61	14.96	15.14	15.62

TABLE 4.4.a-Dissolution rates($\times 10^8$ m/s) in the straight regions (V_{air} = 125 ft/s and Δt=120 min).

Q_{H_2O} (ml/min)	SUB-REGIONS					
	I	II	III	IV	V	VI
490	10.72	33.78	7.42	5.64	34.77	9.09
600	12.55	39.98	8.66	5.74	40.39	12.07
700	13.51	39.40	9.93	7.59	41.50	12.80
810	14.27	39.73	10.06	5.82	44.75	13.54
940	14.38	41.20	12.12	7.77	50.50	14.22

TABLE 4.4 .b-Dissolution rates($x10^8$ m/s) in the groove sub-regions(V_{air}= 125 ft/s and Δt=120 min).

Q_{H_2O} (ml/min)	REGIONS						
	A	B	C	D	E	F	G
490	5.64	5.07	5.14	4.96	5.08	5.04	5.03
600	5.94	6.17	6.34	6.69	6.57	6.46	6.33
700	6.07	6.41	6.81	6.81	6.60	6.32	6.38
810	6.51	6.93	7.21	7.08	6.97	6.99	7.30
940	7.88	7.80	7.44	7.58	7.58	7.47	7.51

TABLE 4.5 .a-Mass transfer coefficients($x10^5$ m/s) in the straight regions(V_{air}= 125 ft/s and Δt=120 min).

Q_{H_2O} (ml/min)	SUB-REGIONS					
	I	II	III	IV	V	VI
490	5.76	18.12	3.97	3.01	18.56	4.84
600	6.75	21.45	4.64	3.07	21.55	6.43
700	7.27	21.13	5.32	4.06	22.15	6.82
810	7.67	21.31	5.39	3.11	23.88	7.21
940	7.73	22.10	6.49	4.15	26.95	7.58

TABLE 4.5 .b-Mass transfer coefficients($x10^5$ m/s) in the groove sub-regions(V_{air}= 125 ft/s and Δt=120 min).

4.4.3. Set of Experiments with V_{air} = 150 ft/s

For this set of experiments the results are given in Tables 4.6.a., 4.6.b., 4.7.a., and 4.7.b.

Q_{H_2O} (ml/min)	REGIONS						
	A	B	C	D	E	F	G
490	10.19	10.26	11.18	11.02	11.38	11.96	12.62
600	11.38	11.25	11.40	14.27	15.27	15.29	15.54
700	12.50	12.70	13.44	14.88	16.18	16.56	17.32
810	13.84	14.76	15.93	16.56	17.78	17.81	17.91
940	16.23	17.98	19.13	19.28	18.90	18.39	18.72

TABLE 4.6.a-Dissolution rates($x10^8$ m/s) in the straight regions (V_{air}= 150 ft/s and Δt=120 min).

Q_{H_2O} (ml/min)	SUB-REGIONS					
	I	II	III	IV	V	VI
490	12.98	35.76	8.05	3.00	47.98	11.33
600	13.36	29.21	10.80	2.92	29.49	13.34
700	14.43	38.71	12.07	4.78	33.17	13.74
810	17.86	43.28	11.66	3.78	40.06	15.82
940	20.55	37.29	9.73	3.61	47.70	19.35

TABLE 4.6.b-Dissolution rates($x10^8$ m/s) in the groove sub-regions(V_{air}= 150 ft/s and Δt=120 min).

Q_{H_2O} (ml/min)	REGIONS						
	A	B	C	D	E	F	G
490	5.78	5.73	6.09	5.72	5.76	5.90	6.07
600	6.46	6.28	6.22	7.41	7.73	7.55	7.47
700	7.09	7.09	7.32	7.73	8.19	8.17	8.32
810	7.85	8.24	8.68	8.60	9.00	8.79	8.61
940	9.21	10.04	10.43	10.01	9.57	9.07	9.00

TABLE 4.7 .a-Mass transfer coefficients($x10^5$ m/s) in the straight regions(V_{air}=150 ft/s and Δt=120 min).

Q_{H_2O} (ml/min)	SUB-REGIONS					
	I	II	III	IV	V	VI
490	6.98	19.18	4.31	1.60	25.60	6.04
600	7.18	15.67	5.78	1.56	15.74	7.11
700	7.76	20.77	6.46	2.55	17.70	7.32
810	9.60	23.32	6.24	2.02	21.37	8.43
940	11.05	20.00	5.21	1.93	25.45	10.31

TABLE 4.7 .b-Mass transfer coefficients($x10^5$ m/s) in the groove sub-regions(V_{air}=150 ft/s and Δt=120 min).

4.4.4. Average Mass Transfer Coefficients

Averaging the mass transfer coefficients calculated for the straight regions (A to G) of the experiments, we obtained the average values given in Table 4.8.

The average mass transfer coefficients were calculated using equation 4.1:

$$(h_d)_s = \frac{\sum_{n=1}^{N} (h_d)_n}{N} \; ; \quad n = 1,2,\ldots,N \qquad N = 7 \tag{4.1}$$

Q_{H_2O} (ml/min)	V_{air} (ft/s)		
	100	125	150
490	4.50	5.14	5.86
600	4.79	6.36	7.02
700	5.24	6.49	7.70
810	5.80	7.00	8.54
940	7.03	7.61	9.62

TABLE 4.8-Average mass transfer coefficients($x10^5$m/s).

4.5 Mass Transfer Coefficient Ratios

Dividing the mass transfer coefficients calculated for each sub-region around the groove by the average coefficient for each experiment, made it possible to obtain the mass transfer coefficient ratios presented in Table 4.9. These ratios are good evidence of the influence of this type of singularity (a welding groove) on the variation of the mass transfer coefficient along the groove. They can be used to obtain the mass transfer coefficient in the sub-regions of the groove if we know the average coefficient for the straight part, which can be predicted using a theoretical model, as will be seen in Chapter 5.

EXPERIMENT	SUB-REGIONS					
	I	II	III	IV	V	VI
1.1	1.04	3.66	0.69	0.40	4.54	1.05
2.1	1.10	3.84	0.97	0.41	3.88	0.95
3.1	1.03	2.83	0.89	0.57	4.35	1.02
4.1	1.07	2.91	0.71	0.41	4.55	0.79
7.2	1.05	2.82	0.90	0.57	2.50	1.01
5.1	1.12	3.53	0.77	0.59	3.61	0.94
6.1	1.06	3.37	0.73	0.48	3.39	1.01
8.1	1.12	3.26	0.82	0.63	3.41	1.05
9.1	1.10	3.04	0.77	0.44	3.41	1.03
10.1	1.02	2.90	0.85	0.55	3.54	0.99
1.2	1.19	3.27	0.74	0.27	4.37	1.03
2.2	1.02	2.23	0.82	0.22	2.24	1.01
3.2	1.01	2.70	0.84	0.33	2.30	0.95
4.2	1.12	2.72	0.73	0.24	2.50	0.99
5.2	1.15	2.08	0.54	0.20	2.65	1.07

TABLE 4.9-Mass transfer coefficient ratios.

As can be inferred from the mass transfer coefficient ratios and observed in the final geometry presented by the groove region, indeed the groove presents four distinct sub-regions since the ratios of regions I and VI are very close to the unit, i.e., the mass transfer coefficients for these two regions don't differ much from the average mass transfer coefficient for the straight regions of the experiment.

CHAPTER 5

THEORETICAL RESULTS

5.1. Introduction

The theoretical model used to predict the average mass transfer coefficients, considering the flow conditions used in the experiments, was that of Kunz and Yerazunis theory [22] with the friction velocity obtained from the interfacial shear stress. This was calculated using both the Wallis analysis for annular flow and the Chenoweth-Martin correlation.

Recalling the block diagram pictured in Figure 13, the Kunz and Yerazunis theory gives us a graphical relationship between the liquid Reynolds (Re_L) and Schmidt (Sc_L) numbers with the friction Stanton number (St*). The friction velocity (v*) can be calculated from the wall sheer stress, which was obtained from a force balance over a section of infinitessimal length, and knowing a pressure drop estimate. Since the friction Stanton number relates the mass transfer coefficient with the friction velocity, having two of these values it is possible to obtain the third.

5.2. Average Property Values

In order to apply the Kunz and Yerazunis theory, the Wallis analysis, and the Chenoweth-Martin correlation, we needed to know several properties of the fluids. These property values usually vary with the temperature, hence we used average property values considering the average fluid temperatures of each experiment. The average fluid temperatures related with the experiments are shown in Table 5.1.

EXPERIMENT	V_{air} (ft/s)	Q_{H_2O}(ml/min)	$\overline{T}_{air}$(°F)	$\overline{T}_{H_2O}$(°F)
1.1	100	490	84.3	84.7
2.1	100	600	82.4	82.8
3.1	100	700	83.3	84.5
4.1	100	810	81.5	82.3
7.2	100	940	96.6	98.0
5.1	125	490	85.8	86.3
6.1	125	600	86.7	86.4
8.1	125	700	88.1	85.9
9.1	125	810	89.1	87.7
10.1	125	940	88.1	87.7
1.2	150	490	96.9	89.5
2.2	150	600	98.6	95.1
3.2	150	700	99.3	91.7
4.2	150	810	99.0	98.0
5.2	150	940	97.6	97.4

TABLE 5.1-Average fluid temperatures.

The values of the fluid properties in the range of temperatures from 80° F to 100° F are tabulated in Appendix B, and every property value used in the theoretical model was related to the average temperatures of the experiments.

5.3. Friction Velocity Estimate Using the Wallis Analysis

From the Wallis analysis for a steady horizontal annular flow, the pressure gradient can be related with the interfacial and the wall shear stresses using equations (2.31) and (2.32):

$$\left(-\frac{dp}{dz}_F\right) = \frac{4\tau_i}{d\sqrt{\alpha}} \tag{2.31}$$

$$\left(-\frac{dp}{dz}_F\right) = \frac{4\tau_w}{d} \tag{2.32}$$

The interfacial and the wall sheer stresses are given, respectively, by:

$$\tau_i = (C_f)_i \frac{\rho_g V_g^2}{2} \tag{2.33}$$

$$\tau_w = (C_f)_w \frac{\rho_f V_f^2}{2} \tag{5.1}$$

The wall friciton factor is a function of the liquid Reynolds number:

$$(C_f)_w = \frac{16}{Re_f} \tag{5.2}$$

where:

$$Re_f = \frac{4\Gamma}{\mu_f} \tag{5.3}$$

$$\Gamma = \frac{\dot{m}_f}{w} \tag{5.4}$$

$$v_f = \frac{\dot{m}_f}{\rho_f \delta a} \tag{5.5}$$

And the interfacial friction factor is given as a function of either the dimensionless film thickness (δ/d) or the void fraction (α):

$$(C_f)_i = 0.005\left[1 + 300\frac{\delta}{d}\right] \tag{5.6.a}$$

$$(C_f)_i = 0.005\left[1 + 75(1-\alpha)\right] \tag{5.6.b}$$

The void fraction, as used in this last equation (5.6.b), is related with the dimensionless film thickness considering the assumption of thin films in pipes (Figure 26), i.e.:

$$\alpha = \frac{\frac{\pi(d-2\delta)^2}{4}}{\frac{\pi d^2}{4}} = 1 - 4\frac{\delta}{d} + 4\frac{\delta^2}{d^2} \tag{5.7}$$

Neglecting the second order term:

$$\alpha \approx 1 - 4\frac{\delta}{d} \qquad \text{or} \qquad \frac{\delta}{d} \approx \frac{1-\alpha}{4} \tag{5.8}$$

In the case of our experiments we can relate the void fraction with other dimensionless film thickness (δ/b). Referring to figure 27, we can see that:

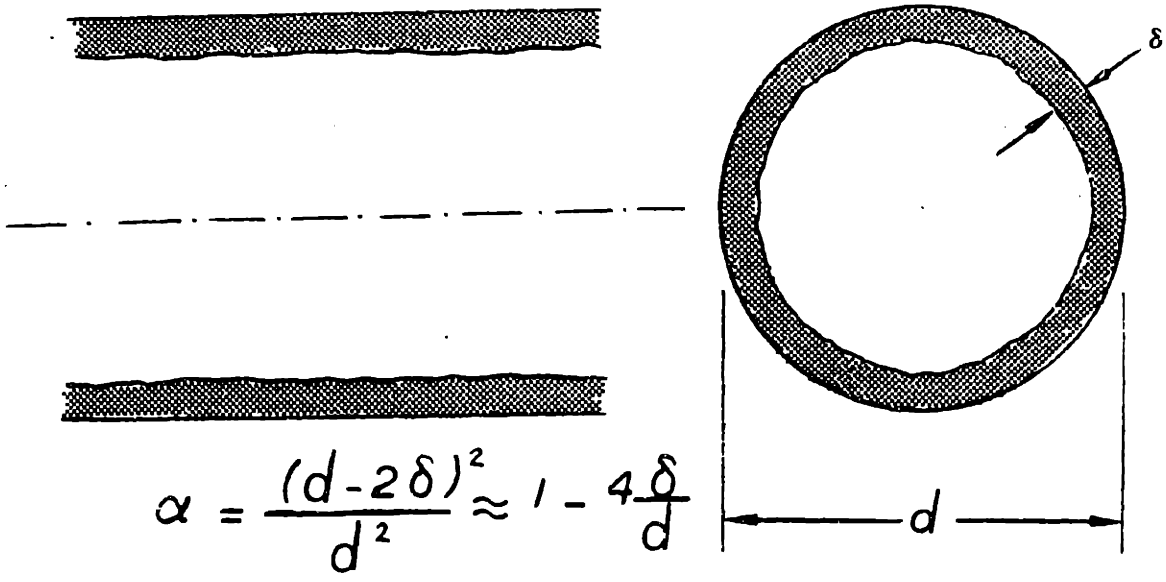

Figure 26-Void fraction for annular flow in a pipe.

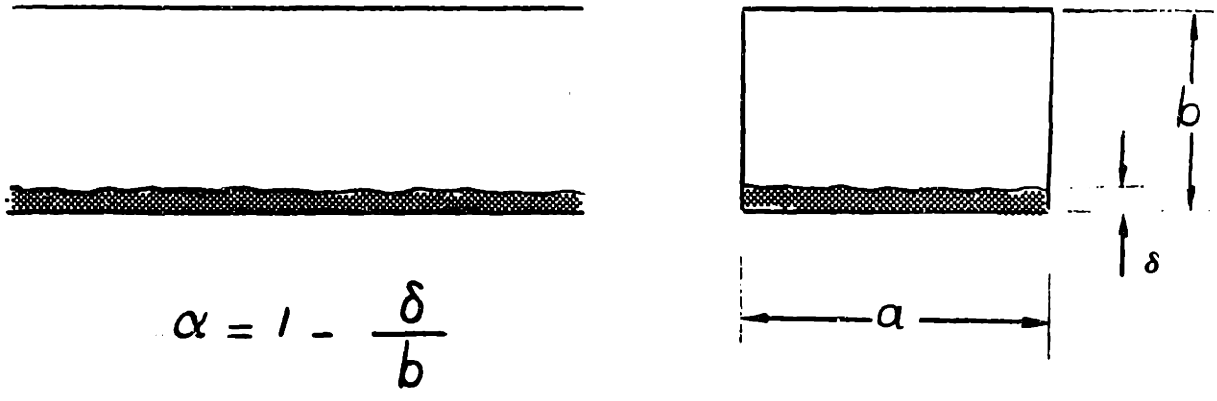

Figure 27-Void fraction for the experimental apparatus flow.

$$\alpha = \frac{(b-\delta)a}{ba} = 1 - \frac{\delta}{b} \tag{5.9}$$

From equations (2.31), (2.32), and (5.9):

$$\tau_i = \tau_w\sqrt{\alpha} = \tau_w\sqrt{1 - \frac{\delta}{b}} \tag{5.10}$$

Using equations (5.9) in equation (5.6):

$$(C_f)_i = 0.005\left[1 + 75\frac{\delta}{b}\right] \tag{5.11}$$

Substituting equations (5.2), (5.5), and (5.11) in equation (5.10):

$$0.005\left(1 + 75\frac{\delta}{b}\right)\rho_g V_g^2 = \frac{16}{Re_f}\frac{\rho_f}{2}\left(\frac{\dot{m}_f}{\rho_f \delta a}\right)^2\sqrt{1 - \frac{\delta}{b}} \tag{5.12}$$

If we use δ, a, and b in ft, ρ_g and ρ_f in lbm/ft^3, $\dot{m}_f$ in lbm/hr, and V_g in ft/s, we can write:

$$\frac{\delta^2(1+450\delta)}{\sqrt{1-6\delta}} = \frac{3.9506 \times 10^3}{Re_f\,\rho_f\,\rho_g}\left(\frac{\dot{m}_f}{V_g}\right)^2 \tag{5.13}$$

The right-hand side of equation (5.13) can be calculated using the values of the fluid properties in the experiment; then, let's call:

$$\Delta = \Delta\left(Re_f, \rho_f, \rho_g, \dot{m}_f, V_g\right) \tag{5.14}$$

Using this new variable in equation (5.13), the film thickness will be one of the roots of the following equation:

$$2.025\times10^{5}\delta^{6}+900\delta^{5}+\ \delta^{4}+6\Delta^{2}\delta-\Delta^{2}=0 \tag{5.15}$$

knowing the value of the film thickness, we can obtain the wall shear stress. Using the same units used to obtain equation (5.13), we have:

$$\tau_w = \frac{3067\times10^{-7}}{Re_f\,\rho_f}\left(\frac{\dot{m}_f}{\delta}\right)^2 \quad (lbf/ft^2) \tag{5.16}$$

The friction velocity was defined in the work of Kunz and Yerazunis as:

$$v^* = \sqrt{\frac{\tau_w g_c}{\rho_f}} \quad (ft/s) \tag{5.18}$$

where:

g_c = gravitational constant = 32.2 $\frac{lbm\ ft}{lbf\ s^2}$

Therefore, using the Wallis analysis for annular two-phase flow we could obtain the friction velocities shown in Table 5.2.

EXPERIMENT	Re_f	$\Delta(x10^7 ft^2)$	$\delta(x10^4 ft)$	$\tau_w(lbf/ft^2)$	$v^*(ft/s)$
1.1	573	6.39	6.96522	.07461	.19666
2.1	692	7.90	7.65420	.07675	.19944
3.1	819	9.09	8.14633	.07791	.20098
4.1	934	10.67	8.73688	.07953	.20302
7.2	1187	11.66	9.08465	.07811	.20138
5.1	582	4.03	5.65945	.11141	.24037
6.1	712	4.96	6.21719	.11305	.24120
8.1	819	5.87	6.70604	.11498	.24414
9.1	962	6.73	7.12927	.11606	.24533
10.1	1116	7.77	7.59843	.11857	.24796
1.2	591	2.82	4.81293	.15176	.28058
2.2	746	3.36	5.20997	.15390	.28263
3.2	857	4.00	5.64304	.15542	.28398
4.2	1022	4.49	5.94488	.15718	.28567
5.2	1187	5.18	6.34186	.16028	.28848

TABLE 5.2-Results obtained applying the Wallis analysis for annular two-phase flow.

5.4. Friction Velocity Estimate Using the Chenoweth-Martin Correlation.

Another way that can be used to estimate the wall shear stress, and consequently the friction velocity, is to obtain the two-phase pressure drop gradient using the separated flow model and making a force balance over a section of infinitesimal length. According to the separated flow model, the two-phase pressure drop gradient is calculated using the Fanning equation for the total liquid plus vapour flow, assumed to be a liquid, corrected by the two-phase frictional multiplier, which can be obtained from the Chenoweth-Martin correlation. Therefore, we used the following set of equations:

1. Separated flow model:

$$\left(-\frac{dp}{dz}_F\right) = \left(-\frac{dp}{dz}_F\right)_{f_o} \Phi_{f_o}^2 \qquad (2.24)$$

$$\left(-\frac{dp}{dz}_F\right)_{f_o} = \frac{2 f_{f_o} G^2 v_f}{d} \qquad (2.25)$$

$$f_{f_o} = 0.079 \left(\frac{G d}{\mu_f}\right)^{-0.25} \qquad (5.18)$$

$$G = \frac{m_f - m_g}{A} = \text{mass velocity} \qquad (5.19)$$

2. Chenoweth-Martin correlation:

$$\Phi_{f_o}^2 = \Phi_{f_o}^2 \left[\left(\frac{v_f}{v_g}\right)\left(\frac{\mu_f}{\mu_g}\right)^{0.2} ; (1-\beta) \right] \qquad (5.20)$$

where:

$$\left(\frac{v_f}{v_g}\right)\left(\frac{\mu_f}{\mu_g}\right)^{0.2} = \text{property index}$$

$(1-\beta)$ = superficial liquid volumetric fraction

$$\beta = \frac{Q_g}{Q_f + Q_g} \qquad (5.21)$$

Q = volumetric rate of flow (volume/time)

The liquid and vapour mass flow rates, as well as the average properties for each experiment are shown in Table 5.3.

EXPERIMENT	$\dot{m}_f$ (lbm/hr)	$\dot{m}_g$ (lbm/hr)	ρ_f (lbm/ft^3)	ρ_g (lbm/ft^3)	μ_f (lbm/ft.hr)	μ_g (lbm/ft.hr)
1.1	64.827	1093.95	62.113	.07293	2.515	.04488
2.1	79.380	1099.05	62.132	.07327	2.596	.04469
3.1	92.610	1093.95	62.113	.07327	2.515	.04469
4.1	107.163	1099.05	62.132	.07327	2.596	.04469
7.2	124.362	1068.60	62.019	.07124	2.110	.04582
5.1	64.827	1367.44	62.094	.07293	2.434	.04488
6.1	79.380	1361.06	62.094	.07259	2.434	.04507
8.1	92.610	1361.06	62.113	.07259	2.515	.04507
9.1	107.163	1354.69	62.094	.07225	2.434	.04525
10.1	124.362	1361.06	62.094	.07259	2.434	.04507
1.2	64.827	1602.90	62.075	.07124	2.353	.04582
2.2	79.380	1602.90	62.038	.07124	2.191	.04582
3.2	92.610	1595.25	62.057	.07090	2.272	.04600
4.2	107.163	1595.25	62.019	.07090	2.110	.04600
5.2	124.362	1602.90	62.019	.07124	2.110	.04582

TABLE 5.3-Mass flow rates and average properties for each experiment.

Table 5.4 shows the calculated values of the mass velocity, friction factor, and single-phase frictional pressure gradient for the total flow assumed to be a liquid.

EXPERIMENT	G ($lbm/ft^2.hr$)	f_{fo}	$\left(-\frac{dp_F}{dz}\right)_{fo}$ ($x10^3 lbf/ft^3$)
1.1	27810.648	.01152	3.43740
2.1	28282.320	.01156	3.56715
3.1	28599.840	.01144	3.60992
4.1	28949.112	.01150	3.71562
7.2	28631.088	.01095	3.46674
5.1	34374.408	.01084	4.94141
6.1	34570.560	.01082	4.99086
8.1	34888.080	.01089	5.11147
9.1	35084.472	.01078	5.12142
10.1	35650.128	.01074	5.26679
1.2	40025.448	.01034	6.39714
2.2	40374.720	.01014	6.38415
3.2	40508.640	.01022	6.47781
4.2	40857.912	.01001	6.45934
5.2	41454.288	.00998	6.62523

TABLE 5.4-Mass velocity, friction factor, and single-phase frictional pressure gradient calculated for the experiment flow conditions.

Using the property index, the superficial liquid volumetric fraction, and the Chenoweth-Martin correlation (Table 2.3 and Figure 16), we obtained the two-phase frictional multipliers (Table 5.5).

EXPERIMENT	$(1-\beta)\times10^{-5}$	$\left(\frac{v_f}{v_g}\right)\left(\frac{\mu_f}{\mu_g}\right)^{0.2}$	ϕ_{fo}^2
1.1	7.0	406.60	516.42
2.1	8.5	403.30	516.26
3.1	9.9	404.40	520.29
4.1	11.5	404.40	514.87
7.2	13.3	423.75	530.38
5.1	5.5	401.14	511.64
6.1	6.8	407.68	516.94
8.1	8.0	407.88	521.97
9.1	9.2	412.20	529.50
10.1	10.7	407.68	522.73
1.2	4.7	420.24	524.04
2.2	5.7	422.57	531.17
3.2	6.6	423.73	536.44
4.2	7.7	426.11	543.12
5.2	8.9	423.75	543.44

TABLE 5.5-Superficial liquid volumetric fraction, property index , and two - phase frictional multiplier obtained from Chenoweth - Martin correlation.

The two-phase pressure drop gradient was calculated using equation (2.24), the wall shear stress obtained from a force balance, and the frictional velocity from equation (5.17). These results can be seen in Table 5.6.

EXPERIMENT	$\left(-\frac{dp}{dz}_F\right)$ (lbf/ft^3)	τ_w (lbf/ft^2)	v^* (ft/s)
1.1	1.77514	.15467	.28317
2.1	1.84158	.16334	.29095
3.1	1.87821	.17015	.29699
4.1	1.91306	.17426	.30052
7.2	1.83869	.17326	.29993
5.1	2.52822	.21381	.33298
6.1	2.57998	.22177	.33912
8.1	2.66803	.23349	.34792
9.1	2.71179	.24314	.35508
10.1	2.75311	.24848	.35897
1.2	3.35236	.27846	.38006
2.2	3.39107	.28983	.38786
3.2	3.47496	.30090	.39513
4.2	3.50820	.31196	.40245
5.2	3.60041	.32574	.41125

TABLE 5.6-Two-phase pressure drop gradient, wall shear stress , and frictional velocity calculated for the experiment flow conditions.

5.5. Friction Stanton Number for Mass Transfer

The friction Stanton number for heat transfer was defined in Section 2.3.2. The difference between this dimensionless and the regular Stanton number concerns the use of the friction velocity, defined as a function of the wall shear stress (equation 5.18), instead of the usual velocity of the fluid or the average velocity of the mixture in the case of a two-phase flow. Using the heat and mass transfer analogy, it is possible to define a friction Stanton number for mass transfer as follows:

$$St_d^* = \frac{h_d}{v^*} \qquad (5.22)$$

where h_d is the mass transfer coefficient and v* is the friction velocity. Using the Kunz and Yerazunis results (Figure 11), we can obtain the product $Pr_L \cdot St^*$ knowing the liquid Reynolds (Re_L) and Prandtl (Pr_L) numbers, or for the case of mass transfer:

$$Sc_L \, St_d^* = \text{function } (Re_L, Sc_L) \qquad (5.23)$$

In our experiments we obtained $0.5 \times 10^3 < Re_L < 1.2 \times 10^3$ and $580 < Sc_L < 850$. For this range of Re_L, we can see in figure 11 that the curves for $Sc_L = 500$ and $Sc_L = 1000$ are almost horizontal and the correspondent values of the product $Sc_L \cdot St_d^*$ are 0.45 and 0.60, respectively. Therefore, using the Schmidt numbers calculated in Appendix B for the temperature range from 80° F to 100° F and the product $Sc_L \cdot St^*_d$ obtained from the curves of figure 11, it was possible to arrive at the friction Stanton numbers shown in Table 5.7.

T(°F)	Sc_L	$St_d^* \times 10^4$
80.0	850.350	6.898
82.5	810.575	7.137
85.0	772.549	7.365
87.5	736.821	7.579
90.0	702.618	7.784
92.5	670.451	7.977
95.0	639.515	8.163
97.5	610.498	8.337
100.0	582.559	8.505

TABLE 5.7-Friction Stanton numbers obtained using the Kunz and Yerazunis theory.

5.6. Mass Transfer Coefficient Prediction

Now we have the friction Stanton number obtained from the Kunz and Yerazunis theory and two estimates of the friction velocity: using the Wallis analysis for annular flow and the separated flow model combined with the Chenoweth-Martin correlation. Using equation (5.22) we can predict the mass transfer coefficient for the flow conditions of our experiments, as shown in Table 5.8.

EXPERIMENT	$St_d^* x10^4$	Wallis analysis		Chenoweth -Martin	
		v^* (ft/s)	$h_d (x10^5 m/s)$	v^* (ft/s)	$h_d (x10^5 m/s)$
1.1	7.365	.19666	4.41	.28317	6.36
2.1	7.137	.19944	4.34	.29095	6.33
3.1	7.365	.20098	4.51	.29699	6.67
4.1	7.137	.20302	4.42	.30052	6.54
7.2	8.337	.20138	5.12	.29993	7.62
5.1	7.579	.24037	5.55	.33298	7.69
6.1	7.579	.24120	5.57	.33912	7.83
8.1	7.365	.24414	5.48	.34792	7.81
9.1	7.579	.24533	5.67	.35508	8.20
10.1	7.579	.24796	5.73	.35897	8.29
1.2	7.784	.28058	6.66	.38006	9.02
2.2	8.163	.28263	7.03	.38786	9.65
3.2	7.977	.28398	6.90	.39513	9.61
4.2	8.337	.28567	7.26	.40245	10.23
5.2	8.337	.28848	7.33	.41125	10.45

TABLE 5.8-Mass transfer coefficients predicted for the experiment flow conditions.

5.7. Comparison Between Experimental and Theoretical Results

Let's define the ratio r as the mass transfer coefficient predicted using the Kunz and Yerazunis theory over the mass transfer coefficient obtained from the experiments:

$$r = \frac{(h_d)\ \text{theoretical}}{(h_d)\ \text{experimental}} \qquad (5.24)$$

Additionally, let's use the subscripts W and CM to indicate if the mass transfer coefficient was predicted using the Wallis analysis or the Chenoweth-Martin correlation, respectively. Calculating the ratios r_W and r_{CM} we obtained the data shown in Table 5.9.

EXPERIMENT	$(h_d)_{exp}$ ($x10^5$m/s)	$(h_d)_W$ ($x10^5$m/s)	r_W	$(h_d)_{CM}$ ($x10^5$m/s)	r_{CM}
1.1	4.50	4.41	1.02	6.36	0.71
2.1	4.79	4.34	1.10	6.33	0.76
3.1	5.24	4.51	1.16	6.67	0.79
4.1	5.80	4.42	1.31	6.54	0.89
7.2	7.03	5.12	1.37	7.62	0.92
5.1	5.14	5.55	0.93	7.69	0.69
6.1	6.36	5.57	1.14	7.83	0.81
8.1	6.49	5.48	1.18	7.81	0.83
9.1	7.00	5.67	1.23	8.20	0.85
10.1	7.61	5.73	1.33	8.29	0.92
1.2	5.86	6.66	0.88	9.02	0.65
2.2	7.02	7.03	1.00	9.65	0.73
3.2	7.70	6.90	1.12	9.61	0.80
4.2	8.54	7.26	1.17	10.23	0.83
5.2	9.62	7.33	1.31	10.45	0.92

TABLE 5.9-Mass transfer coefficient ratios.

Plotting a graph (Figure 28) of the experimental versus theoretical mass transfer coefficient values, we can see that most of the predicted values using the Wallis analysis lie in the first octant whereas all the predicted values using the Chenoweth-Martin correlation lie in the upper octant. In other words, usually the experimental values obtained were greater than the predicted values using the Wallis analysis and smaller than the values calculated using the Chenoweth-Martin correlation, but with a good agreement between the experimental and theoretical results considering the order of magnitude. (10^{-5}).

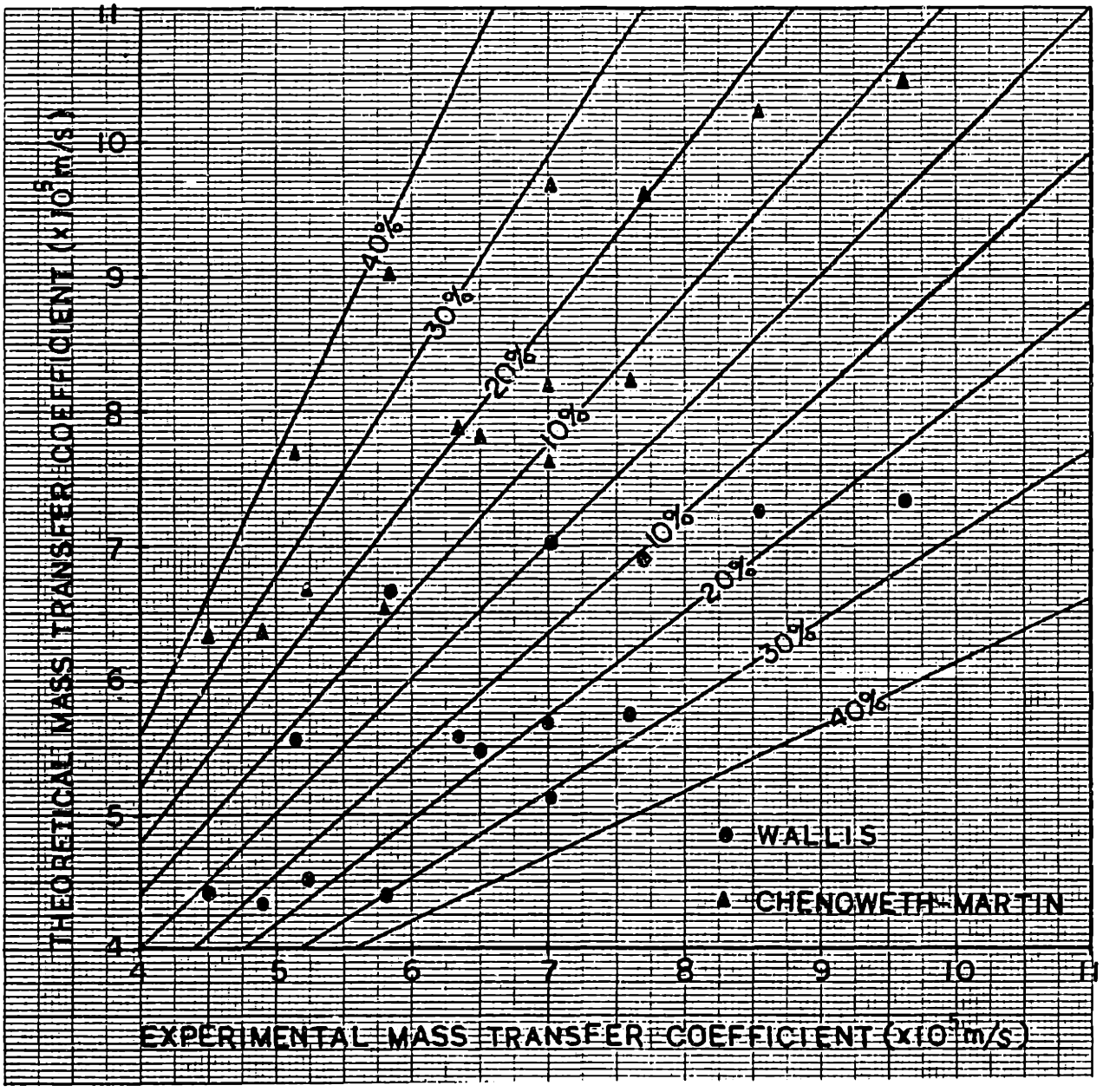

Figure 28-Comparison between experimental and theoretical mass transfer coefficient values.

CHAPTER 6

CONCLUSIONS AND SUGGESTIONS

6.1. Conclusions

An experimental investigation was carried out to obtain data which permitted a calculation of the dissolution rate and the mass transfer coefficient along a planar model simulated fitting, pipe and backup ring made of plaster of paris and submitted to a two-phase air-water flow.

The goals pursued during this work were to reproduce the final geometry found in a sample of a weld joint with a groove, obtained from the extraction line of the Millstone Utility Power Plant, and to correlate the ratio of peak in the singularity to the mean mass transfer coefficient in the straight part of the model.

The results obtained from the experiments showed that it was possible to reproduce the geometry presented in the sample using the experimental apparatus with a two-phase air-water flow simulating the steam two-phase flow which exists in an actual extraction pipeline, and a planar model made of plaster of paris.

Comparing the final groove geometry in the test sections and the calculated mass transfer coefficients using the experimental data, we can see that there are four distinct sub-regions in the groove whose ratios between local and mean mass transfer coefficients give quantitative evidence of how much faster the material was removed from each sub-region of the groove than from the regular surface.

Additionaly, the average mass transfer coefficients obtained from the experiments were compared with theoretical values calculated considering the flow conditions of each experiement and using the Kunz and Yerazunis theory, showing that exists good agreement between the experimental values and the theoretical predictions of this coefficient. Therefore, knowing the ratios between local and mean mass transfer coefficients for the sub-regions of the groove and using the theoretical model to calculate the mass transfer coefficient for the flow conditions, it is possible to predict the coefficient in a groove sub-region. Using this prediction with other variables in the Sanchez-Caldera model for erosion-corrosion [27] will enable us to obtain the wear rate in this kind of singularity, one of the locations that undergoes the greatest metal removal rates in an extraction line.

6.2. Suggestions for Future Work

The apparatus designed for this experimental work can be used to study other types of singularities that exist in a

pipeline. For example, there are regions in which, instead of a separation between two welded parts of a pipeline, one may have an excess of welding material in the joint, forming a weld bead, and places where drain tubes or measuring devices are connected with the line. Considering the characteristics of each case, it is possible to modify the test section adding either a "weld bead" or a "button" made of the plaster of paris, trying to simulate the singularity's geometry.

To obtain better control of the fluid temperatures and consequently better accuracy of the fluid properties, two improvements can be made in the water and air inlet systems:

1. The water temperature can be controlled using electrical resistances in the reservoir, and the water inlet lines as well as the reservoir must be insulated to prevent heat transfer from the water to the environment or vice-versa; and

2. A heat exchanger using cold water and electrical resistances must be inserted in the air inlet system in order to reduce or increase the air temperature.

With these improvements in the inlet systems and an additional control system to maintain the desired fluid temperatures, it will be possible to carry out experiments with exactly the same air and water temperatures instead of trying to

keep these temperatures as close as possible.

This project and several other works on the corrosion-erosion problem have been developed with the aim of obtaining data to predict the wear rate and the remaining lifetime in extraction pipelines of power plants, i.e., we have a problem and we are trying to know more about this problem and its consequent effects, in order to improve the safety of the operating conditions of the equipment. Another approach that could be used to treat this problem is to try to eliminate, or at least to minimize, the causes of the problem. In the case of weld joints, preventive action consists in providing a weld joint with a good penetration, eliminating the lack of material between the welded parts, and using a special device to smooth the pipe internal surface.

As a final suggestion, we believe that it is possible to design and construct a wear meter, and based on experiments similar to those developed in this work, we will be able to predict how the wear meter will work. Preliminary designs of a wear meter are presented in Appendix E. The basic idea of this wear meter is that it could be placed near the "worst" wear rate regions of a steam line. The component labeled as 'B' could be removed from time to time, such as in periodic scheduled outages of the power plant. Taking measurements of the slope which exists on the top of 'B' will give us an indication of the actual wear that was developed during the time between two successive

measurements. The preliminary drawings presented are only a rough sketch of such a kind of wear meter that can be designed, and more experiments are necessary to extrapolate the actual wear of a pipeline from the measurements obtained with the wear meter.

Appendix A

DIFFUSIVITY AND CONCENTRATION

A.1. Diffusity of Calcium Sulfate in Water

The diffusivity of calcium sulfate in water was calculated by means of the Nerst equation for diffusion coefficients of electrolytes at infinite dilution, given in the Chemical Engineers Handbook [24]:

$$D_o = 8.931 \times 10^{-10} T \left(\frac{l_+^\circ \quad l_-^\circ}{\Lambda^\circ}\right) \left(\frac{z_+ + z_-}{z_+ \quad z_-}\right) \qquad (A.1)$$

where D_o = diffusity of molecule (cm^2/sec)

l_-° = cationic conductance at infinite dilution (mhos/equivalent)

l_-° = anionic conductance at infinite dilution (mhos/equivalent)

$\Lambda^\circ = l_+^\circ + l_-^\circ$ = electrolyte conductance at infinite dilution (mhos/equivalent)

T = absolute temperature

z_+ = absolute valence of cation

z_- = absolute valence of anion

The ionic conductances at infinite dilution in water (Table A.1) were obtained from the Smithsonian Physical Tables [28] and used to calculate the diffusion ceofficients presented in Table A.2.

	Temperature (°C)				
ION	0	18	25	50	75
Ca^{++}	30	51	60	98	142
SO_4^{--}	41	68	79	125	177

Table A.1. Ionic conductances at infinity dilution in water (mhos/equivalent)

T (°C)	T (°F)	T(K)	D_o ($\times 10^{10} m^2/s$)	D_o ($\times 10^{3} in^2/hr$)
0	32.0	273.15	4.2262	2.3582
18	64.4	291.15	7.5779	4.2285
25	77.0	298.15	9.0803	5.0668
50	122.0	323.15	15.8539	8.8465
75	167.0	348.15	24.4984	13.6701

Table A.2. Diffusion coefficients of $CaSO_4$ at infinite dilution in H_2O

Plotting these values of temperatures and the correspondent diffusion coefficients, we sketched the curve shown in figure

A.1, which can be well represented by a second grade parabola. Since our experiments were carried out in the temperature range from 80°F to 100°F (26.7°C to 37.8°C), using three coordinate sets (T; Do) it was possible to determine the coefficients of a second grade curve for this temperature range, as follows:

$$aT^2 + bT + c = Do, \quad 18°C \leq T \leq 50°C \tag{A.2}$$

$$(18;\ 7.5779\times10^{-10}):\quad 324a + 18b + c = 7.5779\times10^{-10} \tag{A.3}$$

$$(25;\ 9.0803\times10^{-10}):\quad 625a + 25b + c = 9.0803\times10^{-10} \tag{A.4}$$

$$(50;\ 15.8539\times10^{-10}):\quad 2500a + 50b + c = 15.8539\times10^{-10} \tag{A.5}$$

In matrix form:

$$\begin{bmatrix} 324 & 18 & 1 \\ 625 & 25 & 1 \\ 2500 & 50 & 1 \end{bmatrix} \begin{Bmatrix} a \\ b \\ c \end{Bmatrix} = 10^{-10} \times \begin{Bmatrix} 7.5779 \\ 9.0803 \\ 15.8539 \end{Bmatrix} \tag{A.6}$$

Solving the system, we obtained:

$$\begin{Bmatrix} a \\ b \\ c \end{Bmatrix} = \begin{Bmatrix} 1.759857143 \times 10^{-13} \\ 1.389547143 \times 10^{-11} \\ 4.506521429 \times 10^{-10} \end{Bmatrix} \tag{A.7}$$

Therefore, equation (A.2) with the coefficients given by the vector (A.7) defines the analytical relationship between temperature, in the range from 18°C to 50°C, and the diffusion coefficient of calcium sulfate at infinite dilution in water.

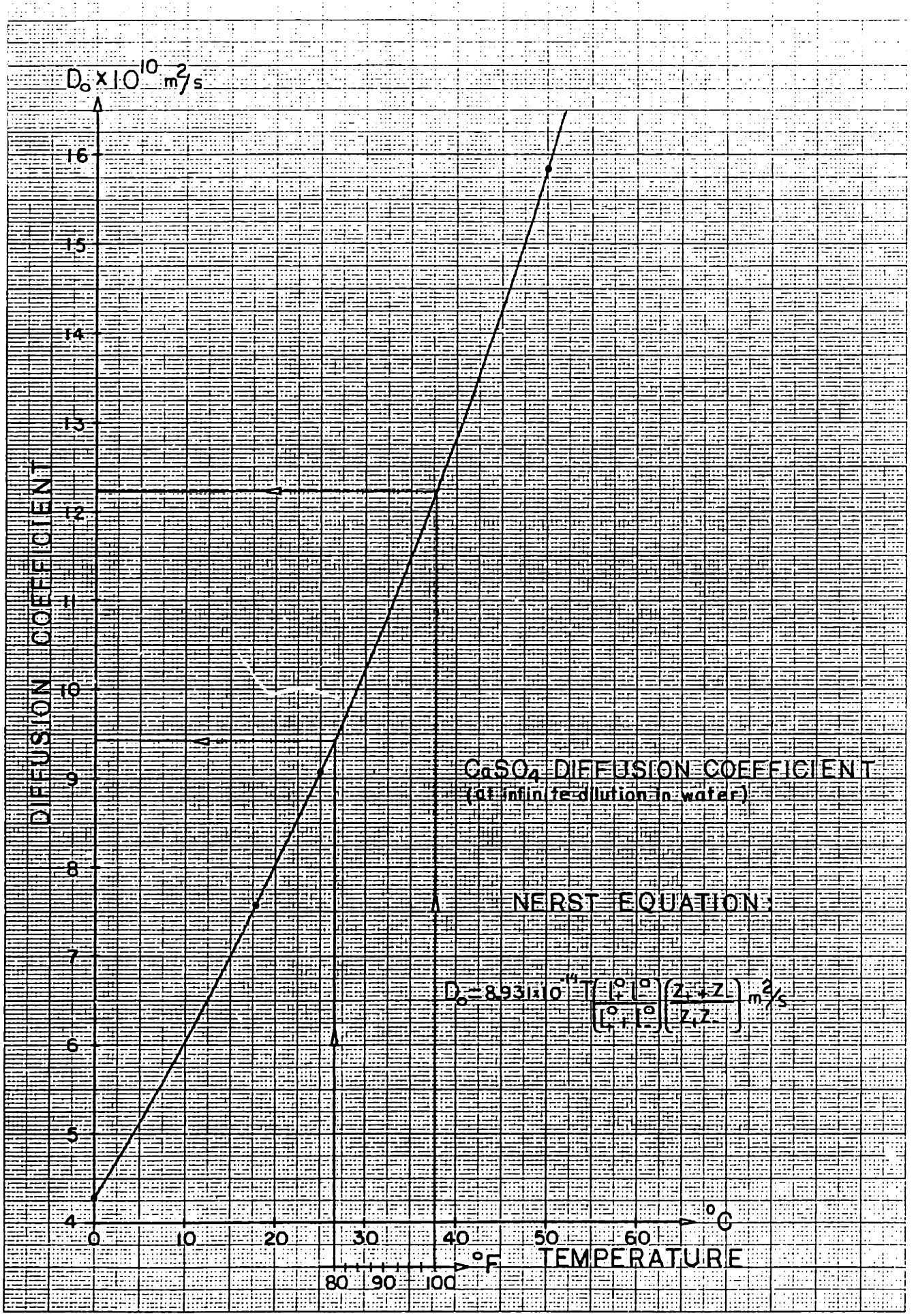

Figure A.1-Variation of the diffusion coefficient of Calcium Sulfat
(at infinite dilution in water) with temperature.

Correction of the diffusion coefficients, calculated by equation (A.1), for the effect of finite dilution was made using equation (A.8) with the data for mean ionic activity coefficients of Mg SO_4 obtained from Table 16, Appendix 8.10, of Electrolyte Solutions [25].

$$D = D_o \left[1 - \frac{\partial \ln \gamma}{\partial \ln C}\right] \qquad (A.8)$$

where: γ = mean ionic activity coefficient based on molarity

C = molarity = concentration in moles per liter

Values of the diffusion coefficents at infinite dilution and corrected for the effect of finite dilution are given in Table A.3 for the temperature range from 80°F to 100°F.

T (°F)	Do($x10^{10} m^2/s$)	Do($x10^3 in^2/hr$)	D($x10^3 in^2/hr$)
80.0	9.463	5.280	5.148
82.5	9.790	5.463	5.326
85.0	10.124	5.649	5.508
87.5	10.464	5.839	5.693
90.0	10.811	6.033	5.882
92.5	11.165	6.230	6.074
95.0	11.526	6.432	6.271
97.5	11.893	6.636	6.470
100.0	12.268	6.846	6.674

Table A.3 Diffusion Coefficients of Ca SO_4

A.2. Concentration Measurements

Based on the fact that the conductivity of a solution is directly related to the solution concentration, it was possible to plot a graph of conductivity versus concentration taking conductivity measuremetns of solutions whose concentration values were previously known.

Using a volume of 2,000 ml of water at 25°C, adding a known quantity of calcium sulfate, and measuring the conductivity, we obtained the data shown in Table A.4

m_{CaSO_4}	C (kg/m^3)	Conductivity (μmho)	
		Regular Lab. Water	Distilled Water
0.0	0.00	276	2.7
0.5	0.25	609	390
1.0	0.50	896	586
1.5	0.75	1156	797
2.0	1.00	1393	1015
2.5	1.25	1638	1247
3.0	1.50	1870	1479
3.5	1.75	2320	1668
4.0	2.00	2560	1878
4.5	2.25	2770	2040
5.0	2.50	2970	2240
5.5	2.75	3200	2420
6.0	3.00	3390	2630
6.5	3.25	3580	2780
7.0	3.50	3790	2960

Table A.4 Conductivity Measurements of Calcium Sulfate Solutions

Plotting these data, we obtained the two curves presented in Figure A.2: one curve for the measurements taken using regular laboratory water and the other using distilled water.

The value obtained for the solubility of the plaster in regular water was 2585 kg/m^3 at 25°C, which corresponds to a concentration of 2840 μmho.

A.2.1. Variation of the Concentration Difference

Collecting solution samples with the modified test section introduced in Section 3.4.2 and measuring their conductivity, we obtained the average conductivity values and corresponding concentrations shown below:

x(in)	Conductivity (μmho)	C_∞ (kg/m^3)
0	860	0.4625
4	630	0.2625
8	-	0.0

Table A.5. Conductivity and Bulk Concentrations Along the Test Section

Using the solubility as the wall concentration (C_w) and plotting the concentration difference (C_w-C_∞) versus the length (x)

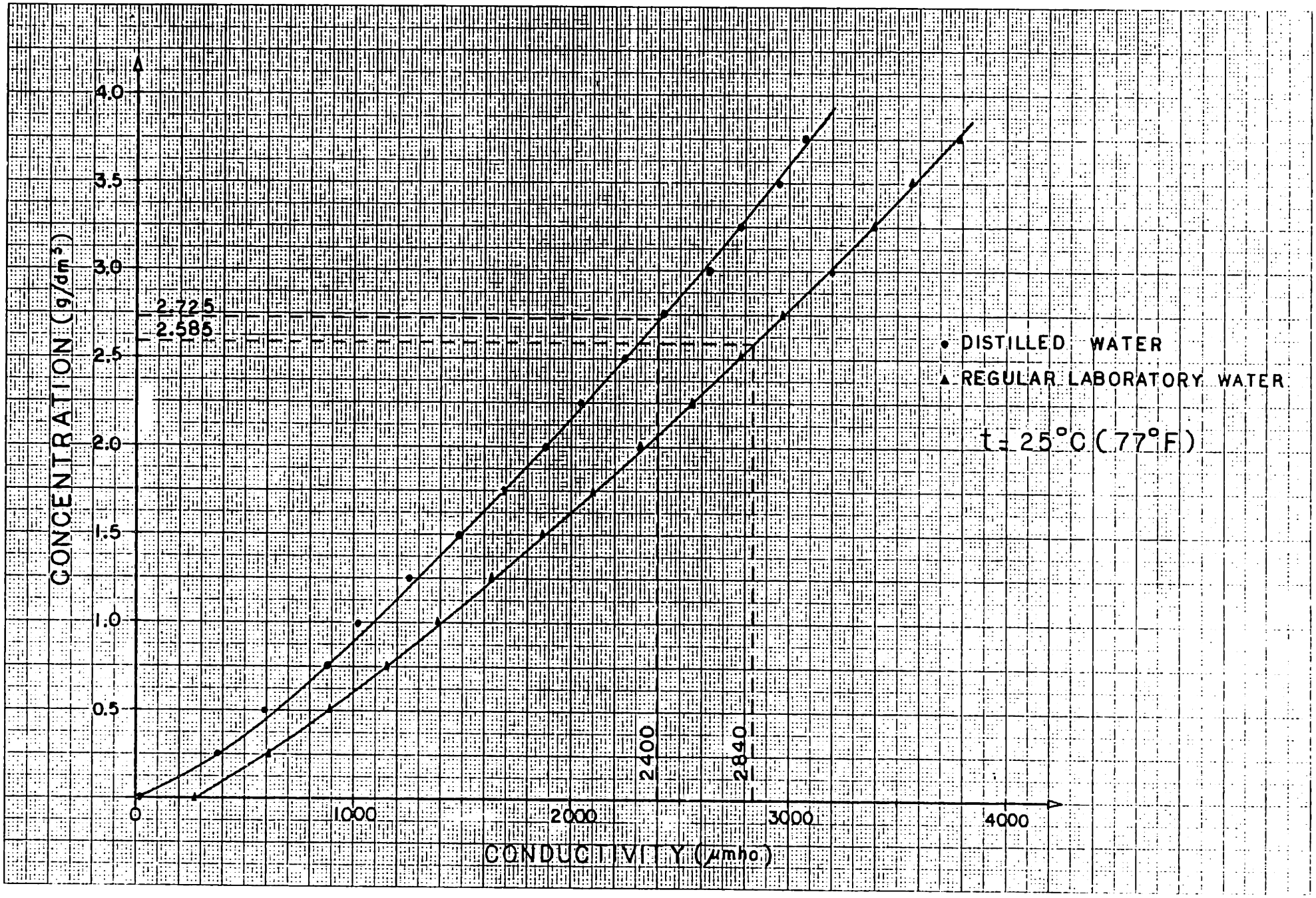

Figure A.2-Concentration of Calcium Sulfate in water versus solution conductivity.

we would see that the points obtained for x = 0, 4, and 8 inches were well alligned and it was possible to trace a straight line through these points, as drawn in Figure A.3.

The equation of this straight line can be represented by:

$$C_w - C_\infty = 2.1225 + 5.78125 \times 10^{-2} x \qquad (A.9)$$

where: x is measured in inches

$C_w - C_\infty$ is given in kg/m^3

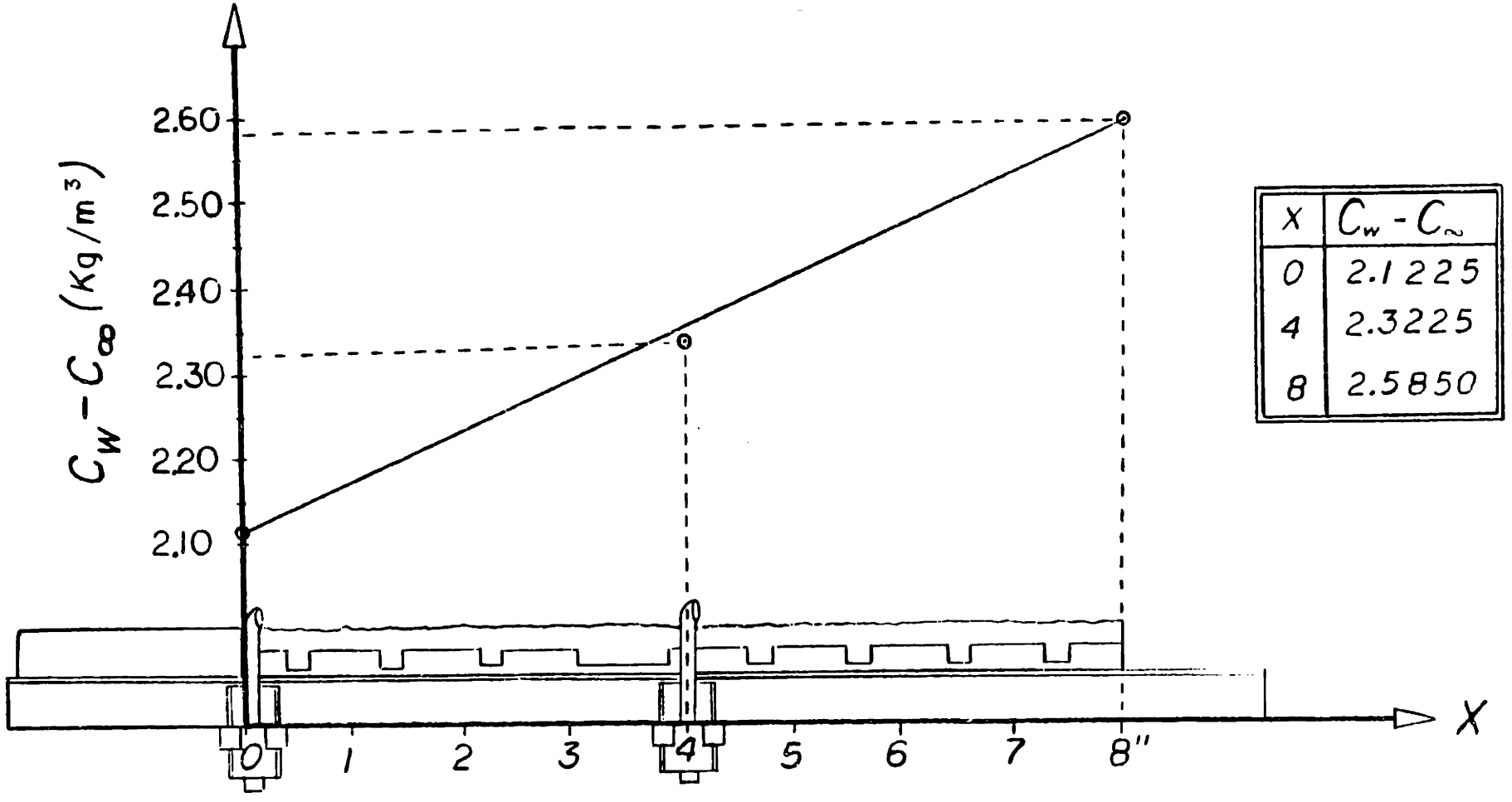

Figure A.3-Concentration difference (C_w - C_∞) versus test section length.

Appendix B

FLUID PROPERTIES

The air and water properties at low pressures used in the theoretical model were obtained from Heat Mass and Momentum Transfer [26] and are given in Tables B.1 and B.2.

B.1. Air Properties at Low Pressure

T(°F)	ρ (lbm/ft^3)	μ(lbm/hr.ft)	ν (ft^2/hr)
80.0	62.151	1.862	3.040
82.5	62.132	1.836	2.998
85.0	62.113	1.809	2.955
87.5	62.094	1.783	2.913
90.0	62.075	1.756	2.870
92.5	62.057	1.730	2.828
95.0	62.038	1.703	2.785
97.5	62.019	1.677	2.743
100.0	62.000	1.650	2.700

Table B.1. Air Properties at Low Pressure

B.2. Water Properties at Low Pressure

T(°F)	ρ(lbm/ft^3)	μ(lbm/hr. ft)	ν(ft^2/hr)
80.0	0.07361	0.04451	0.604
82.5	0.07327	0.04469	0.610
85.0	0.07293	0.04488	0.615
87.5	0.07259	0.04507	0.621
90.0	0.07225	0.04525	0.626
92.5	0.07192	0.04544	0.632
95.0	0.07158	0.04563	0.637
97.5	0.07124	0.04582	0.643
100.0	0.07090	0.04600	0.648

Table B.2. Water Properties at Low Pressure

B.3. Schmidt Number

The Schmidt numbers were calculated using data from Tables A.3. and B.2 and the results are shown in Table B.3.

$$Sc = \frac{\nu}{D} = \frac{\text{kinematic viscosity}}{\text{diffusion coefficient at finite dillution}} \qquad (2.5)$$

T(°F)	D($\times 10^3$ in^2/hr)	ν (ft^2/hr)	Sc
80.0	5.148	3.040	850
82.5	5.326	2.998	811
85.0	5.508	2.955	773
87.5	5.693	2.913	737
90.0	5.882	2.870	703
92.5	6.074	2.828	670
95.0	6.271	2.785	640
97.5	6.470	2.743	610
100.0	6.674	2.700	583

Table B.3. Schmidt Numbers in the Temperature Range from 80°F to 100°F

Appendix C

EXPERIMENTAL DATA OBTAINED

The thickness and groove geometry measurements taken before and after every time interval in which the experiments were carried out are tabulated in this Appendix. The coordinate system used and the points whose measurements were taken are defined in Figures C.1 and C.2.

The tables for each experiment are presented in the following sequence:

a) Thickness Measurements in the Straight Regions

b) Mean Thickness Differences, Dissolution Rates, and Mass Transfer Coefficients in the Straight Regions;

c) Thickness Measurements in the Groove Region;

d) Longitudinal Measurements in the Groove Region; and

e) Mean Thickness Differences, Dissolution Rates, and Mass Transfer Coefficients in the Groove Region.

To obtain the change in thickness (Δy) of a point over a period of time, for example, Δt = 240 minutes, we simply subtracted the thickness of t = 240 min from that value at t = 0. Each region or sub-region is bounded by four points; averaging the thickness difference values of these four points, we obtained the mean thickness difference of either the region or the sub-region.

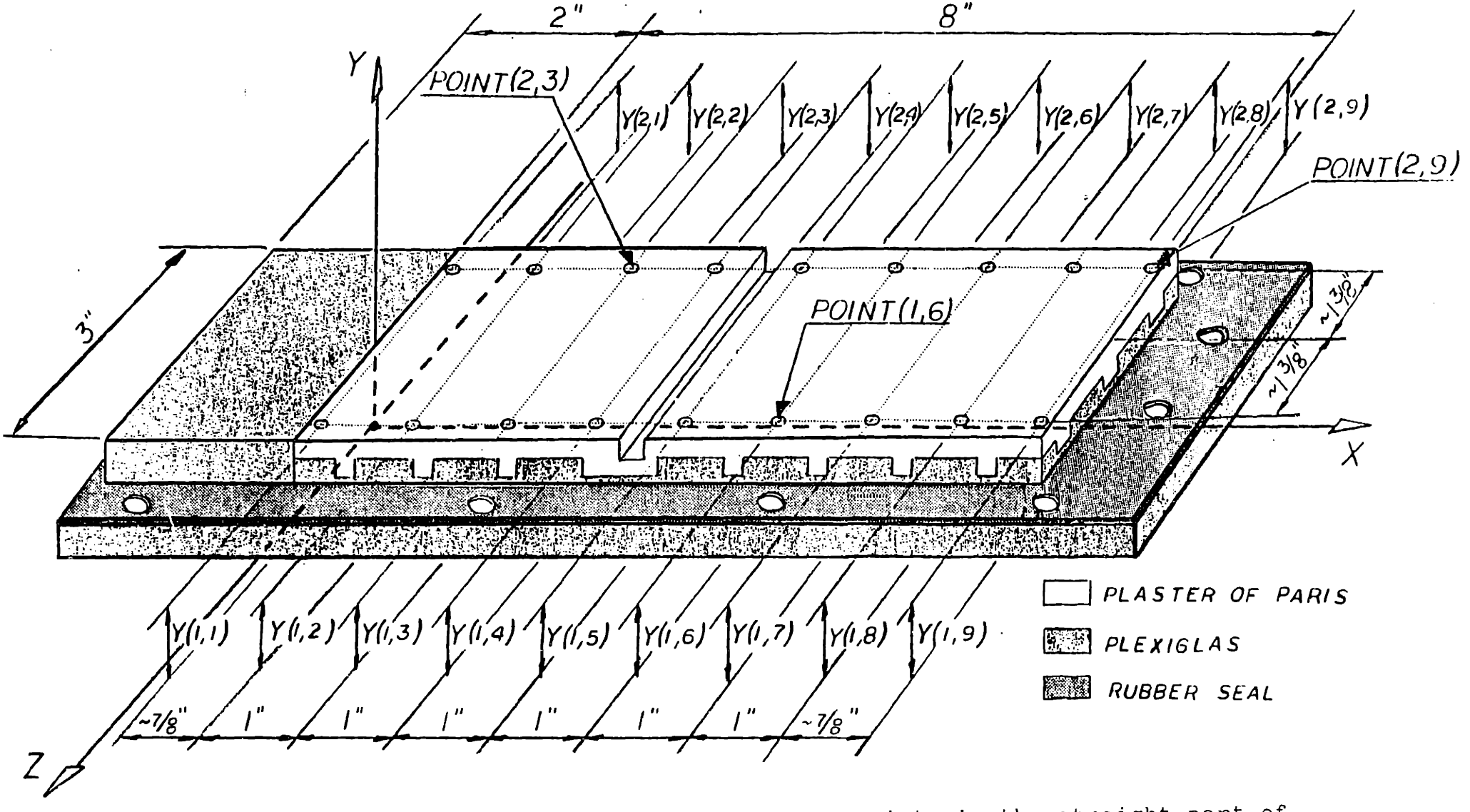

Figure C.1-Coordinate system and measurement points in the straight part of the test section.

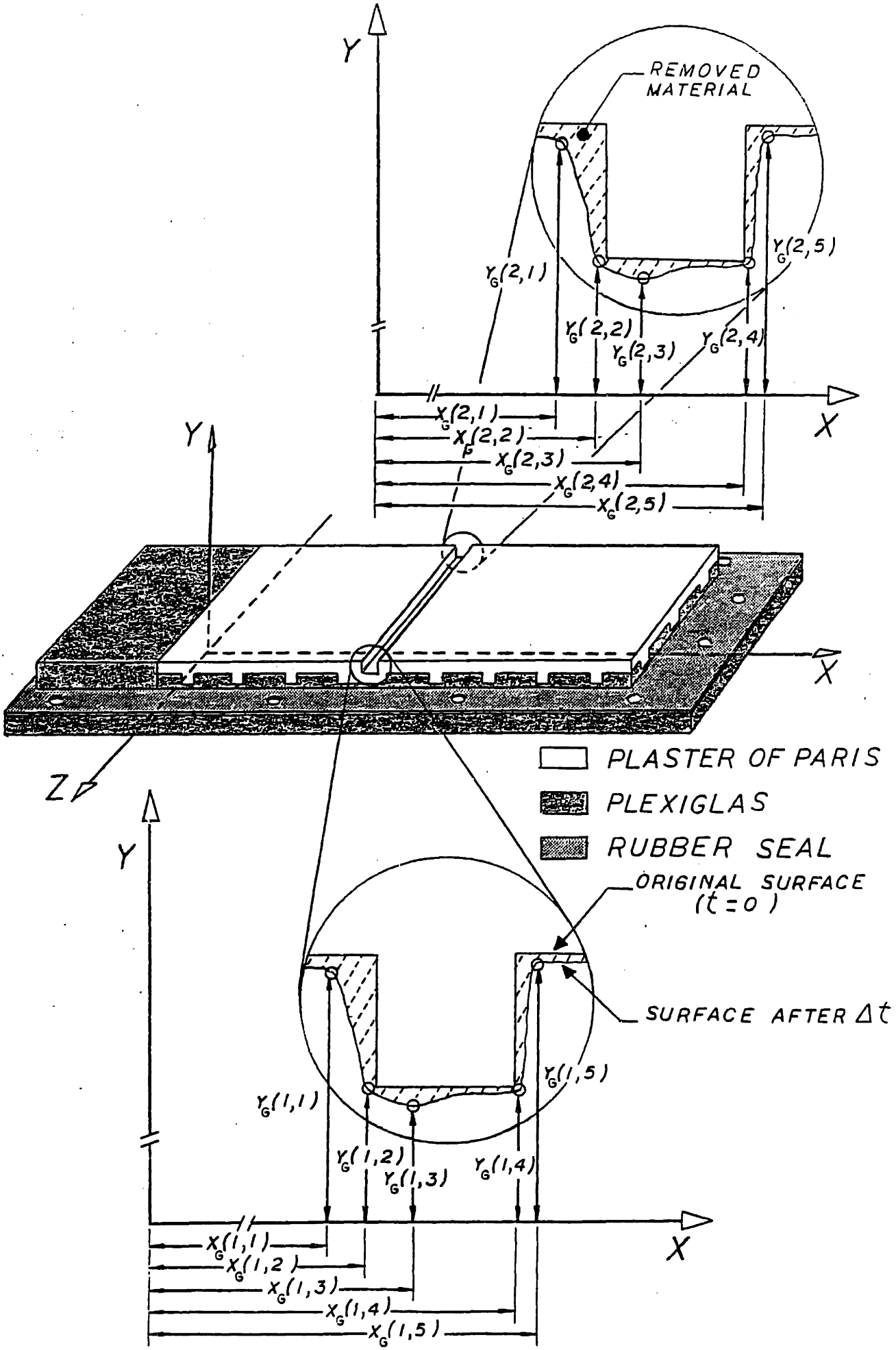

Figure C.2-Coordinate system and measurement points in the

The dissolution rates were easily obtained from the mean thickness differences using equation (C.1):

$$w = \frac{\overline{\Delta y}}{\Delta t} = \frac{\text{mean thickness difference}}{\text{time interval}} \qquad (C.1)$$

and the mass transfer coefficient using equation (C.2.b):

$$J = w\rho = h_d(C_w - C_\infty) \qquad (C.2.a)$$

$$h_d = \frac{w\rho}{C_w - C_\infty} \qquad (C.2.b)$$

where the density can be measured, the dissolution rate is given by equation (C.1), and the concentration difference by equation (A.9).

C.1. Data Tables

Experiment 1.1 - V_{air} = 100 ft/s

Q_{H_2O} = 490 ml/min

	t (minutes)					
	0		120		240	
j \ i	1	2	1	2	1	2
1	.8642	.8569	.8336	.8474	.8092	.8354
2	.8606	.8568	.8313	.8467	.7993	.8325
3	.8636	.8568	.8326	.8480	.7932	.8306
4	.8626	.8593	.8294	.8477	.7875	.8297
5	.8694	.8588	.8297	.8425	.7923	.8304
6	.8689	.8586	.8271	.8378	.7897	.8200
7	.8532	.8554	.8232	.8355	.7860	.8179
8	.8472	.8537	.8168	.8331	.7797	.8118
9	.8464	.8489	.8095	.8260	.7695	.7889

TABLE C. 1.a- Thickness Measurements (Y(i,j)inches) in the Straight Regions.

Δt(min)	120			240		
Region	$\overline{\Delta Y}x10^2$	$Wx10^6$	$h_d x10^5$	$\overline{\Delta Y}x10^2$	$Wx10^6$	$h_d x10^5$
A	1.99	2.76	3.98	4.06	2.82	4.06
B	1.98	2.75	3.90	4.56	3.16	4.48
C	2.12	2.94	4.07	5.04	3.50	4.85
D	2.97	4.12	5.43	5.59	3.88	5.12
E	2.81	3.91	5.03	5.57	3.86	4.96
F	2.52	3.50	4.39	5.36	3.72	4.66
G	2.77	3.85	4.70	6.16	4.28	5.22

TABLE C. 1.b- Mean Thickness Differences (in), Dissolution Rates (in/s), and Mass Transfer Coefficients (m/s) in the Straight Regions.

Experiment 1.1

	t (minutes)					
	0		120		240	
j \ i	1	2	1	2	1	2
1	.8628	.8593	.8277	.8406	.7845	.8175
2	.7500	.7470	.7370	.7410	.7180	.7250
3	—	—	.7270	.7300	.6920	.7100
4	.7500	.7470	.7370	.7410	.7180	.7250
5	.8624	.8594	.8310	.8467	.7923	.8304

TABLE C. 1.c- Thickness measurements ($Y_G(i,j)$ inches) in the Groove Region.

	t (minutes)					
	0		120		240	
j \ i	1	2	1	2	1	2
1	3.490	3.522	3.431	3.478	3.390	3.443
2	3.492	3.527	3.476	3.515	3.462	3.481
3	—	—	3.528	3.555	3.510	3.535
4	3.732	3.762	3.751	3.775	3.757	3.776
5	3.740	3.773	3.764	3.790	3.787	3.798

TABLE C. 1.d- Longitudinal measurements ($X_G(i,j)$ inches) in the Groove Region.

Δt (min)	120			240		
Sub-region	$\overline{\Delta Y} \times 10^2$	$W \times 10^6$	$h_d \times 10^5$	$\overline{\Delta Y} \times 10^2$	$W \times 10^6$	$h_d \times 10^5$
I	2.46	3.42	4.67	5.24	3.64	4.97
II	8.71	12.10	16.49	8.84	6.14	8.37
III	1.65	2.29	3.12	4.06	2.82	3.84
IV	0.95	1.32	1.79	2.71	1.88	2.55
V	10.86	15.08	20.44	8.81	6.12	8.29
VI	2.51	3.48	4.71	5.13	3.56	4.82

TABLE C. 1.e- Mean Thickness Differences (in), Dissolution Rates (in/s), and Mass Transfer Coefficients (m/s), in the Groove Region.

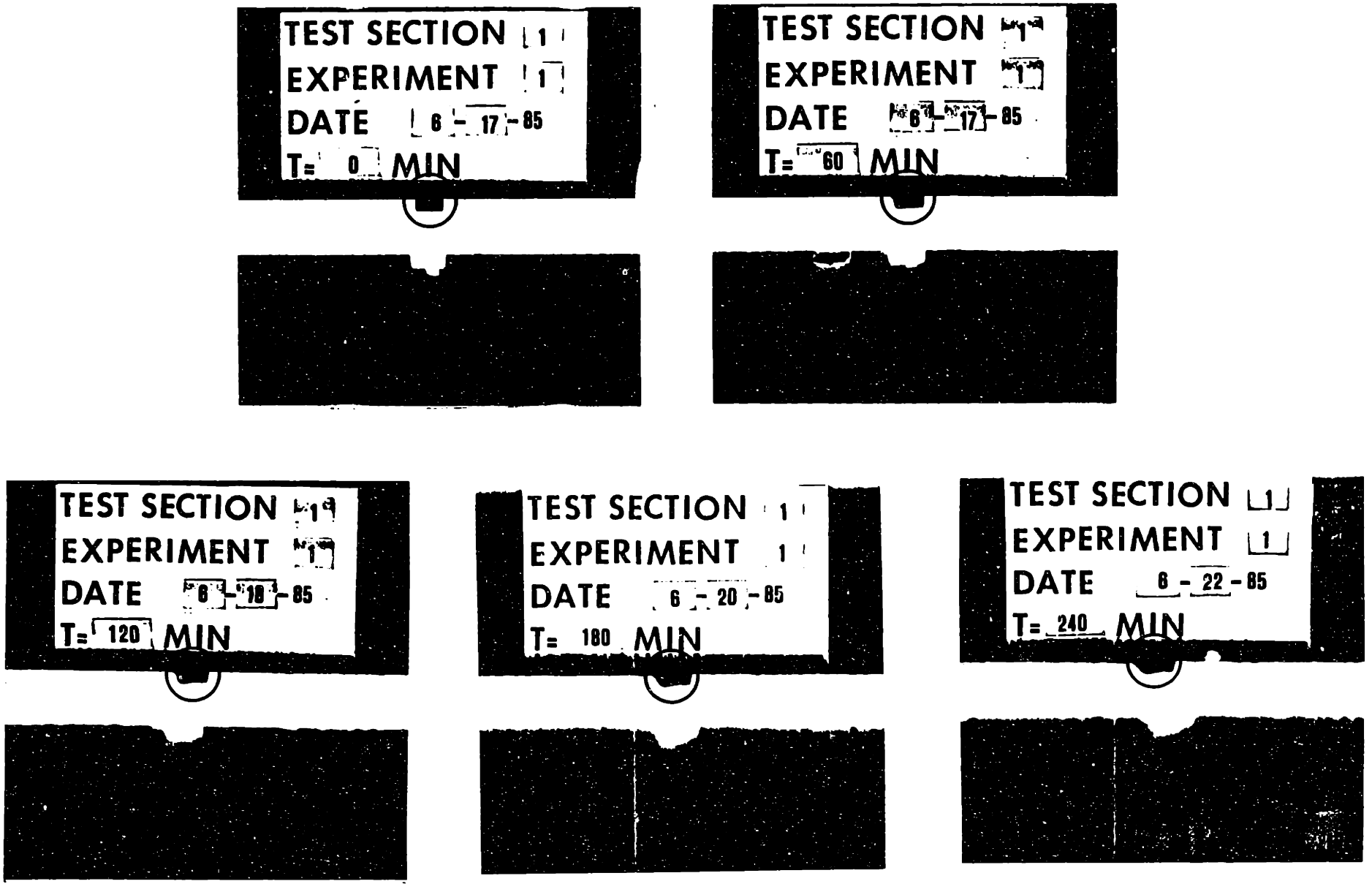

Figure C.3- Experiment 1.1 – Variation of the groove shape with time.

Experiment 2.1 - V_{air} = 100 ft/s

Q_{H_2O} = 600 ml/min

	t (minutes)					
	0		120		240	
j \ i	1	2	1	2	1	2
1	.8673	.8522	.8370	.8401	.8007	.8251
2	.8736	.8555	.8403	.8399	.8005	.8211
3	.8808	.8609	.8478	.8457	.8046	.8239
4	.8828	.8644	.8446	.8501	.8033	.8319
5	.8834	.8642	.8515	.8476	.8080	.8314
6	.8823	.8694	.8495	.8489	.8070	.8334
7	.8830	.8721	.8504	.8499	.8081	.8331
8	.8819	.8750	.8496	.8515	.8068	.8357
9	.8835	.8785	.8487	.8503	.8109	.8176

TABLE C.2.a- Thickness Measurements (Y(i,j)inches) in the Straight Regions.

Δt(min)	120			240		
Region	$\overline{\Delta Y}x10^2$	$Wx10^6$	$h_d x10^5$	$\overline{\Delta Y}x10^2$	$Wx10^6$	$h_d x10^5$
A	2.28	3.17	4.57	5.01	3.48	5.02
B	2.43	3.37	4.78	5.49	3.81	5.40
C	2.52	3.50	4.85	5.63	3.91	5.41
D	2.55	3.54	4.67	5.49	3.81	5.03
E	2.70	3.75	4.82	5.63	3.91	5.03
F	2.76	3.84	4.81	5.70	3.96	4.96
G	2.97	4.13	5.04	6.19	4.30	5.25

TABLE C. 2.b- Mean Thickness Differences (in), Dissolution Rates (in/s), and Mass Transfer Coefficients (m/s) in the Straight Regions.

Experiment 2.1

	t (minutes)					
	0		120		240	
j \ i	1	2	1	2	1	2
1	.8831	.8653	.8442	.8453	.8030	.8244
2	.7500	.7540	.7430	.7400	.7200	.7240
3	—	—	.7160	.7250	.6830	.6920
4	.7500	.7540	.7430	.7400	.7200	.7240
5	.8846	.8641	.8517	.8481	.8082	.8316

TABLE C.2.c- Thickness measurements ($Y_G(i,j)$ inches) in the Groove Region.

	t (minutes)					
	0		120		240	
j \ i	1	2	1	2	1	2
1	3.510	3.538	3.455	3.494	3.390	3.452
2	3.513	3.782	3.488	3.520	3.444	3.493
3	—	—	3.555	3.570	3.515	3.564
4	3.739	3.541	3.755	3.785	3.754	3.790
5	3.750	3.780	3.770	3.799	3.785	3.813

TABLE C.2.d- Longitudinal measurements ($X_G(i,j)$ inches) in the Groove Region.

Δt (min)	120			240		
Sub-region	$\overline{\Delta Y}x10^2$	$Wx10^6$	$h_d x10^5$	$\overline{\Delta Y}x10^2$	$Wx10^6$	$h_d x10^5$
I	2.79	3.87	5.28	5.79	4.02	5.49
II	9.72	13.50	18.39	11.91	8.27	11.27
III	2.45	3.40	4.63	5.30	3.68	5.01
IV	1.05	1.46	1.98	3.00	2.08	2.82
V	9.87	13.71	18.58	10.18	7.07	9.58
VI	2.43	3.38	4.57	5.43	3.77	5.10

TABLE C.2.e- Mean Thickness Differences (in), Dissolution Rates (in/s), and Mass Transfer Coefficients (m/s), in the Groove Region.

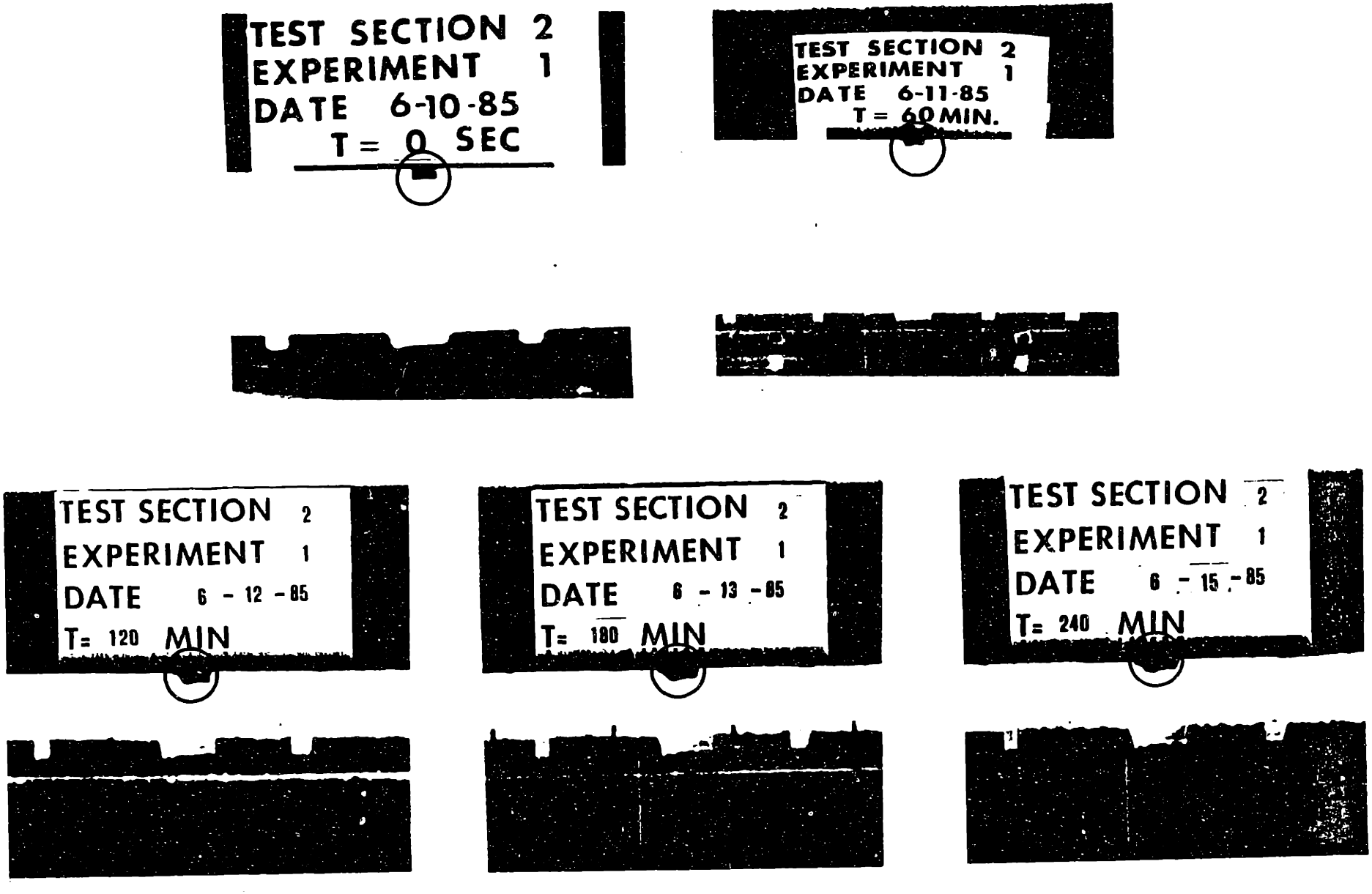

Figure C.4- Experiment 2.1 – Variation of the groove shape with time.

Experiment 3.1 - V_{air} = 100 ft/s

Q_{H_2O} = 700 ml/min

	t (minutes)					
	0		120		240	
j \ i	1	2	1	2	1	2
1	.9911	1.0141	.9644	.9918	.9299	.9766
2	.9947	1.0046	.9602	.9870	.9263	.9739
3	1.0091	1.0150	.9721	1.0017	.9359	.9860
4	1.0127	1.0168	.9744	1.0017	.9317	.9860
5	1.0142	1.0189	.9762	.9976	.9357	.9797
6	1.0149	1.0198	.9809	.9968	.9414	.9795
7	1.0184	1.0246	.9823	.9992	.9395	.9810
8	1.0240	1.0277	.9870	1.0033	.9453	.9842
9	1.0237	1.0250	.9785	.9998	.9462	.9720

TABLE C.3.a- Thickness Measurements (Y(i,j)inches) in the Straight Regions.

Δt(min)	120			240		
Region	$\overline{\Delta Y}x10^2$	$Wx10^6$	$h_d x10^5$	$\overline{\Delta Y}x10^2$	$Wx10^6$	$h_d x10^5$
A	3.03	4.21	5.06	6.21	4.31	4.94
B	3.25	4.52	5.06	6.88	4.78	4.96
C	3.54	4.92	4.98	7.43	5.16	5.15
D	3.72	5.16	5.33	7.65	5.31	5.30
E	3.69	5.13	5.30	7.56	5.25	5.27
F	3.63	5.04	5.35	7.30	5.07	5.33
G	3.77	5.23	5.59	7.55	5.24	5.36

TABLE C.3.b- Mean Thickness Differences (in), Dissolution Rates (in/s), and Mass Transfer Coefficients (m/s) in the Straight Regions.

Experiment 3.1

	t (minutes)					
	0		120		240	
j \ i	1	2	1	2	1	2
1	1.0125	1.0171	.9738	.9953	.9332	.9765
2	.8980	.8980	.8780	.8860	.8590	.8750
3	—	—	.8590	.8790	.8150	.8510
4	.8980	.8980	.8780	.8860	.8590	.8750
5	1.0117	1.0184	.9792	.9968	.9345	.9800

TABLE C. 3.c- Thickness measurements ($Y_G(i,j)$ inches) in the Groove Region.

	t (minutes)					
	0		120		240	
j \ i	1	2	1	2	1	2
1	3.433	3.479	3.382	3.441	3.334	3.407
2	3.432	3.489	3.416	3.489	3.375	3.440
3	—	—	3.456	3.545	3.447	3.521
4	3.688	3.721	3.704	3.742	3.706	3.746
5	3.690	3.734	3.715	3.754	3.720	3.763

TABLE C. 3.d- Longitudinal measurements ($X_G(i,j)$ inches) in the Groove Region.

Δt (min)	120			240		
Sub-region	$\overline{\Delta Y} \times 10^2$	$W \times 10^6$	$h_d \times 10^5$	$\overline{\Delta Y} \times 10^2$	$W \times 10^6$	$h_d \times 10^5$
I	2.85	3.96	5.41	5.79	4.02	5.49
II	7.84	10.89	14.84	11.98	8.32	11.34
III	2.47	3.43	4.67	5.37	3.73	5.07
IV	1.60	2.22	3.01	3.10	2.15	2.92
V	12.11	16.82	22.80	12.79	8.88	12.04
VI	2.84	3.94	5.33	5.83	4.05	5.48

TABLE C. 3.e- Mean Thickness Differences (in), Dissolution Rates (in/s), and Mass Transfer Coefficients (m/s), in the Groove Region.

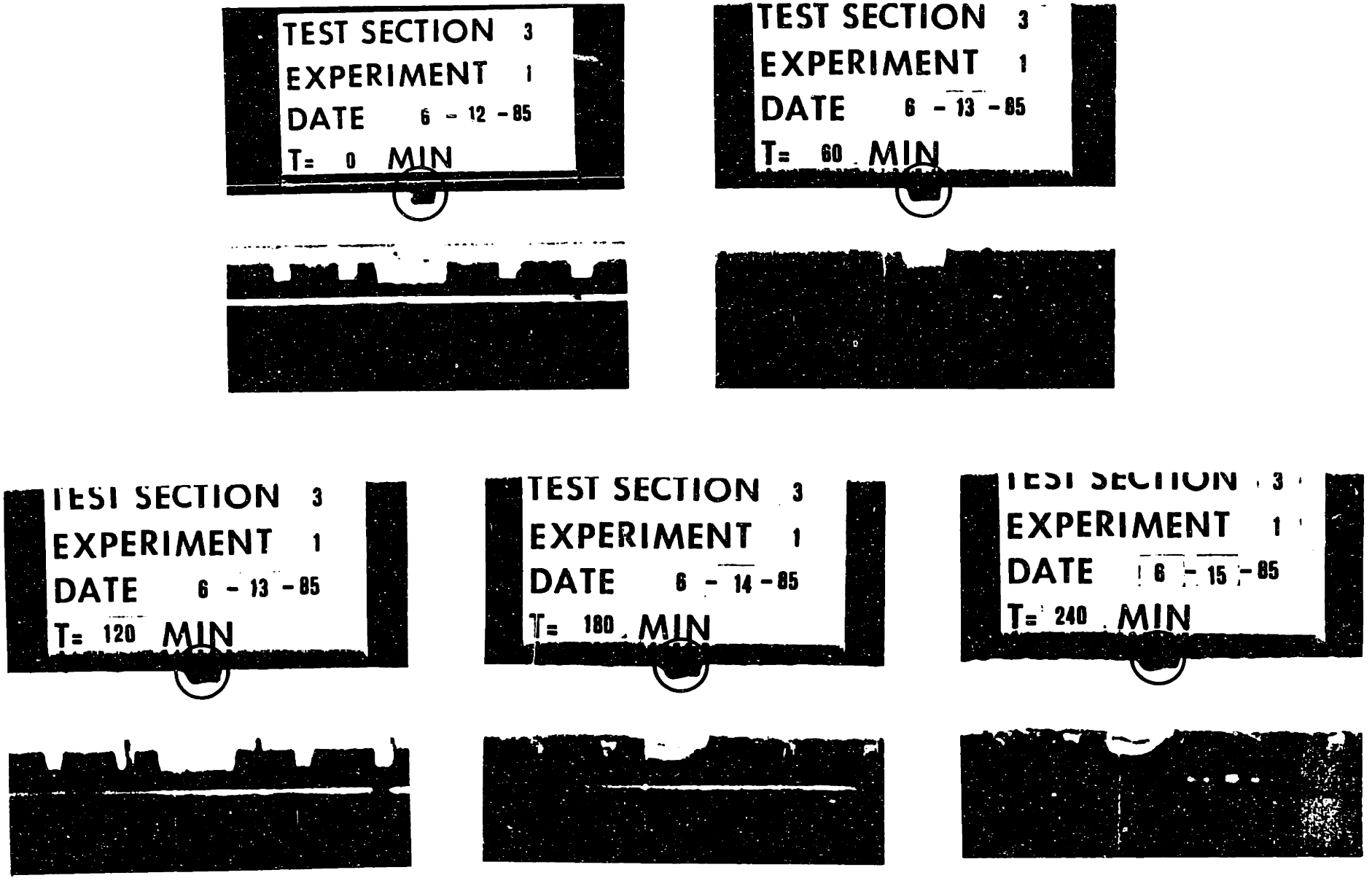

Figure C.5- Experiment 3.1 – Variation of the groove shape with time.

Experiment 4.1 - V_{air} = 100 ft/s

Q_{H_2O} = 810 ml/min

	t (minutes)					
	0		120		240	
j \ i	1	2	1	2	1	2
1	.8713	.8730	.8407	.8485	.8094	.8293
2	.8693	.8925	.8383	.8534	.8001	.8311
3	.8781	.8811	.8406	.8625	.7990	.8422
4	.8834	.8878	.8428	.8659	.7983	.8413
5	.8851	.8838	.8505	.8644	.8076	.8419
6	.8909	.8908	.8542	.8647	.8144	.8384
7	.8928	.8946	.8549	.8670	.8148	.8411
8	.8938	.8950	.8585	.8664	.8207	.8392
9	.8892	.8892	.8530	.8556	.8092	.8250

TABLE C.4.a- Thickness Measurements (Y(i,j)inches) in the Straight Regions.

Δt(min)	120			240		
Region	$\overline{\Delta Y}x10^2$	$Wx10^6$	$h_d x10^5$	$\overline{\Delta Y}x10^2$	$Wx10^6$	$h_d x10^5$
A	3.13	4.35	6.27	5.99	4.16	6.00
B	3.16	4.39	6.22	6.22	4.32	6.12
C	2.97	4.12	5.70	6.24	4.33	6.00
D	2.92	4.06	5.36	6.21	4.31	5.68
E	3.21	4.46	5.74	6.51	4.52	5.81
F	3.23	4.49	5.63	6.51	4.52	5.67
G	3.34	4.64	5.66	6.83	4.74	5.79

TABLE C.4.b- Mean Thickness Differences (in), Dissolution Rates (in/s), and Mass Transfer Coefficients (m/s) in the Straight Regions.

Experiment 4.1

	t (minutes)					
	0		120		240	
j \ i	1	2	1	2	1	2
1	.8882	.8887	.8846	.8645	.8035	.8357
2	.7520	.7590	.7310	.7520	.7190	.7390
3	—	—	.7170	.7380	.6870	.7120
4	.7430	.7620	.7310	.7520	.7190	.7390
5	.8860	.8873	.8497	.8651	.8085	.8420

TABLE C. 4.c- Thickness measurements ($Y_G(i,j)$ inches) in the Groove Region.

	t (minutes)					
	0		120		240	
j \ i	1	2	1	2	1	2
1	3.501	3.541	3.444	3.494	3.402	3.459
2	3.502	3.545	3.493	3.531	3.445	3.493
3	—	—	3.538	3.594	3.517	3.552
4	3.773	3.781	3.757	3.792	3.756	3.792
5	3.751	3.793	3.774	3.808	3.790	3.821

TABLE C. 4.d- Longitudinal measurements ($X_G(i,j)$ inches) in the Groove Region.

Δt (min)	120			240		
Sub-region	$\overline{\Delta Y} \times 10^2$	$W \times 10^6$	$h_d \times 10^5$	$\overline{\Delta Y} \times 10^2$	$W \times 10^6$	$h_d \times 10^5$
I	3.26	4.53	6.19	6.74	4.68	6.39
II	8.92	12.39	16.88	12.70	8.82	12.02
III	2.18	3.03	4.12	4.46	3.10	4.22
IV	1.25	1.74	2.36	2.51	1.74	2.36
V	10.79	19.48	26.40	11.95	8.30	11.25
VI	2.46	3.41	4.61	6.06	4.21	5.70

TABLE C. 4.e- Mean Thickness Differences (in), Dissolution Rates (in/s), and Mass Transfer Coefficients (m/s), in the Groove Region.

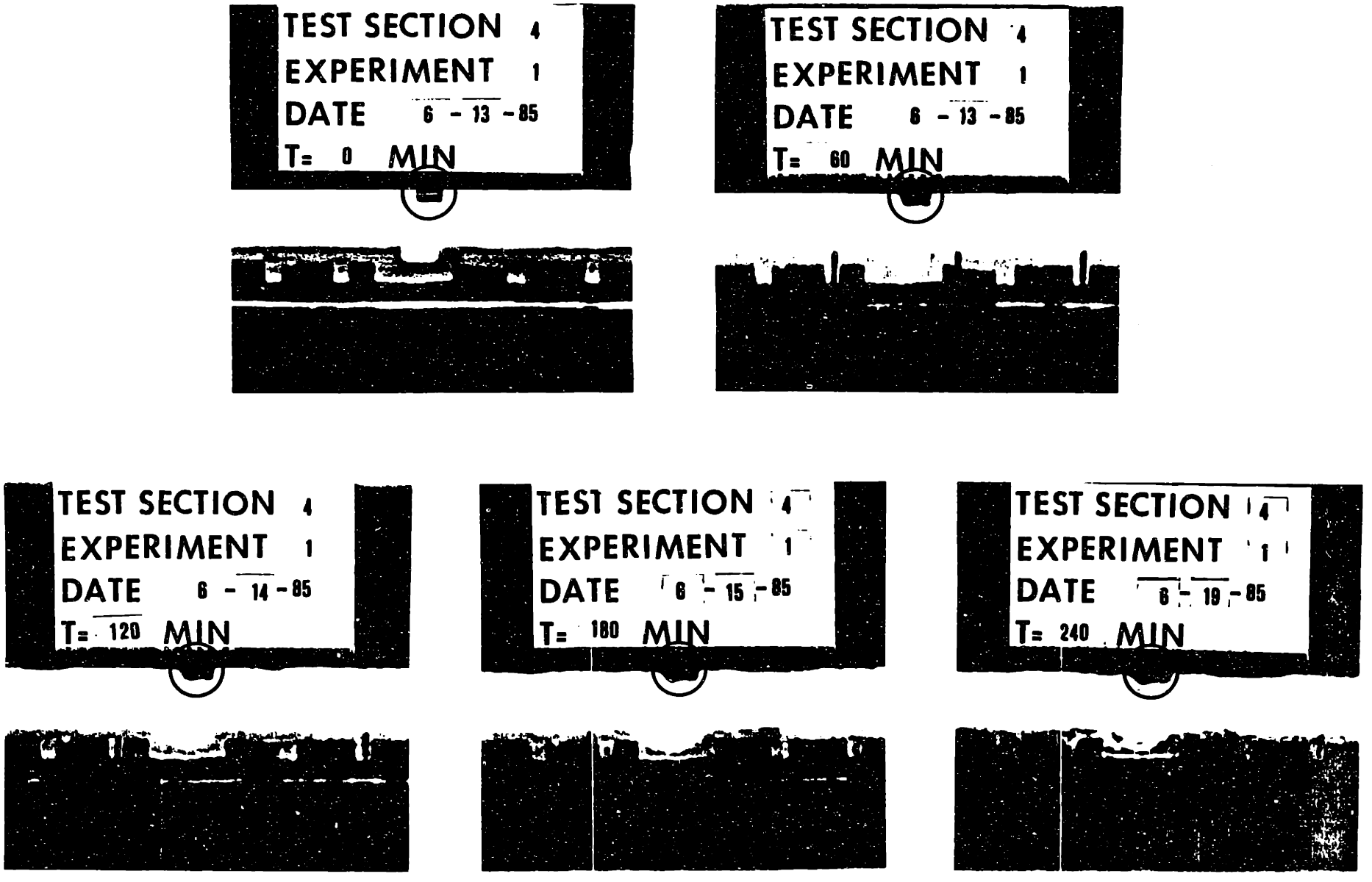

Figure C.6- Experiment 4.1 – Variation of the groove shape with time.

Experiment 7.2 - V_{air} = 100 ft/s

Q_{H_2O} = 940 ml/min

	t (minutes)					
	0		120		240	
j \ i	1	2	1	2	1	2
1	.8337	.8406	.7943	.8126	.7569	.7905
2	.8318	.8446	.7879	.8174	.7458	.7931
3	.8327	.8486	.7889	.8191	.7457	.7978
4	.8336	.8500	.7810	.8246	.7368	.8006
5	.8372	.8503	.7943	.8169	.7491	.7883
6	.8381	.8484	.7966	.8118	.7542	.7805
7	.8403	.8479	.7999	.8099	.7608	.7789
8	.8434	.8480	.8025	.8100	.7671	.7830
9	.8514	.8533	.8040	.8133	.7632	.7771

TABLE C.5.a- Thickness Measurements (Y(i,j) inches) in the Straight Regions.

Δt(min)	120			240		
Region	$\overline{\Delta Y} \times 10^2$	$W \times 10^6$	$h_d \times 10^5$	$\overline{\Delta Y} \times 10^2$	$W \times 10^6$	$h_d \times 10^5$
A	3.46	4.81	6.93	6.61	4.59	6.62
B	3.61	5.01	7.10	6.88	4.78	6.78
C	3.78	5.25	7.27	7.10	4.93	6.83
D	3.86	5.36	7.07	7.55	5.24	6.91
E	3.91	5.43	6.98	7.50	5.21	6.70
F	3.93	5.46	6.84	7.24	5.03	6.30
G	4.15	5.77	7.04	7.65	5.31	6.48

TABLE C.5.b- Mean Thickness Differences (in), Dissolution Rates (in/s), and Mass Transfer Coefficients (m/s) in the Straight Regions.

Experiment 7.2

	t (minutes)					
	0		120		240	
j \ i	1	2	1	2	1	2
1	.8364	.8507	.7872	.8226	.7403	.7979
2	.7120	.7400	.6850	.7420	.6690	.6980
3	—	—	.6680	.7040	.6270	.6710
4	.7060	.7450	.6850	.7240	.6690	.6980
5	.8372	.8503	.7955	.8166	.7491	.7883

TABLE C. 5.c- Thickness measurements ($Y_G(i,j)$ inches) in the Groove Region.

	t (minutes)					
	0		120		240	
j \ i	1	2	1	2	1	2
1	3.498	3.530	3.432	3.477	3.374	3.420
2	3.502	3.541	3.472	3.511	3.420	3.463
3	—	—	3.539	3.588	3.558	3.574
4	3.774	3.806	3.783	3.818	3.789	3.822
5	3.779	3.821	3.814	3.848	3.828	3.849

TABLE C. 5.d- Longitudinal measurements ($X_G(i,j)$ inches) in the Groove Region.

Δt (min)	120			240		
Sub-region	$\overline{\Delta Y} \times 10^2$	$W \times 10^6$	$h_d \times 10^5$	$\overline{\Delta Y} \times 10^2$	$W \times 10^6$	$h_d \times 10^5$
I	3.88	5.39	7.36	7.37	5.12	6.99
II	10.47	14.54	19.81	13.48	9.36	12.75
III	3.36	4.66	6.34	6.52	4.53	6.16
IV	2.12	2.95	4.00	4.22	2.93	3.98
V	9.32	12.94	17.54	11.82	8.21	11.13
VI	3.79	5.27	7.13	7.50	5.21	7.05

TABLE C.5 .e- Mean Thickness Differences (in), Dissolution Rates (in/s), and Mass Transfer Coefficients (m/s), in the Groove Region.

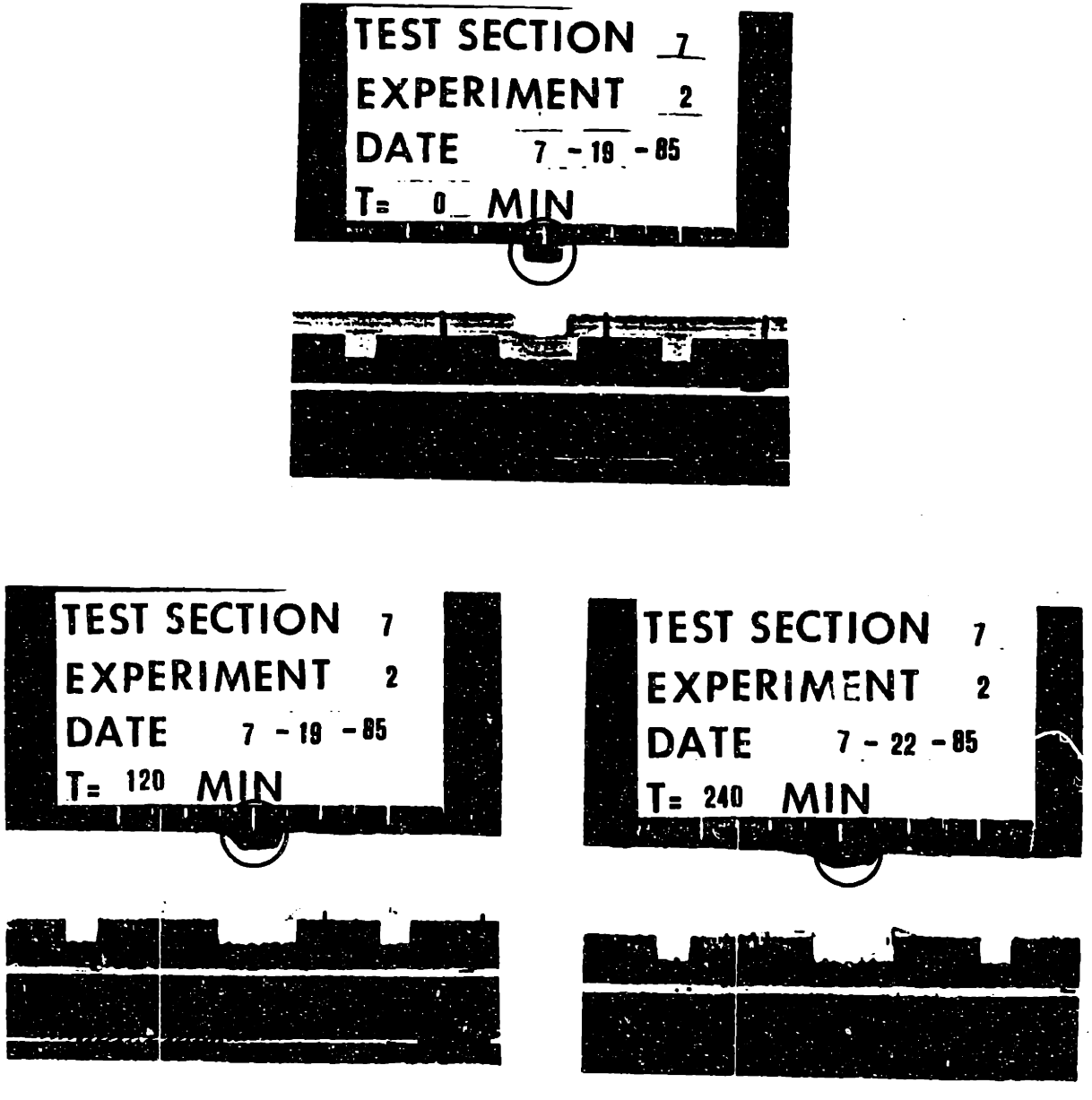

Figure C.7- Experiment 7.2 – Variation of the groove shape with time.

Experiment 5.1 - V_{air} = 125 ft/s

Q_{H_2O} = 490 ml/min

	t (minutes)					
	0		120		240	
j \ i	1	2	1	2	1	2
1	.8444	.8718	.8170	.8401	.7856	.8294
2	.8485	.8703	.8156	.8497	.7789	.8371
3	.8597	.8704	.8214	.8590	.7809	.8459
4	.8598	.8685	.8177	.8536	.7730	.8439
5	.8554	.8617	.8199	.8448	.7749	.8337
6	.8507	.8554	.8133	.8370	.7669	.8248
7	.8460	.8504	.8075	.8309	.7659	.8167
8	.8445	.8486	.8100	.8254	.7722	.8089
9	.8449	.8446	.8086	.8199	.7716	.7890

TABLE C.6.a- Thickness Measurements (Y(i,j) inches) in the Straight Regions.

Δt(min)	120			240		
Region	$\overline{\Delta Y}x10^2$	$Wx10^6$	$h_d x10^5$	$\overline{\Delta Y}x10^2$	$Wx10^6$	$h_d x10^5$
A	2.82	3.91	5.64	5.10	3.54	5.10
B	2.58	3.58	5.07	5.16	3.58	5.07
C	2.67	3.71	5.14	5.44	3.78	5.23
D	2.71	3.76	4.96	5.57	3.87	5.10
E	2.84	3.95	5.08	5.70	3.96	5.09
F	2.89	4.02	5.04	5.64	3.92	4.91
G	2.97	4.12	5.03	6.02	4.18	5.10

TABLE C.6.b- Mean Thickness Differences (in), Dissolution Rates (in/s), and Mass Transfer Coefficients (m/s) in the Straight Regions.

Experiment 5.1

	t (minutes)					
	0		120		240	
j \ i	1	2	1	2	1	2
1	.8595	.8677	.8157	.8469	.7721	.8330
2	.7290	.7340	.7110	.7140	.6960	.7020
3	—	—	.7000	.7100	.6680	.6800
4	.7250	.7260	.7110	.7140	.6960	.7020
5	.8545	.8635	.8209	.8463	.7766	.8335

TABLE C.6.c- Thickness measurements ($Y_G(i,j)$ inches) in the Groove Region.

	t (minutes)					
	0		120		240	
j \ i	1	2	1	2	1	2
1	3.491	3.514	3.434	3.463	3.401	3.412
2	3.491	3.516	3.479	3.497	3.441	3.444
3	—	—	3.517	3.538	3.510	3.520
4	3.736	3.765	3.740	3.774	3.758	3.779
5	3.750	3.767	3.771	3.786	3.794	3.794

TABLE C.6.d- Longitudinal measurements ($X_G(i,j)$ inches) in the Groove Region.

Δt (min)	120			240		
Sub-region	$\overline{\Delta Y}x10^2$	$Wx10^6$	$h_d x10^5$	$\overline{\Delta Y}x10^2$	$Wx10^6$	$h_d x10^5$
I	3.04	4.22	5.76	5.83	4.05	5.53
II	9.58	13.30	18.12	13.28	9.22	12.56
III	2.10	2.92	3.97	4.62	3.21	4.37
IV	1.60	2.22	3.01	2.95	2.05	2.78
V	9.86	13.69	18.56	12.23	8.49	11.51
VI	2.58	3.58	4.84	5.41	3.76	5.09

TABLE C.6.e- Mean Thickness Differences (in), Dissolution Rates (in/s), and Mass Transfer Coefficients (m/s), in the Groove Region.

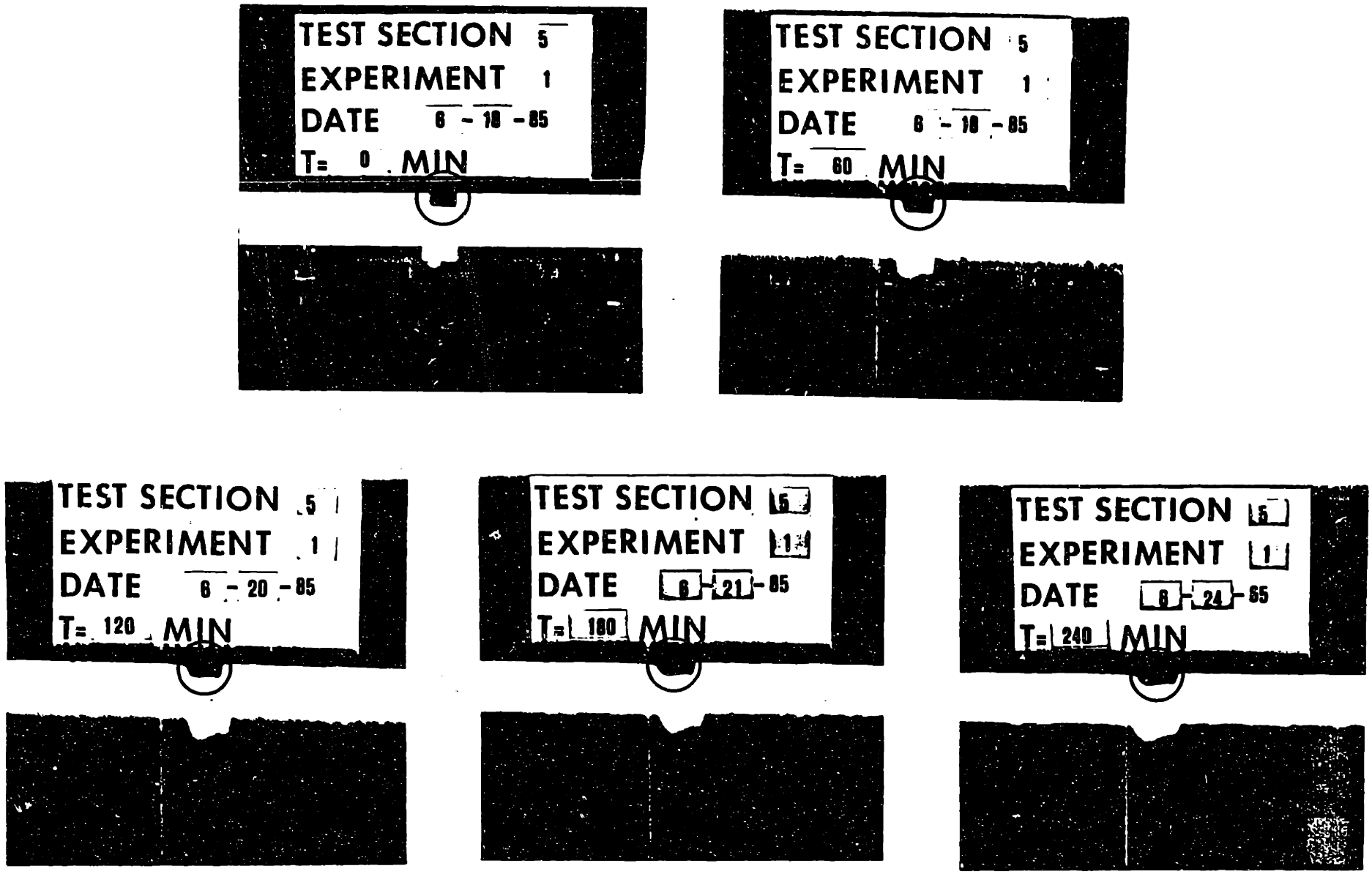

Figure C.8- Experiment 5.1 — Variation of the groove shape with time.

Experiment 6.1- V_{air} = 125 ft/s

Q_{H_2O} = 600 ml/min

	t (minutes)					
	0		120		240	
j \ i	1	2	1	2	1	2
1	.8578	.8535	.8184	.8358	.7808	.8151
2	.8724	.8624	.8289	.8445	.7817	.8242
3	.8792	.8743	.8355	.8542	.7857	.8392
4	.8845	.8798	.8375	.8587	.7798	.8504
5	.8785	.8792	.8370	.8509	.7894	.8298
6	.8763	.8782	.8313	.8470	.7822	.8183
7	.8683	.8616	.8220	.8370	.7734	.8108
8	.8616	.8667	.8149	.8360	.7734	.8043
9	.8466	.8539	.8134	.8149	.7668	.7475

TABLE C.7.a- Thickness Measurements (Y(i,j)inches) in the Straight Regions.

Δt(min)	120			240		
Region	$\overline{\Delta Y}x10^2$	$Wx10^6$	$h_d x10^5$	$\overline{\Delta Y}x10^2$	$Wx10^6$	$h_d x10^5$
A	2.97	4.12	5.94	6.11	4.24	6.11
B	3.13	4.35	6.17	6.44	4.47	6.34
C	3.30	4.58	6.34	6.57	4.56	6.31
D	3.65	5.07	6.69	7.32	5.08	6.70
E	3.68	5.11	6.57	7.49	5.20	6.69
F	3.71	5.15	6.46	7.40	5.14	6.44
G	3.74	5.19	6.33	8.42	5.85	7.14

TABLE C.7.b- Mean Thickness Differences (in), Dissolution Rates (in/s), and Mass Transfer Coefficients (m/s) in the Straight Regions.

Experiment C.7

	t (minutes)					
	0		120		240	
j \ i	1	2	1	2	1	2
1	.8844	.8802	.8339	.8566	.7796	.8429
2	.7540	.7550	.7350	.7420	.7050	.7220
3	—	—	.7260	.7260	.6840	.6850
4	.7540	.7560	.7350	.7420	.7050	.7220
5	.8829	.8790	.8381	.8569	.7901	.8305

TABLE C.7 .c- Thickness measurements ($Y_G(i,j)$ inches) in the Groove Region.

	t (minutes)					
	0		120		240	
j \ i	1	2	1	2	1	2
1	3.494	3.517	3.440	3.487	3.385	3.437
2	3.506	3.530	3.485	3.502	3.432	3.454
3	—	—	3.525	3.542	3.496	3.530
4	3.749	3.768	3.761	3.786	3.780	3.790
5	3.754	3.776	3.783	3.797	3.805	3.811

TABLE C.7 .d- Longitudinal measurements ($X_G(i,j)$ inches) in the Groove Region.

Δt (min)	120					
Sub-region	$\overline{\Delta Y} \times 10^2$	$W \times 10^6$	$h_d \times 10^5$	$\overline{\Delta Y} \times 10^2$	$W \times 10^6$	$h_d \times 10^5$
I	3.56	4.94	6.75	6.91	4.80	6.56
II	11.33	15.74	21.45	15.08	10.47	14.27
III	2.46	3.41	4.64	6.06	4.21	5.73
IV	1.63	2.26	3.07	4.13	2.87	3.90
V	11.45	15.90	21.55	13.62	9.46	12.82
VI	3.42	4.75	6.43	7.00	4.86	6.58

TABLE C.7 .e- Mean Thickness Differences (in), Dissolution Rates (in/s), and Mass Transfer Coefficients (m/s), in the Groove Region.

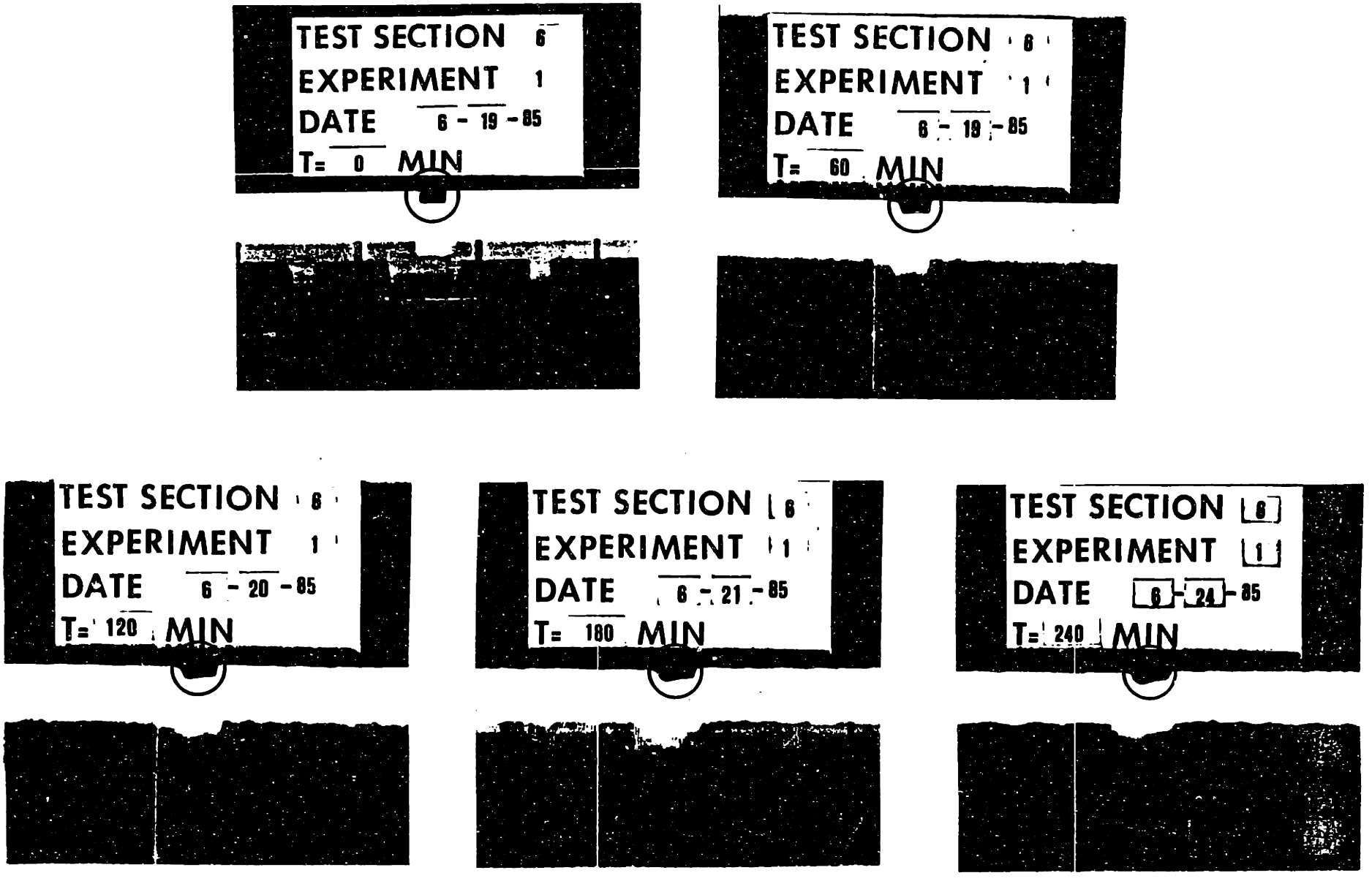

Figure C.9- Experiment 6.1 – Variation of the groove shape with time.

Experiment 8.1 - V_{air} = 125 ft/s

Q_{H_2O} = 700 ml/min

	t (minutes)					
	0		120		240	
j \ i	1	2	1	2	1	2
1	.8539	.8517	.8224	.8355	.7915	.8178
2	.8624	.8651	.8284	.8466	.7897	.8293
3	.8707	.8745	.8344	.8543	.7935	.8340
4	.8706	.8732	.8297	.8536	.7848	.8374
5	.8707	.8712	.8326	.8401	.7909	.8221
6	.8701	.8707	.8304	.8449	.7871	.8176
7	.8683	.8681	.8301	.8402	.7916	.8124
8	.8665	.8641	.8290	.8357	.7910	.8049
9	.8622	.8584	.8214	.8269	.7826	.7909

TABLE C. 8.a- Thickness Measurements (Y(i,j)inches) in the Straight Regions.

Δt(min)	120			240		
Region	$\overline{\Delta Y}x10^2$	$Wx10^6$	$h_d x10^5$	$\overline{\Delta Y}x10^2$	$Wx10^6$	$h_d x10^5$
A	3.03	4.21	6.07	6.21	4.31	6.21
B	3.25	4.52	6.41	6.88	4.78	6.78
C	3.54	4.92	6.81	7.43	5.16	7.14
D	3.72	5.16	6.81	7.65	5.31	7.00
E	3.69	5.13	6.60	7.56	5.25	6.75
F	3.63	5.04	6.32	7.30	5.07	6.35
G	3.77	5.23	6.38	7.55	5.24	6.40

TABLE C. 8.b- Mean Thickness Differences (in), Dissolution Rates (in/s), and Mass Transfer Coefficients (m/s) in the Straight Regions.

	t (minutes)					
	0		120		240	
j \ i	1	2	1	2	1	2
1	.8704	.8723	.8278	.8495	.7842	.8330
2	.7550	.7390	.7300	.7300	.7070	.7150
3	—	—	.7200	.7150	.6890	.6870
4	.7480	.7400	.7300	.7300	.7070	.7150
5	.8705	.8719	.8340	.8404	.7909	.8221

TABLE C. 8.c- Thickness measurements ($Y_G(i,j)$ inches) in the Groove Region.

	t (minutes)					
	0		120		240	
j \ i	1	2	1	2	1	2
1	3.538	3.565	3.504	3.516	3.435	3.477
2	3.545	3.577	3.525	3.548	3.501	3.522
3	—	—	3.572	3.606	3.554	3.592
4	3.771	3.812	3.809	3.831	3.828	3.840
5	3.800	3.827	3.820	3.847	3.833	3.866

TABLE C. 8.d- Longitudinal measurements ($X_G(i,j)$ inches) in the Groove Region.

Δt (min)	120			240		
Sub-region	$\overline{\Delta Y}x10^2$	$Wx10^6$	$h_d x10^5$	$\overline{\Delta Y}x10^2$	$Wx10^6$	$h_d x10^5$
I	3.83	5.32	7.27	7.80	5.42	7.40
II	11.17	15.51	21.13	12.41	8.62	11.75
III	2.82	3.91	5.32	5.64	3.92	5.33
IV	2.15	2.99	4.06	4.45	3.09	4.19
V	11.76	16.34	22.15	15.55	10.80	14.64
VI	3.63	5.04	6.82	7.47	5.19	7.02

TABLE C. 8.e- Mean Thickness Differences (in), Dissolution Rates (in/s), and Mass Transfer Coefficients (m/s), in the Groove Region.

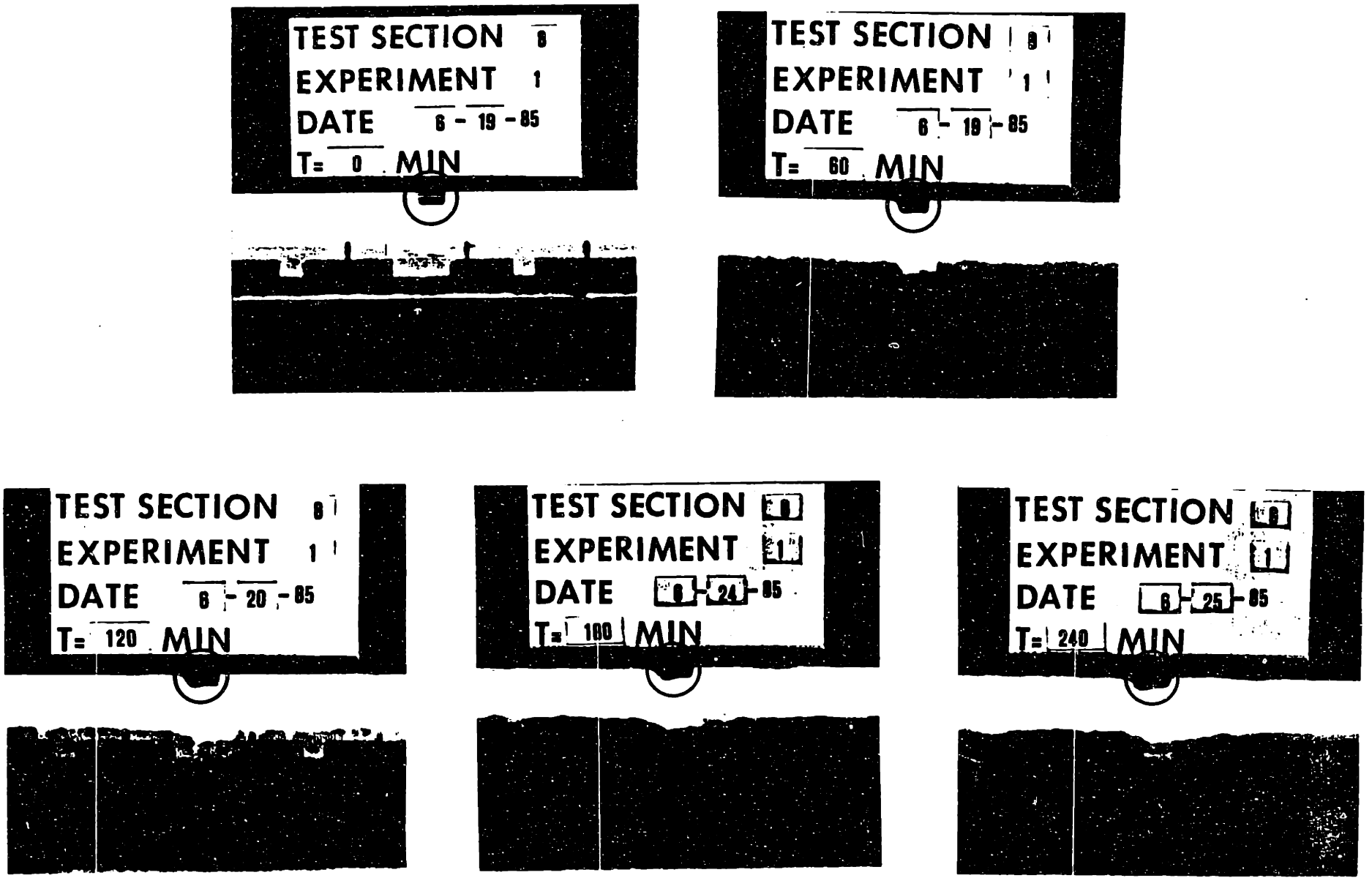

Figure C.10- Experiment 8.1 — Variation of the groove shape with time.

Experiment 9.1 - V_{air} = 125 ft/s

Q_{H_2O} = 810 ml/min

	t (minutes)					
	0		120		240	
j \ i	1	2	1	2	1	2
1	.8336	.8410	.8013	.8123	.7641	.7925
2	.8397	.8460	.7994	.8170	.7602	.7960
3	.8590	.8613	.8147	.8342	.7716	.8117
4	.8657	.8642	.8135	.8377	.7648	.8148
5	.8671	.8671	.8219	.8353	.7747	.8050
6	.8668	.8653	.8225	.8321	.7785	.8010
7	.8695	.8642	.8233	.8318	.7803	.8007
8	.8668	.8676	.8200	.8323	.7792	.8018
9	.8652	.8703	.8171	.8283	.7749	.7918

TABLE C.9.a- Thickness Measurements (Y(i,j)inches) in the Straight Regions.

Δt(min)	120			240		
Region	$\overline{\Delta Y}x10^2$	$Wx10^6$	$h_d x10^5$	$\overline{\Delta Y}x10^2$	$Wx10^6$	$h_d x10^5$
A	3.25	4.52	6.51	6.19	4.30	6.20
B	3.52	4.89	6.93	6.67	4.63	6.56
C	3.75	5.21	7.21	7.19	4.99	6.91
D	3.87	5.37	7.08	7.68	5.33	7.03
E	3.90	5.42	6.97	7.63	5.30	6.82
F	4.02	5.58	6.99	7.65	5.31	6.66
G	4.31	5.98	7.30	8.05	5.59	6.82

TABLE C.9.b- Mean Thickness Differences (in), Dissolution Rates (in/s), and Mass Transfer Coefficients (m/s) in the Straight Regions.

Experiment 9.1

	t (minutes)					
	0		120		240	
j \ i	1	2	1	2	1	2
1	.8674	.8651	.8153	.8342	.7665	.8051
2	.7400	.7400	.7230	.7200	.6950	.7080
3	—	—	.7070	.7000	.6600	.6620
4	.7420	.7300	.7230	.7200	.6950	.7080
5	.8673	.8663	.8218	.8352	.7746	.8049

TABLE C.9 .c- Thickness measurements ($Y_G(i,j)$ inches) in the Groove Region.

	t (minutes)					
	0		120		240	
j \ i	1	2	1	2	1	2
1	3.512	3.528	3.456	3.470	3.395	3.434
2	3.520	3.547	3.498	3.506	3.452	3.470
3	—	—	3.558	3.585	3.543	3.548
4	3.760	3.774	3.795	3.790	3.800	3.802
5	3.765	3.782	3.804	3.811	3.812	3.820

TABLE C.9 .d- Longitudinal measurements ($X_G(i,j)$ inches) in the Groove Region.

Δt (min)	120			240		
Sub-region	$\overline{\Delta Y}x10^2$	$Wx10^6$	$h_d x10^5$	$\overline{\Delta Y}x10^2$	$Wx10^6$	$h_d x10^5$
I	4.05	5.62	7.67	7.78	5.40	7.37
II	11.26	15.64	21.31	13.92	9.67	13.18
III	2.85	3.96	5.39	6.35	4.41	6.00
IV	1.65	2.29	3.11	3.64	2.53	3.43
V	12.69	17.62	23.88	14.85	10.31	13.97
VI	3.84	5.33	7.21	7.72	5.36	7.25

TABLE C.9 .e- Mean Thickness Differences (in), Dissolution Rates (in/s), and Mass Transfer Coefficients (m/s), in the Groove Region.

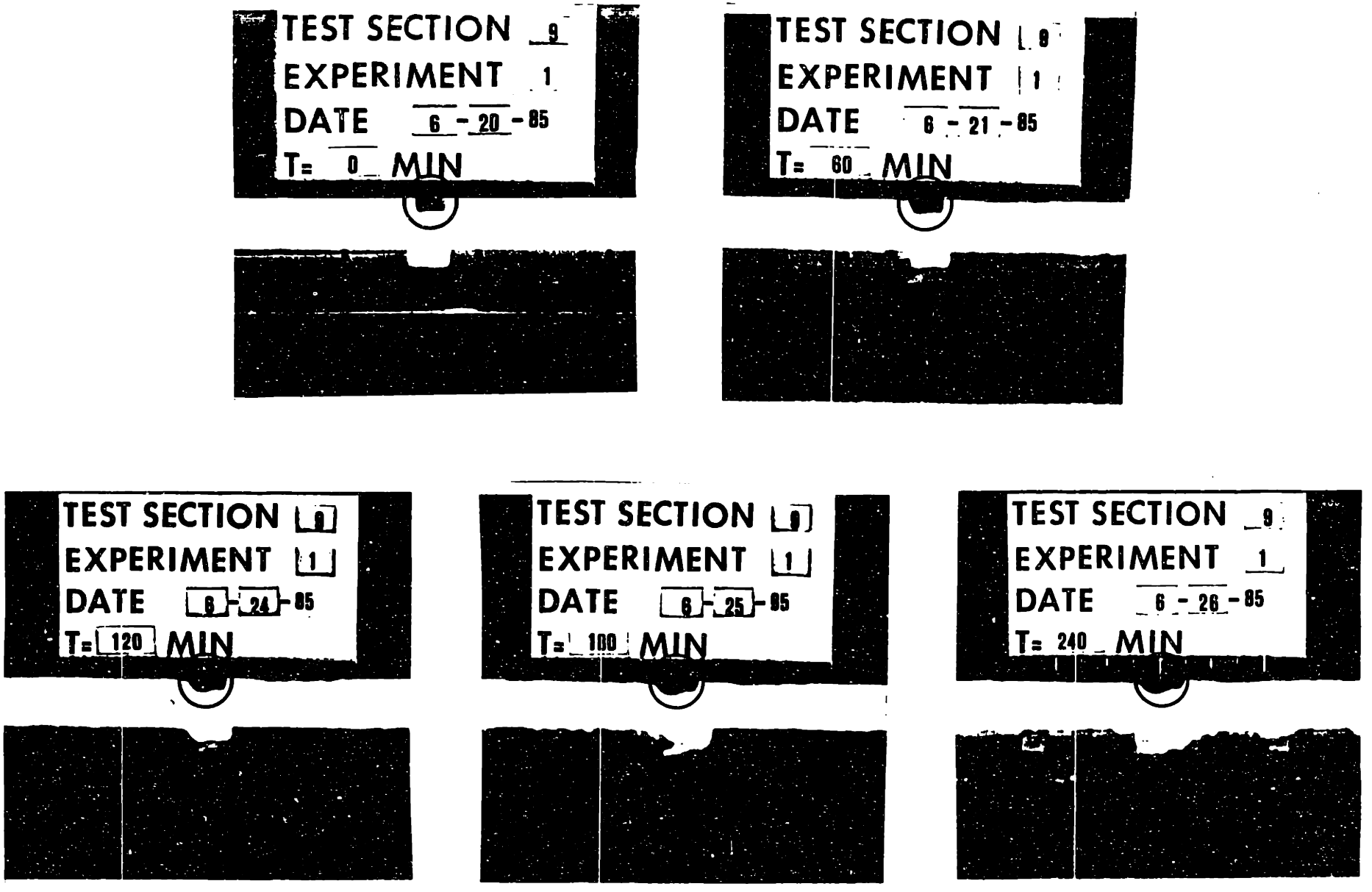

Figure C.11- Experiment 9.1 — Variation of the groove shape with time.

Experiment 10.1- V_{air} = 125 ft/s

Q_{H_2O} = 940 ml/min

	t (minutes)					
	0		120		240	
j \ i	1	2	1	2	1	2
1	.8504	.8492	.8037	.8206	.7715	.7988
2	.8683	.8594	.8134	.8322	.7705	.8082
3	.8735	.8688	.8243	.8418	.7766	.8164
4	.8739	.8689	.8189	.8454	.7705	.8171
5	.8721	.8683	.8263	.8332	.7724	.8011
6	.8703	.8663	.8224	.8294	.7710	.7987
7	.8683	.8640	.8202	.8272	.7779	.7888
8	.8658	.8635	.8181	.8244	.7768	.7893
9	.8571	.8586	.8086	.8169	.7666	.7790

TABLE C.10.a- Thickness Measurements (Y(i,j)inches) in the Straight Regions.

Δt(min)	120			240		
Region	$\overline{\Delta Y}x10^2$	$Wx10^6$	$h_d x10^5$	$\overline{\Delta Y}x10^2$	$Wx10^6$	$h_d x10^5$
A	3.94	5.47	7.88	6.96	4.83	6.96
B	3.96	5.50	7.80	7.46	5.18	7.34
C	4.08	5.66	7.44	7.62	5.29	7.32
D	4.14	5.75	7.58	8.35	5.80	7.65
E	4.24	5.89	7.58	8.31	5.77	7.42
F	4.29	5.96	7.47	8.22	5.71	7.16
G	4.43	6.15	7.51	8.31	5.77	7.04

TABLE C.10.b- Mean Thickness Differences (in), Dissolution Rates (in/s), and Mass Transfer Coefficients (m/s) in the Straight Regions.

Experiment 10.1

	t (minutes)					
	0		120		240	
j \ i	1	2	1	2	1	2
1	.8727	.8680	.8172	.8389	.7687	.8151
2	.7340	.7370	.7080	.7190	.6820	.7100
3	—	—	.6910	.6990	.6560	.6590
4	.7340	.7370	.7080	.7190	.6820	.7100
5	.8732	.8672	.8277	.8324	.7724	.8011

TABLE C.10.c- Thickness measurements ($Y_G(i,j)$ inches) in the Groove Region.

	t (minutes)					
	0		120		240	
j \ i	1	2	1	2	1	2
1	3.509	3.540	3.454	3.488	3.382	3.432
2	3.516	3.551	3.493	3.522	3.441	3.470
3	—	—	3.551	3.588	3.530	3.580
4	3.762	3.790	3.786	3.812	3.798	3.820
5	3.774	3.806	3.801	3.835	3.816	3.846

TABLE C.10.d- Longitudinal measurements ($X_G(i,j)$ inches) in the Groove Region.

Δt (min)	120			240		
Sub-region	$\overline{\Delta Y}x10^2$	$Wx10^6$	$h_d x10^5$	$\overline{\Delta Y}x10^2$	$Wx10^6$	$h_d x10^5$
I	4.08	5.66	7.73	7.80	5.42	7.40
II	11.68	16.22	22.10	14.53	10.09	13.75
III	3.43	4.77	6.49	6.49	4.51	6.14
IV	2.20	3.06	4.15	3.95	2.74	3.72
V	14.31	19.88	26.95	15.77	10.95	14.84
VI	4.03	5.60	7.58	8.35	5.80	7.85

TABLE C.10.e- Mean Thickness Differences (in), Dissolution Rates (in/s), and Mass Transfer Coefficients (m/s), in the Groove Region.

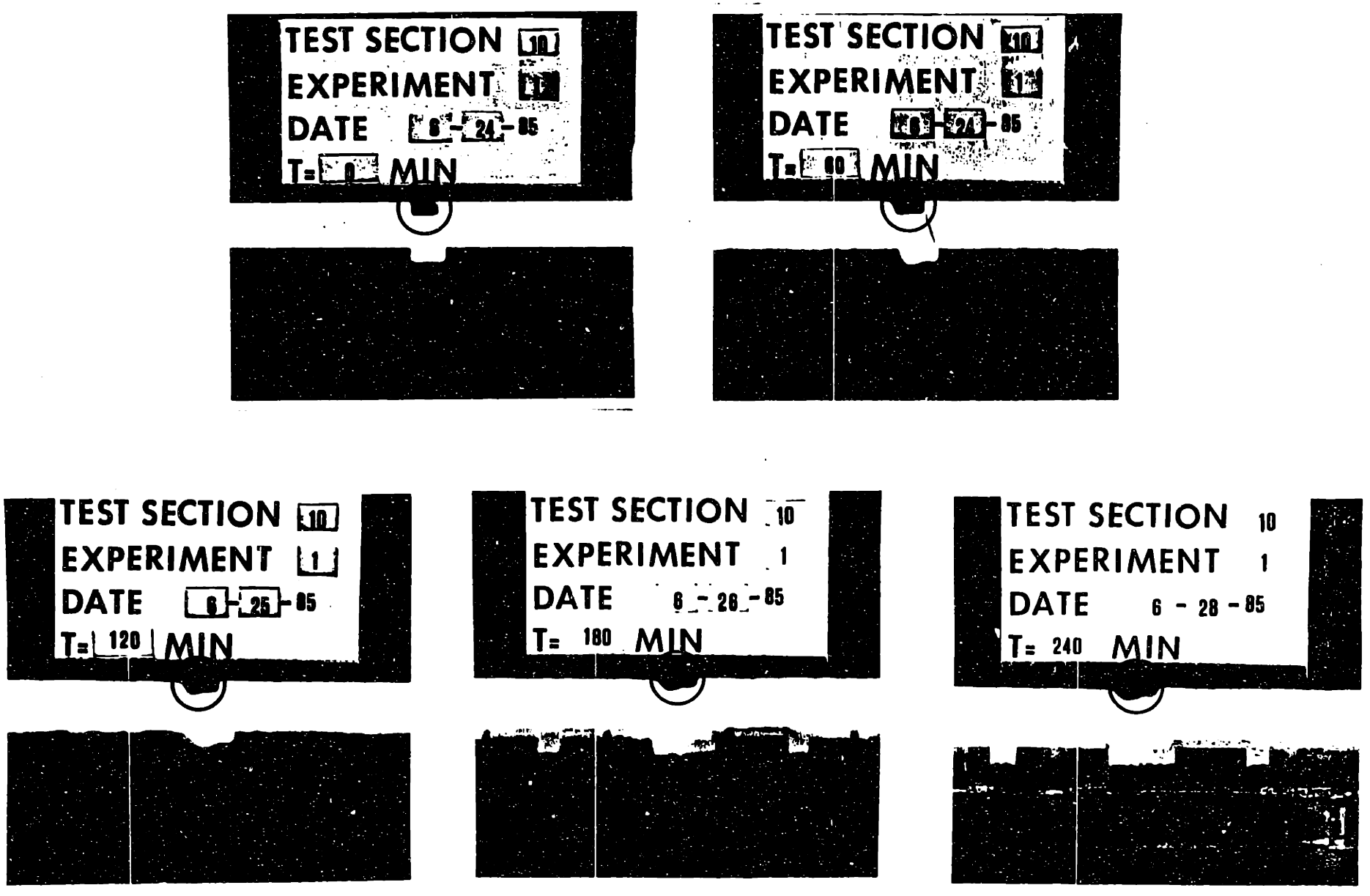

Figure C.12- Experiment 10.1 — Variation of the groove shape with time.

Experiment 1.2 - V_{air} = 150 ft/s

Q_{H_2O} = 490 ml/min

	t (minutes)					
	0		120		240	
j \ i	1	2	1	2	1	2
1	.8686	.8562	.8290	.8377	.8040	.8159
2	.8726	.8683	.8280	.8556	.8005	.8107
3	.8750	.8738	.8285	.8612	.7911	.8189
4	.8712	.8676	.8192	.8521	.7819	.8192
5	.8674	.8621	.8201	.8469	.7893	.7974
6	.8632	.8573	.8140	.8440	.7808	.8017
7	.8597	.8605	.8091	.8445	.7776	.8120
8	.8532	.8633	.8049	.8427	.7764	.8116
9	.8492	.8611	.8080	.8280	.7784	.7877

TABLE C.11.a- Thickness Measurements (Y(i,j) inches) in the Straight Regions.

Δt(min)	120			240		
Region	$\overline{\Delta Y}x10^2$	$Wx10^6$	$h_d x10^5$	$\overline{\Delta Y}x10^2$	$Wx10^6$	$h_d x10^5$
A	2.89	4.01	5.78	5.86	4.07	5.87
B	2.91	4.04	5.73	6.71	4.66	6.61
C	3.17	4.40	6.09	6.91	4.80	6.65
D	3.12	4.34	5.72	7.03	4.88	6.44
E	3.23	4.48	5.76	6.71	4.66	5.99
F	3.39	4.71	5.90	6.47	4.49	5.63
G	3.58	4.97	6.07	6.81	4.73	5.77

TABLE C.11.b- Mean Thickness Differences (in), Dissolution Rates (in/s), and Mass Transfer Coefficients (m/s) in the Straight Regions.

	t (minutes)					
	0		120		240	
j \ i	1	2	1	2	1	2
1	.8694	.8672	.8138	.8431	.7778	.8087
2	.7250	.7300	.7120	.7260	.6950	.7120
3	—	—	.6900	.7050	.6560	.6700
4	.7200	.7350	.7120	.7260	.6950	.7120
5	.8674	.8672	.8209	.8477	.7902	.7983

TABLE C.11c- Thickness measurements ($Y_G(i,j)$ inches) in the Groove Region.

	t (minutes)					
	0		120		240	
j \ i	1	2	1	2	1	2
1	3.490	3.515	3.410	3.435	3.365	3.398
2	3.501	3.521	3.471	3.493	3.412	3.445
3	—	—	3.537	3.556	3.531	3.534
4	3.736	3.765	3.755	3.775	3.761	3.785
5	3.758	3.781	3.770	3.793	3.783	3.801

TABLE C.11.d- Longitudinal measurements ($X_G(i,j)$ inches) in the Groove Region.

Δt (min)	120			240		
Sub-region	$\overline{\Delta Y} \times 10^2$	$W \times 10^6$	$h_d \times 10^5$	$\overline{\Delta Y} \times 10^2$	$W \times 10^6$	$h_d \times 10^5$
I	3.68	5.11	6.98	7.20	5.00	6.83
II	10.14	14.08	19.18	13.81	9.59	13.07
III	2.28	3.17	4.31	5.10	3.54	4.82
IV	0.85	1.18	1.60	2.40	1.67	2.27
V	13.60	18.89	25.60	16.43	11.41	15.46
VI	3.21	4.46	6.04	7.23	5.02	6.79

TABLE C.11.e- Mean Thickness Differences (in), Dissolution Rates (in/s), and Mass Transfer Coefficients (m/s), in the Groove Region.

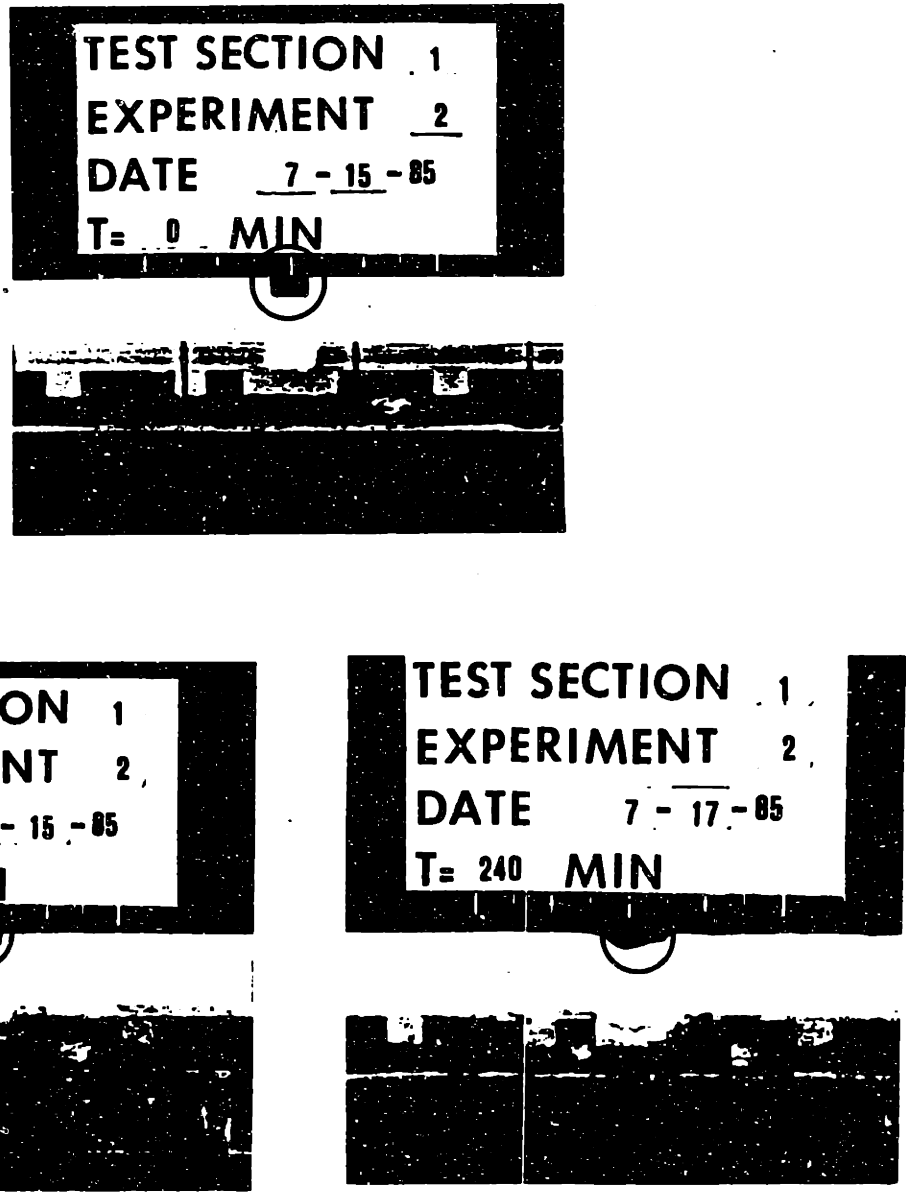

Figure C.13- Experiment 1.2 — Variation of the groove shape with time.

Experiment 2.2 - V_{air} = 150 ft/s

Q_{H_2O} = 600 ml/min

	t (minutes)					
	0		120		205	
j \ i	1	2	1	2	1	2
1	.8611	.8482	.8168	.8310	.7961	.7977
2	.8597	.8450	.8045	.8326	.7821	.7949
3	.8606	.8465	.8056	.8415	.7821	.7917
4	.8591	.8462	.7971	.8388	.7784	.7918
5	.8596	.8462	.8070	.8232	.7733	.7914
6	.8565	.8498	.8010	.8190	.7778	.7899
7	.8552	.8538	.8026	.8195	.7813	.7891
8	.8579	.8566	.8087	.8193	.7882	.7921
9	.8585	.8596	.8108	.8176	.7862	.7879

TABLE C.12a- Thickness Measurements (Y(i,j)inches) in the Straight Regions.

Δt(min)	120			205		
Region	$\overline{\Delta Y}x10^2$	$Wx10^6$	$h_d x10^5$	$\overline{\Delta Y}x10^2$	$Wx10^6$	$h_d x10^5$
A	3.23	4.48	6.46	7.11	4.94	7.12
B	3.19	4.43	6.28	7.65	5.31	7.53
C	3.23	4.49	6.22	7.86	5.46	7.56
D	4.05	5.62	7.41	8.19	5.69	7.51
E	4.33	6.01	7.73	8.11	5.63	7.24
F	4.33	6.02	7.55	8.01	5.56	6.97
G	4.41	6.12	7.47	8.14	5.65	6.90

TABLE C.12.b- Mean Thickness Differences (in), Dissolution Rates (in/s), and Mass Transfer Coefficients (m/s) in the Straight Regions.

	t (minutes)					
	0		120		205	
j \ i	1	2	1	2	1	2
1	.8603	.8471	.7915	.8337	.7721	.7888
2	.7400	.7350	.7350	.7310	.7150	.7120
3	—	—	.6980	.7010	.6690	.6680
4	.7500	.7400	.7350	.7310	.7150	.7120
5	.8596	.8462	.8070	.8232	.7733	.7914

TABLE C.12.c- Thickness measurements ($Y_G(i,j)$ inches) in the Groove Region.

	t (minutes)					
	0		120		205	
j \ i	1	2	1	2	1	2
1	3.478	3.494	3.397	3.405	3.348	3.370
2	3.482	3.494	3.450	3.462	3.391	3.406
3	—	—	3.517	3.530	3.514	3.512
4	3.721	3.745	3.732	3.750	3.737	3.755
5	3.730	3.753	3.750	3.774	3.757	3.780

TABLE C. 12d- Longitudinal measurements ($X_G(i,j)$ inches) in the Groove Region.

Δt (min)	120			205		
Sub-region	$\overline{\Delta Y}x10^2$	$Wx10^6$	$h_d x10^5$	$\overline{\Delta Y}x10^2$	$Wx10^6$	$h_d x10^5$
I	3.79	5.26	7.18	8.24	5.72	7.81
II	8.28	11.50	15.67	13.95	9.69	13.20
III	3.06	4.25	5.78	6.77	4.70	6.39
IV	0.83	1.15	1.56	3.25	2.26	3.07
V	8.36	11.61	15.74	12.12	8.42	11.41
VI	3.78	5.25	7.11	8.27	5.74	7.77

TABLE C.12.e- Mean Thickness Differences (in), Dissolution Rates (in/s), and Mass Transfer Coefficients (m/s), in the Groove Region.

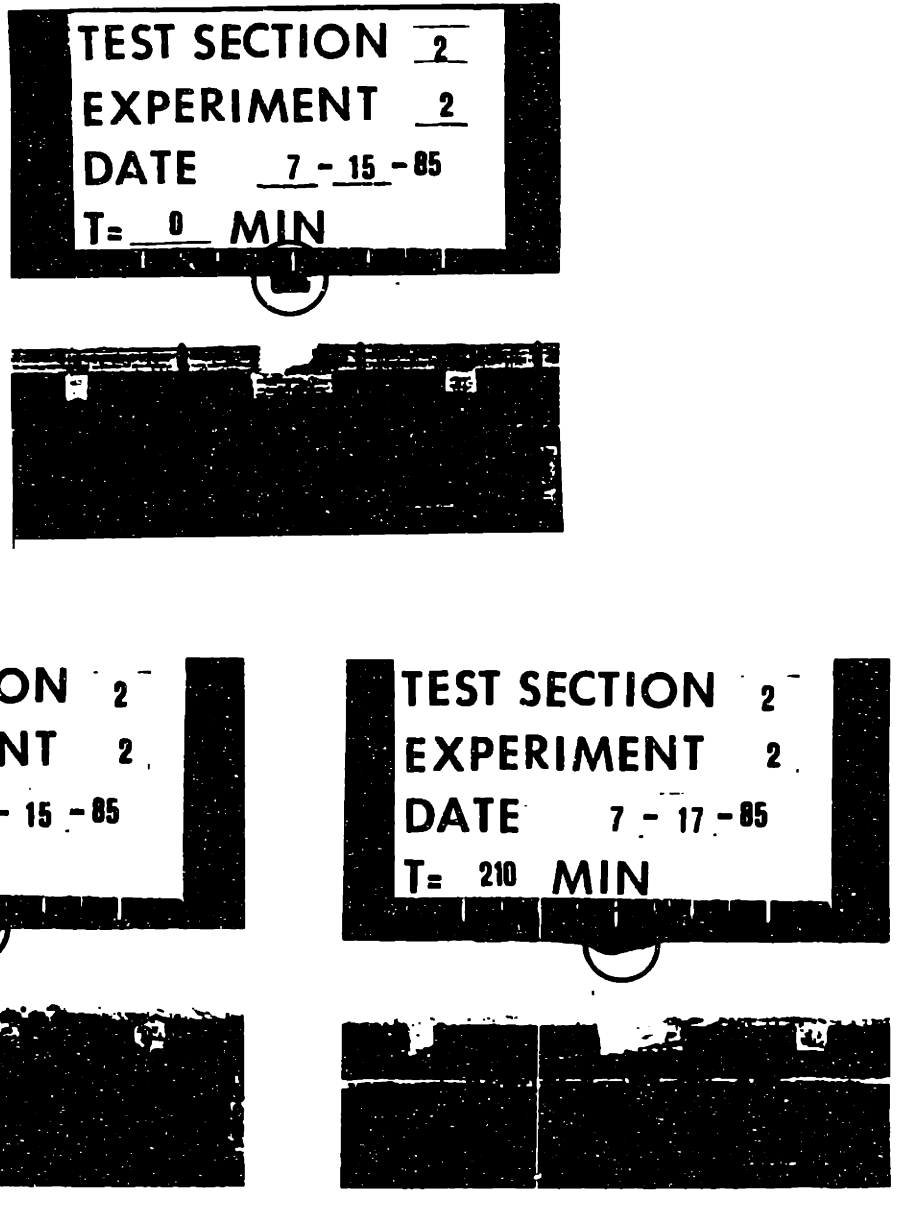

Figure C.14- Experiment 2.2 – Variation of the groove shape with time.

Experiment 3.2 - V_{air} = 150 ft/s

Q_{H_2O} = 700 ml/min

	t (minutes)					
	0		120		210	
j \ i	1	2	1	2	1	2
1	1.0078	1.0120	.9559	.9908	.9231	.9675
2	1.0028	1.0041	.9538	.9845	.9210	.9625
3	1.0015	1.0046	.9477	.9829	.9136	.9596
4	.9957	1.0013	.9377	.9826	.9052	.9512
5	.9913	.9983	.9419	.9712	.9099	.9511
6	.9894	.9977	.9363	.9586	.9071	.9453
7	.9888	.9987	.9395	.9569	.9096	.9442
8	.9934	1.0030	.9444	.9553	.9135	.9397
9	.9995	1.0047	.9573	.9471	.9247	.9194

TABLE C.13.a- Thickness Measurements (Y(i,j)inches) in the Straight Regions.

Δt(min)	120			210		
Region	$\overline{\Delta Y}x10^2$	$Wx10^6$	$h_d x10^5$	$\overline{\Delta Y}x10^2$	$Wx10^6$	$h_d x10^5$
A	3.54	4.92	7.09	7.21	5.01	7.22
B	3.60	5.00	7.09	7.33	5.09	7.21
C	3.81	5.29	7.32	7.82	5.43	7.52
D	4.22	5.86	7.73	7.52	5.22	6.89
E	4.59	6.37	8.19	7.68	5.33	6.86
F	4.69	6.52	8.17	7.91	5.49	6.88
G	4.91	6.82	8.32	8.67	6.02	7.35

TABLE C.13.b- Mean Thickness Differences (in), Dissolution Rates (in/s), and Mass Transfer Coefficients (m/s) in the Straight Regions.

	t (minutes)					
	0		120		210	
j \ i	1	2	1	2	1	2
1	.9942	1.0013	.9302	.9783	.9062	.9431
2	.8620	.8750	.8480	.8630	.8190	.8520
3	—	—	.8120	.8370	.7840	.8070
4	.8610	.8750	.8480	.8630	.8190	.8520
5	.9913	1.0024	.9425	.9718	.9106	.9518

TABLE C.13.c- Thickness measurements ($Y_G(i,j)$ inches) in the Groove Region.

	t (minutes)					
	0		120		210	
j \ i	1	2	1	2	1	2
1	3.440	3.467	3.361	3.378	3.296	3.349
2	3.448	3.469	3.402	3.423	3.348	3.399
3	—	—	3.468	3.510	3.437	3.478
4	3.694	3.713	3.702	3.721	3.703	3.723
5	3.699	3.720	3.720	3.748	3.721	3.750

TABLE C.13.d- Longitudinal measurements ($X_G(i,j)$ inches) in the Groove Region.

Δt (min)	120			210		
Sub-region	$\overline{\Delta Y}x10^2$	$Wx10^6$	$h_d x10^5$	$\overline{\Delta Y}x10^2$	$Wx10^6$	$h_d x10^5$
I	4.09	5.68	7.76	8.19	5.69	7.77
II	10.97	15.24	20.77	15.25	10.59	14.43
III	3.42	4.75	6.46	6.88	4.78	6.50
IV	1.35	1.88	2.55	3.83	2.66	3.61
V	9.40	13.06	17.70	12.63	8.77	11.89
VI	3.90	5.41	7.32	7.43	5.16	6.98

TABLE C.13e- Mean Thickness Differences (in), Dissolution Rates (in/s), and Mass Transfer Coefficients (m/s), in the Groove Region.

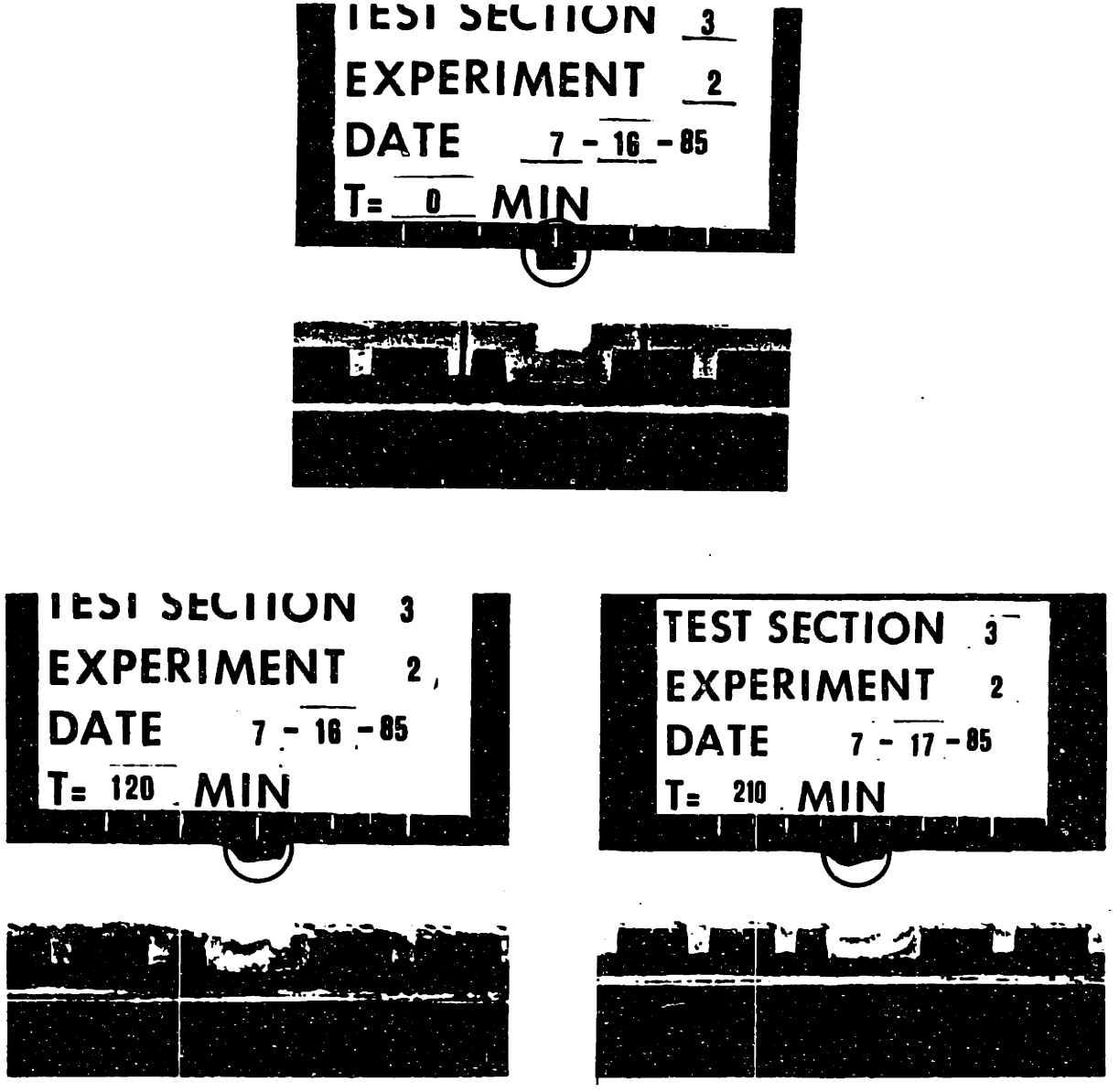

Figure C.15- Experiment 3.2 – Variation of the groove shape with time.

Experiment 4.2- V_{air} = 150 ft/s

Q_{H_2O} = 810 ml/min

	t (minutes)					
	0		120		210	
j \ i	1	2	1	2	1	2
1	.8727	.8612	.8250	.8342	.7981	.8122
2	.8722	.8691	.8190	.8401	.7801	.8166
3	.8760	.8746	.8170	.8484	.7791	.8239
4	.8822	.8757	.8163	.8462	.7741	.8241
5	.8815	.8800	.8267	.8464	.7940	.8198
6	.8838	.8843	.8246	.8442	.7856	.8302
7	.8823	.8888	.8229	.8465	.7849	.8364
8	.8777	.8897	.8191	.8481	.7881	.8327
9	.8755	.8850	.8220	.8317	.7949	.7963

TABLE C.14.a- Thickness Measurements (Y(i,j)inches) in the Straight Regions.

Δt(min)	120			210		
Region	$\overline{\Delta Y}x10^2$	$Wx10^6$	$h_d x10^5$	$\overline{\Delta Y}x10^2$	$Wx10^6$	$h_d x10^5$
A	3.92	5.45	7.85	7.66	5.32	7.67
B	4.18	5.81	8.24	8.35	5.80	8.22
C	4.51	6.27	8.68	8.78	6.10	8.45
D	4.69	6.52	8.60	8.57	5.95	7.85
E	5.04	7.00	9.00	8.63	5.99	7.70
F	5.05	7.01	8.79	8.47	5.88	7.37
G	5.08	7.05	8.61	9.03	6.27	7.65

TABLE C.14.b- Mean Thickness Differences (in), Dissolution Rates (in/s), and Mass Transfer Coefficients (m/s) in the Straight Regions.

Experiment 4.2

	t (minutes)					
	0		120		210	
j \ i	1	2	1	2	1	2
1	.8816	.8786	.8085	.8447	.7691	.8346
2	.7310	.7430	.7200	.7400	.7160	.7290
3	—	—	.6900	.7030	.6590	.6710
4	.7380	.7510	.7200	.7400	.7160	.7290
5	.8815	.8800	.8274	.8431	.7940	.8198

TABLE C.14.c- Thickness measurements ($Y_G(i,j)$ inches) in the Groove Region.

	t (minutes)					
	0		120		210	
j \ i	1	2	1	2	1	2
1	3.490	3.494	3.404	3.431	3.338	3.376
2	3.494	3.510	3.445	3.465	3.390	3.420
3	—	—	3.517	3.560	3.502	3.517
4	3.731	3.765	3.743	3.780	3.751	3.786
5	3.747	3.770	3.768	3.795	3.780	3.804

TABLE C.14.d- Longitudinal measurements ($X_G(i,j)$ inches) in the Groove Region.

Δt (min)	120			210		
Sub-region	$\overline{\Delta Y} \times 10^2$	$W \times 10^6$	$h_d \times 10^5$	$\overline{\Delta Y} \times 10^2$	$W \times 10^6$	$h_d \times 10^5$
I	5.06	7.03	9.60	9.03	6.27	8.56
II	12.27	17.04	23.22	15.51	10.77	14.67
III	3.30	4.59	6.24	6.47	4.49	6.11
IV	1.07	1.49	2.02	2.09	1.45	1.97
V	11.35	15.77	21.37	14.54	10.10	13.69
VI	4.49	6.23	8.43	8.44	5.86	7.93

TABLE C.14.e- Mean Thickness Differences (in), Dissolution Rates (in/s), and Mass Transfer Coefficients (m/s), in the Groove Region.

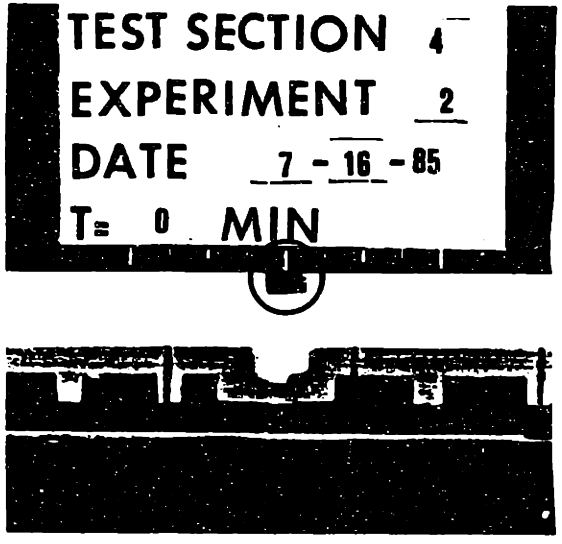

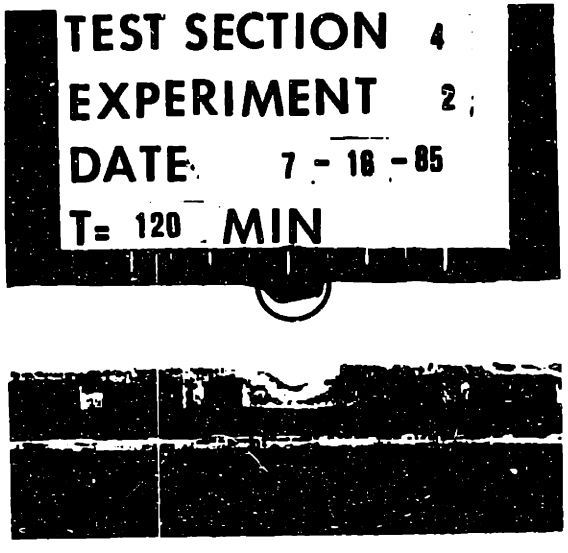

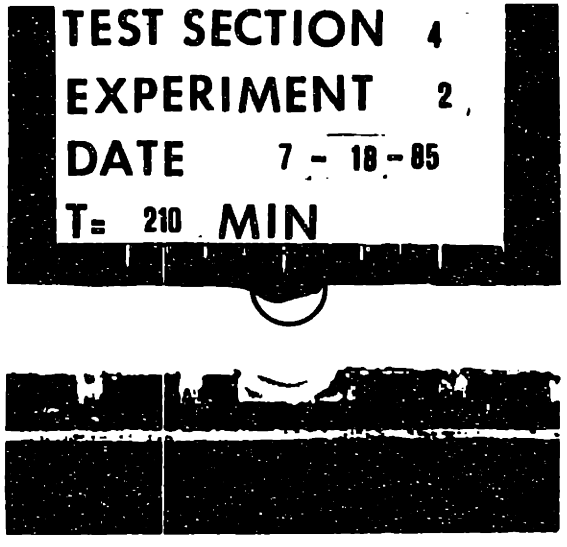

Figure C.16- Experiment 4.2 – Variation of the groove shape with time.

Experiment 5.2 - V_{air} = 150 ft/s

Q_{H_2O} = 940 ml/min

	t (minutes)					
	0		120		180	
j \ i	1	2	1	2	1	2
1	.8515	.8462	.7993	.8140	.7787	.7977
2	.8603	.8578	.7957	.8227	.7681	.8054
3	.8675	.8657	.7996	.8294	.7692	.8155
4	.8664	.8657	.7902	.8293	.7627	.8043
5	.8636	.8614	.8015	.8138	.7743	.7985
6	.8570	.8537	.7939	.8078	.7705	.7949
7	.8563	.8516	.7968	.8059	.7714	.7912
8	.8574	.8514	.7954	.8101	.7740	.7950
9	.8578	.8502	.7970	.8020	.7791	.7702

TABLE C.15.a- Thickness Measurements (Y(i,j)inches) in the Straight Regions.

Δt(min)	120			180		
Region	$\overline{\Delta Y}x10^2$	$Wx10^6$	$h_d x10^5$	$\overline{\Delta Y}x10^2$	$Wx10^6$	$h_d x10^5$
A	4.60	6.39	9.21	8.86	6.15	8.86
B	5.10	7.08	10.04	9.78	6.79	9.62
C	5.42	7.53	10.43	10.45	7.26	10.05
D	5.46	7.59	10.01	9.92	6.89	9.09
E	5.36	7.44	9.57	9.69	6.73	8.66
F	5.21	7.24	9.07	9.50	6.60	8.27
G	5.31	7.37	9.00	9.95	6.91	8.43

TABLE C.15.b- Mean Thickness Differences (in), Dissolution Rates (in/s), and Mass Transfer Coefficients (m/s) in the Straight Regions.

Experiment 5.2

	t (minutes)					
	0		120		180	
j \ i	1	2	1	2	1	2
1	.8662	.8642	.7952	.8147	.7637	.7929
2	.7200	.7220	.7090	.7140	.6980	.7040
3	—	—	.6880	.6830	.6630	.6610
4	.7200	.7250	.7090	.7140	.6980	.7040
5	.8636	.8614	.8015	.8138	.7743	.7985

TABLE C.15.c- Thickness measurements ($Y_G(i,j)$ inches) in the Groove Region.

	t (minutes)					
	0		120		180	
j \ i	1	2	1	2	1	2
1	3.543	3.563	3.468	3.478	3.406	3.440
2	3.550	3.566	3.517	3.537	3.456	3.499
3	—	—	3.574	3.608	3.548	3.585
4	3.798	3.810	3.819	3.844	3.815	3.832
5	3.813	3.821	3.842	3.853	3.849	3.859

TABLE C.15.d- Longitudinal measurements ($X_G(i,j)$ inches) in the Groove Region.

Δt (min)	120			180		
Sub-region	$\overline{\Delta Y}x10^2$	$Wx10^6$	$h_d x10^5$	$\overline{\Delta Y}x10^2$	$Wx10^6$	$h_d x10^5$
I	5.82	8.09	11.05	11.30	7.85	10.72
II	10.57	14.68	20.00	17.58	12.21	16.64
III	2.76	3.83	5.21	6.24	4.33	5.89
IV	1.02	1.42	1.93	2.76	1.96	2.61
V	13.52	18.78	22.45	16.57	11.51	15.60
VI	5.49	7.62	10.31	10.15	7.05	9.54

TABLE C.15.e- Mean Thickness Differences (in), Dissolution Rates (in/s), and Mass Transfer Coefficients (m/s), in the Groove Region.

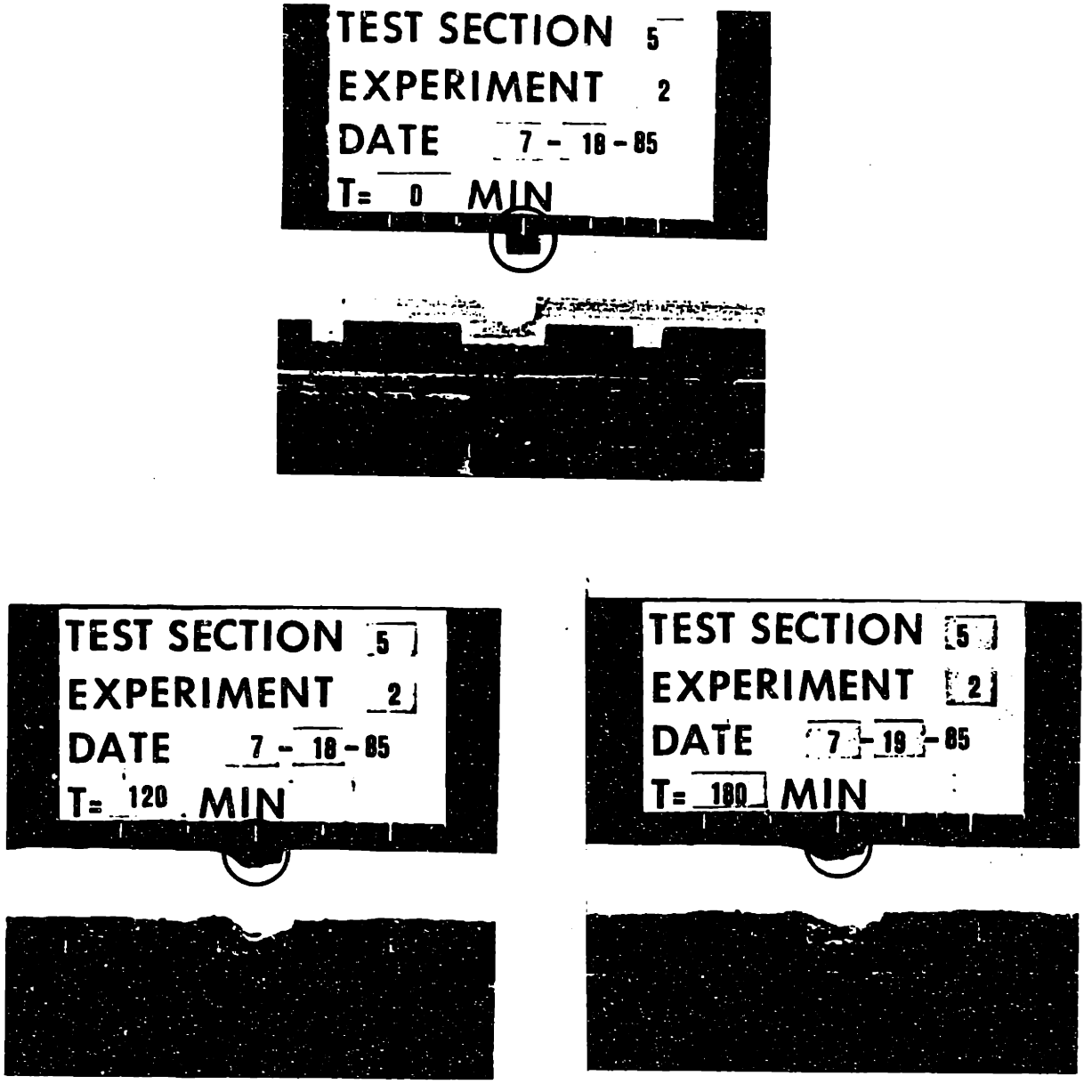

Figure C.17- Experiment 5.2 — Variation of the groove shape with time.

APPENDIX D

PLASTER MODEL FABRICATION

The test section is a plaster-of-paris plate moulded on a plexiglas base. The base is composed of three pieces of plexiglas and a rubber seal held together by round-head screws. A schematic view of the component parts of the base can be seen in Figure D.1 and the mounted test section base in Figure D.2. In order to perform the experiments, the test section is placed in the appatatus using Allen-type screws.

D.1 Preparation of the Test Section

A large amount of work was dedicated to develop a test section that could perform the required objectives. Many designs were built and tested until arriving at the actual design. The most difficult part was to cast the plaster-of-paris producing a homogeneous plate, almost free of air bubbles, because the mixture water plus calcium sulfate half-hydrate has a setting time of about ten minutes which was not sufficient to let the air bubbles escape to the surface of the material.

Initially one tried to allow the mixture to set at atmospheric conditions, without any disturbance. The resulting plate contained small bubbles, nonuniformly distributed, originating a nonhomogeneous material that could not be used for the experiments. The next step tried was to set the mixture under vacuum conditions. The result was worse than that of the first attempt: the setting time was reduced and larger voids were located inside the material.

Using the same technique tried by Blumberg [9], we added a small amount of citric acid to the mixture to delay its setting time. Since this was an empirical technique, we tried to find the best 'recipe' for our case

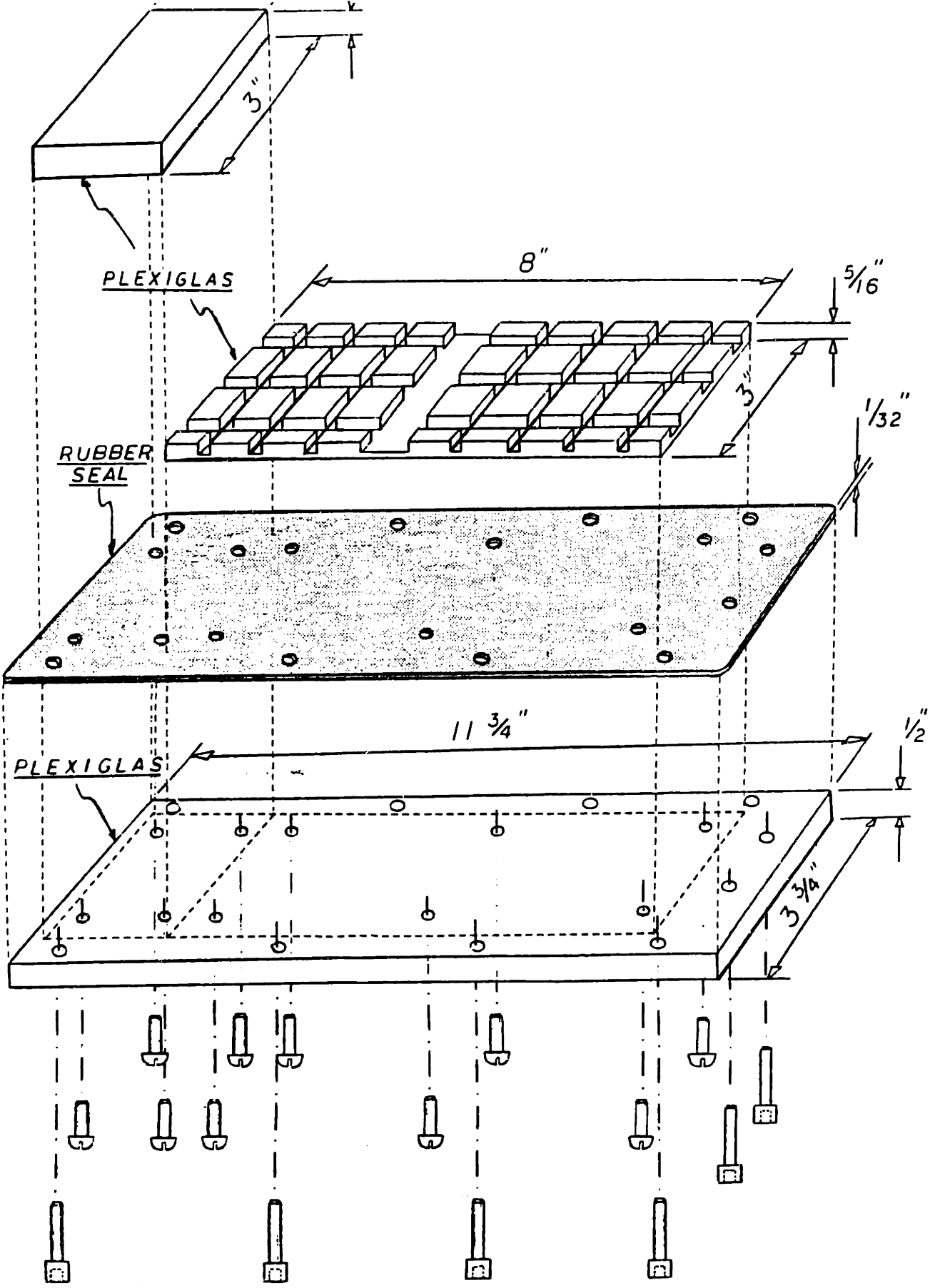

FIGURE D.1 Schematic View of the Plexiglas Base

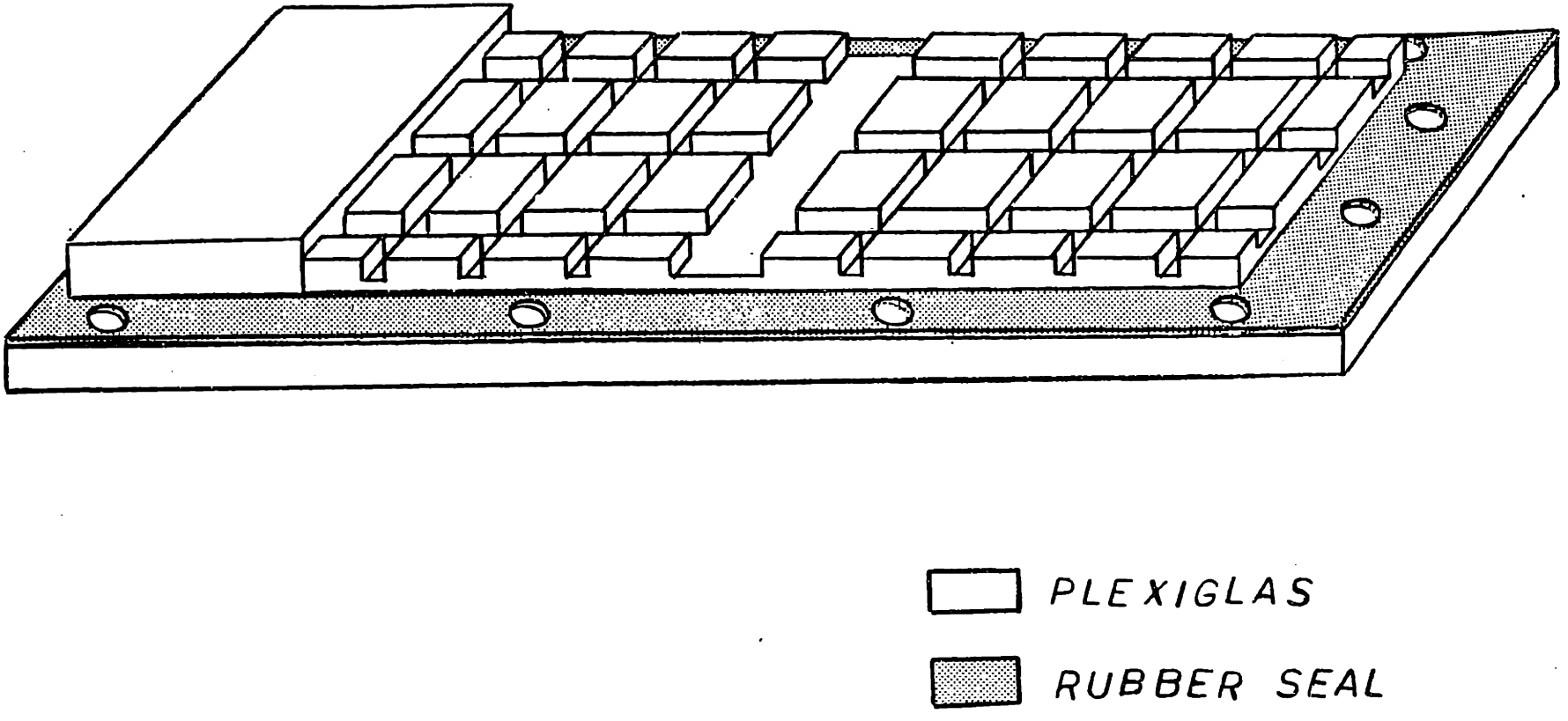

FIGURE D.2 Mounted Test Section Base

and, after a few attempts, we found a setting time of about three hours by adding 3 grams of citric acid to one liter of water used to prepare the mixture. This last setting time proved to be good enough to obtain a plaster plate with a satisfactory homogeneity to be used for dissolution rate measurements.

The plaster dissolution method used to measure dissolution rates and the further calculations to obtain the mass transfer coefficients present some advantages over other methods, such as, (1) the plaster high solubility which permits us to see a perceptible material loss in the plate after only one hour of experiment, (2) the easy and less expensive replacement of test sections that can be used in several experiments, and (3) the possibility of making measurements at any point on the plaster surface.

In our experiments we have used the DURABOND plaster-of-paris, a general purpose plaster produced by the United States Gypsum Company. The proportions used to prepare the plaster mixture were:

-200 ml of distilled water containing three parts per thousand of granular citric acid ($H_3C_6H_5O_7 \cdot H_2O$) produced by Mellinckrodt Inc.; and

-400 cm^3 of plaster-of-paris (calcium sulfate half-hydrate) powder.

To make the mixture we previously had dissolved the citric acid in the water, put the necessary amount of water in a plastic beaker, and then the plaster powder was slowly added and mixed. When the plaster was completely added to the water the components were mixed for five minutes using an impeller driven by a portable electric drill. After mixing was finished, the beaker was manually stirred for about one minute and was let to rest for five minutes in order to allow the small remaining air bubbles to escape from the material. At that point the mixture could be poured out into the mold previously placed around the plexiglas base and allowed to set

and dry for at least 24 hours at atmospheric conditions. If the local relative humidity of the air were low, the plaster surface of the test section could be prepared after those 24 hours; if not, we had to wait longer, depending on the moisture conditions.

D.2 Plaster Surface Preparation

The plaster surface preparation was made in three steps. The first one was to remove the plaster excess above the level of the mold using an electric sander until there was only about one milimeter of plaster excess. The second step consisted of removing this last one millimeter layer manually, with fine sandpaper, to get a smooth plaster surface and the required plate thickness. After this step, the mold was removed from the test section and a jig having lateral grooves was fixed over the base and around the plaster plate. In this last phase the groove was opened in the plaster using rectangular cross section files.

Appendix E

WEAR METER: PRELIMINARY DRAWINGS

The results of this work showed that it was possible to relate the mass transfer coefficient of the groove sub-regions to the average mass transfer coefficient in the straight regions of a test section. Since the local mass transfer coefficient is directly related to the local wear rate, it is plausible to suppose that we can relate the actual wear rate of a pipeline to the shape modifications in a region containing a groove.

Based on these assumptions we drafted out a preliminary drawing of a wear meter shown in Figure E.1. It is basically composed of a fixed flange (component 'A') welded on the external part of a pipeline, the 'core' of the wear meter (component 'B'), and a cover (component 'C'). These three components are held together by means of six set screws ('F'), washers ('D'), and nuts ('E'). In order to provide an adequate sealing, a flexitalic gasket ('G') is placed between parts 'A' and 'C'. To assure the correct positioning of the core 'C', whose groove must stay perpendicular to the flow direction, there is a key ('H') between components 'A' and 'B'.

The pipe external radius considered (11'), which corresponds to the curvature radius of the upper surfaces of components 'A' and 'B', is the same as the Millstone extraction line outer

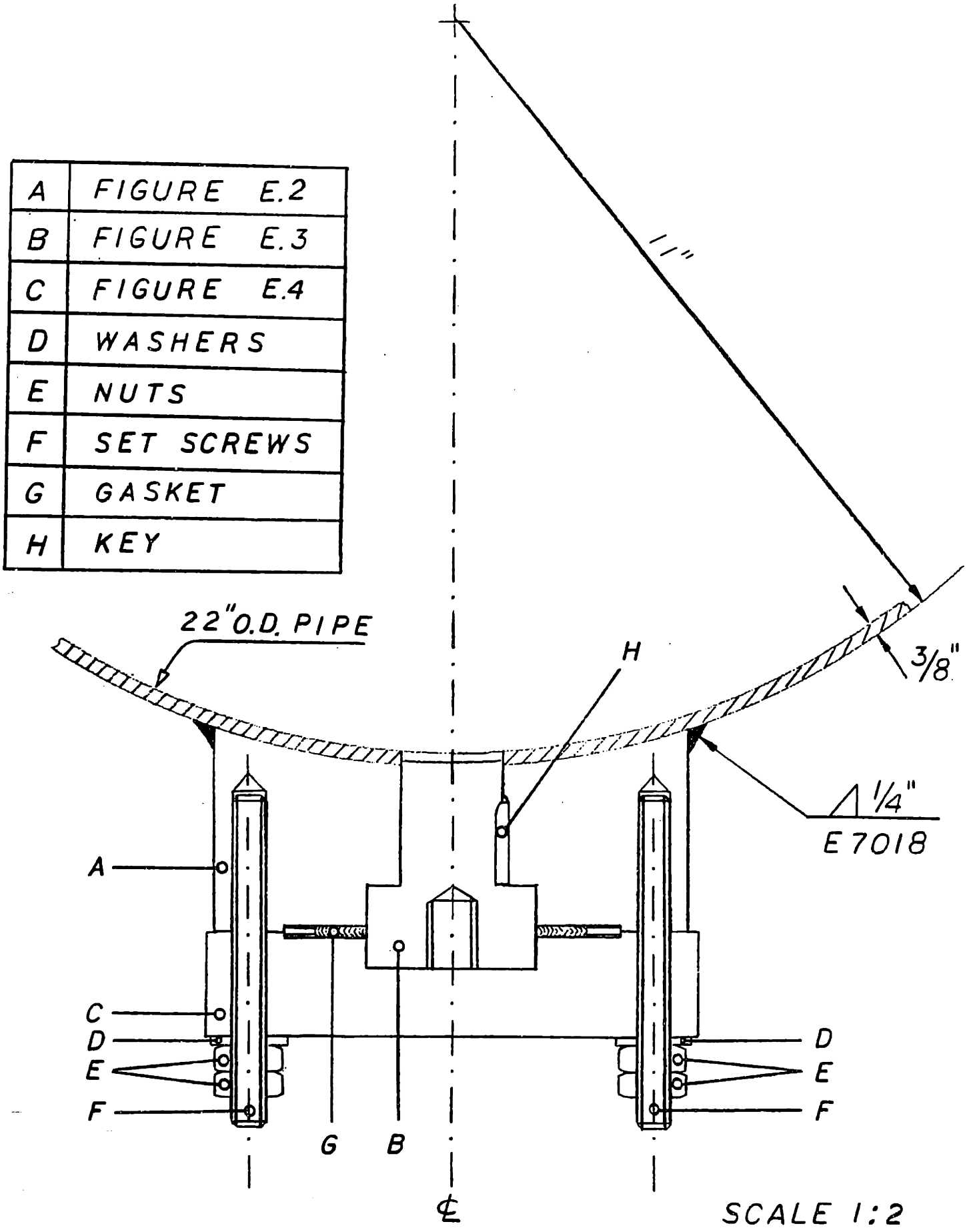

FIGURE E.1 Preliminary Drawing of a Wear Meter

radius. Preliminary drawings of components 'A', 'B' and 'C' are presented in Figures E.2, E.3 and E.4, respectively. These drawings presented are only a rough sketch of such a wear meter that can be designed, and more experiments are neccessary to extrapolate the actual wear of a pipeline from the measurements obtained with the wear meter.

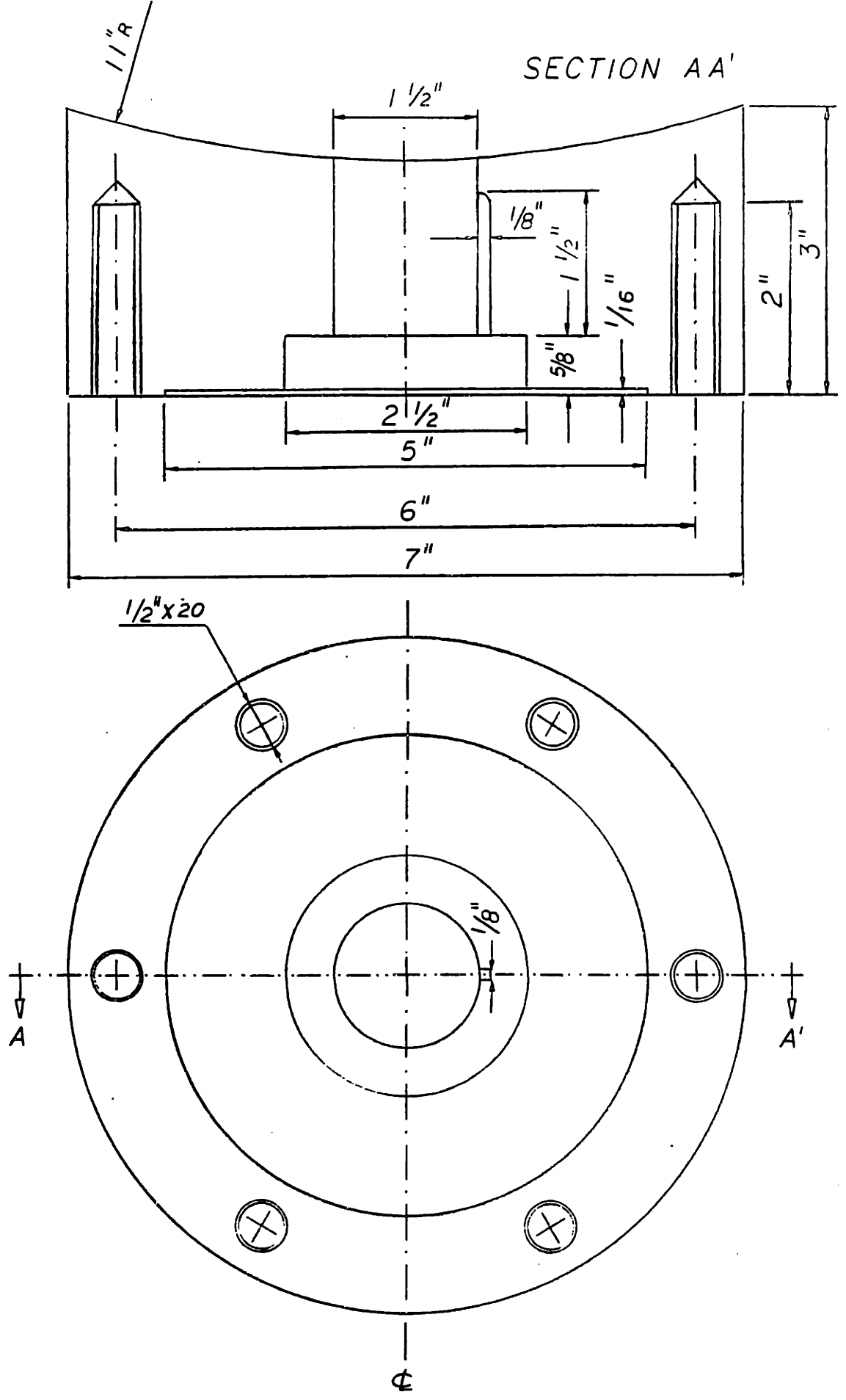

FIGURE E.2 Component 'A' (Preliminary Drawing)

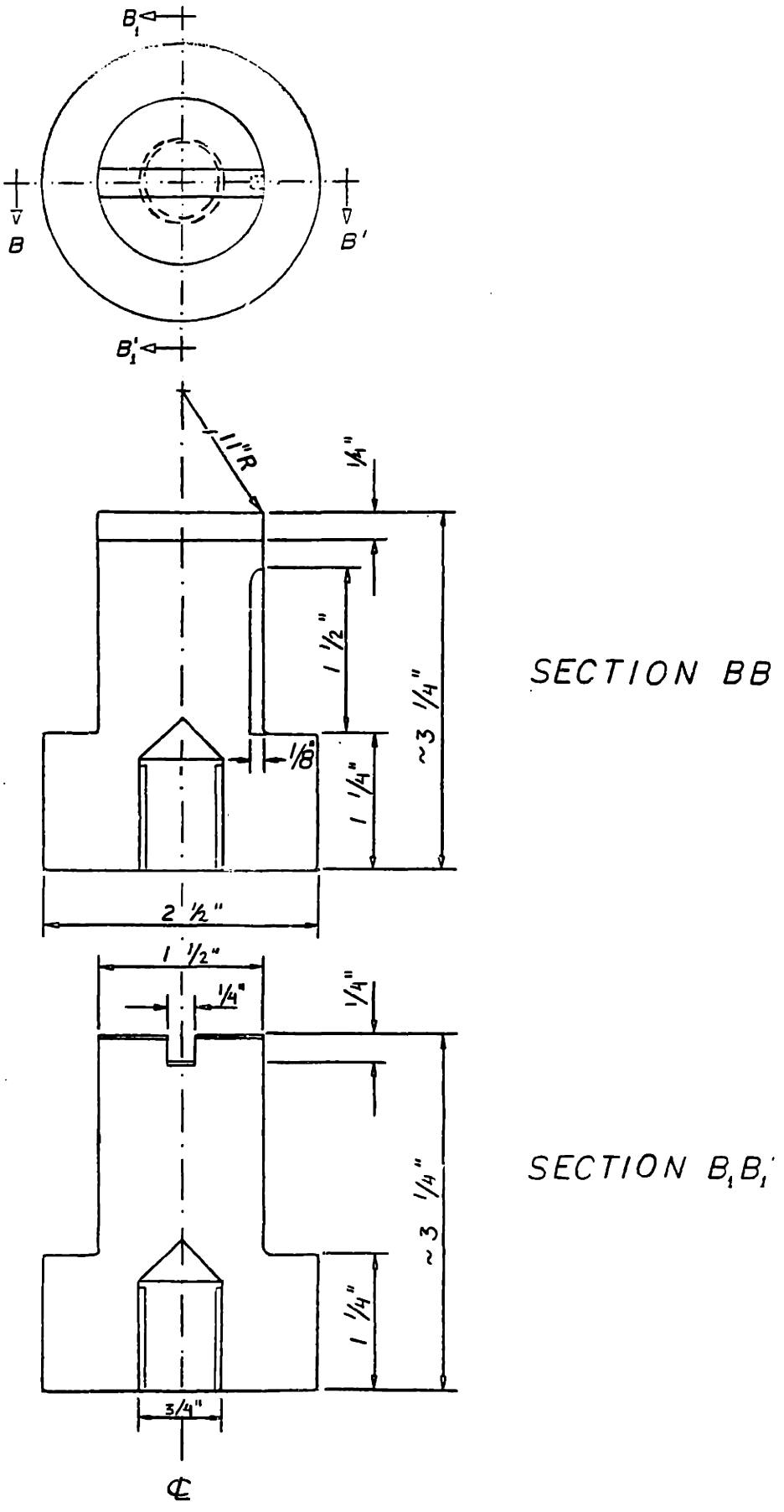

FIGURE E.3 Component 'B' (Preliminary Drawing)

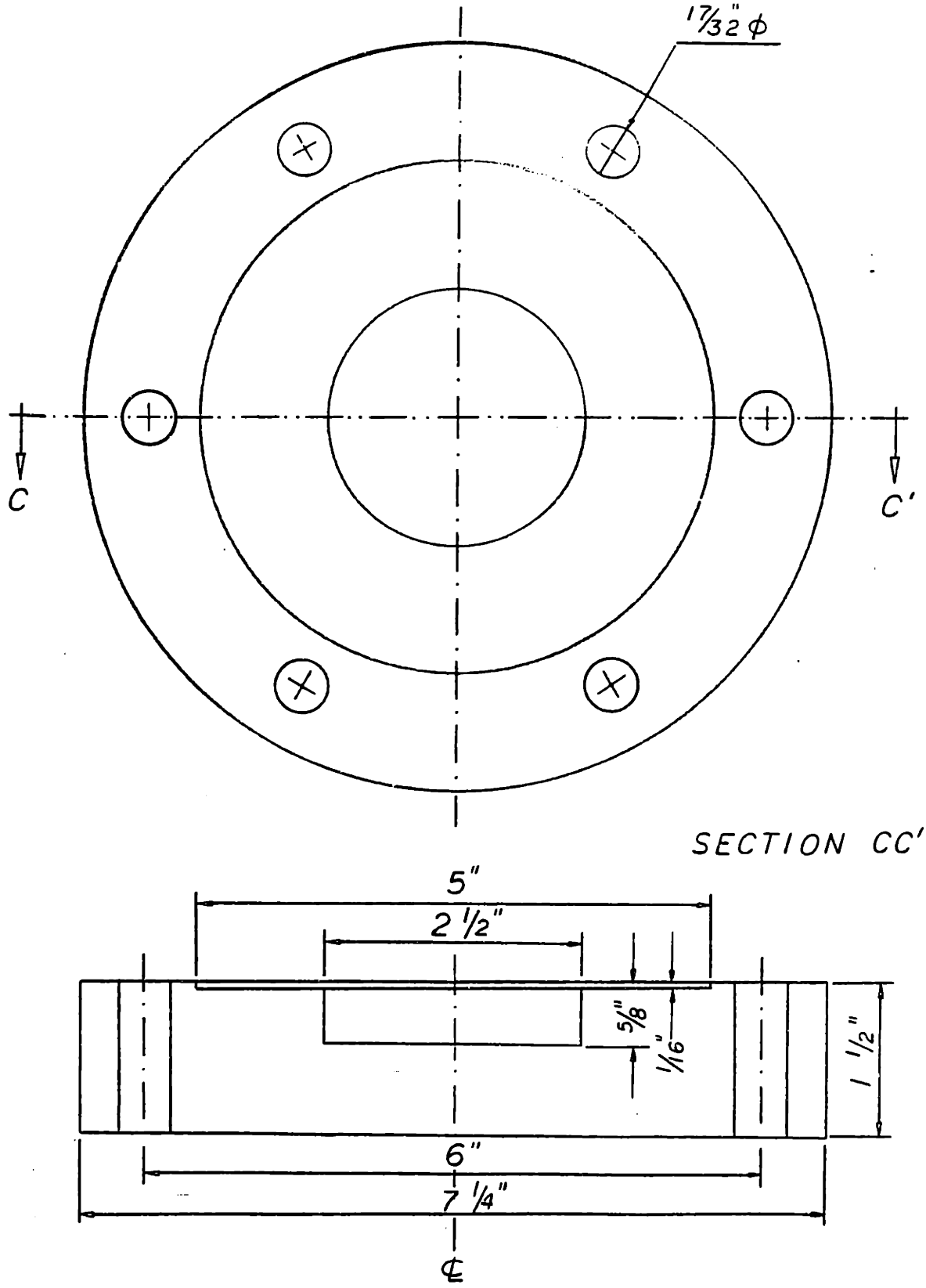

FIGURE E.4 Component 'C' (Preliminary Drawing)

References

1. Allen, J.R.L., "Note on the use of plaster of paris in flow visualization". Journal of Fluid Mech. 25 (1966) pg.331-335.

2. Allen, J.R.L.,"Transverse erosional marks of mud and rock". Sedimentary Geology 5, no. 3/4 (1971).

3. Allen, J.R.L., "Bed forms due to mass transfer in turbulent flows. Journal of Fluid Mech. 49 (1971) pg.49-63.

4. Apblett, W.R., "Prepared discussion to paper by Klapper, J.A. and Micek, W.A.". Proc. American Power Conference, 29 (1967).

5. Berger, F.P., and Hau, K.F., "Mass Transfer in turbulent pipe flow measured by electrochemical method". International Journal of Heat and Mass transfer 20 (1977) pg. 1185-1194.

6. Berkow, M.J., "The use of novel bend geometries to reduce or eliminate erosive-corrosive wear in steam extraction lines". M. Sc. thesis, M.I.T., Mech. Eng. Dept. (1984).

7. Bignold, G.J., Garbett, K., Garnsey, R., and Woolsey, J.S., "Erosion-corrosion in nuclear steam generators". 2nd International Conference on Water Chemistry of Nuclear Reactor Systems, Bounemouth (1980).

8. Bignold, G.J., Whalley, C.H., Garbett, K., Garnsey, R., Woolsey, I.S., Libaert, D.F., and Sale, R. "Erosion-corrosion of mild steel in ammoniated water". Proc. 8th International Congress on Metallic Corrosion (1981).

9. Blumberg, P.N., "Flutes: a study of stable periodic dissolution profiles". Ph.D. thesis, University of Michigan (1970).

10. Bradshaw, P., "Experimental Fluid Mechanics". London-Pergamon Press (1964) pg. 146.

11. Chenoweth, J.M. and Martin, M.W., "Turbulent two-phase flow". Petroleum Refiner, 34 (1955) pg. 151-155.

12. Collier, J.G., "Convective Boiling and Condensation". 2nd ed., McGraw-Hill International Book Co. (1971).

13. Coney, M.W.E., Wilkin, S.J., and Oates, H.S., "Thermal-hydraulic effects on mass - transfer behaviour and on erosion-corrosion metal loss rates". Specialists Meeting on Erosion-Corrosion, Les Renardieres (1982).

14. Delhaye, J.M., Giot, M., and Ruthmuller, M.L., "Thermodynamics of two-phase systems for industrial design and nuclear engineering". McGraw-Hill International Book Co. (1981).

15. Gawlik, K.M., "The determination of wear patterns in pipes conveying wet steam". B. Sc. thesis, M.I.T., Mech. Eng. Dept. (1985).

16. Griffith, P., Rabinowicz, E., Vu, H., and Sanchez-Caldera, L.E., "Erosive-corrosive wear in steam extraction lines". Progress Report, M.I.T., Mech. Eng. Dept. (1981).

17. Ishii, M., "Thermo-fluid dynamic theory of two-phase flow". Eyrolles, Paris, Scientific and Medical Publications of France, N.Y. (1975).

18. Kazimi, M.S., "Lecture Notes of course 22.312 - Engineering of Nuclear Reactors", M.I.T. (1983).

19. Keck, R.G., Griffith, P., and Rabinowicz, E., "Erosive-corrosive wear in the steam extraciton lines of power plants" - Progress Report no. 3, M.I.T., Mech. Eng. Dept. (1984).

20. Keller, H., "Erosion-corrosion in wet steam turbines". Kraftwerkstechnick, 54 (1974) pg. 292-295.

21. Keller, H., "Problems de corrosion et d'erosion dans les turbines a vapeur saturee". J. Internationales d'estudes des centrales electrique, paper no. 42 (1978).

22. Kunz, H.R. and Yerazunis, S., "An analysis of film condensation, film evaporation, and single-phase heat transfer for liquid Prandtl numbers from 10^{-3} to 10^{4} ". Journal of Heat Transfer, (1969) pg. 413-420.

23. Pak, B.G., "Prediction of maximum wear location in steam extraction lines of power plants". M. Sc. thesis, M.I.T., Mech. Eng. Dept. (1984).

24. Perry, R.H. and Chilton, C.H., "Chemical Engineers Handbook". 5th ed., McGraw-Hill, New York (1973) pg. 3.235.

25. Robinson, R.A. and Stokes, R.H., "Electrolyte Solutions". 2nd ed., Butterworths Scientific Publications, London (1959).

26. Rohsenow, W.M. and Choi, H., "Heat, Mass, and Momentum Transfer". Prentice-Hall, New Jersey (1961).

27. Sanchez-Caldera, L.E., "The mechanism of corrosion-erosion in steam extraction lines of power stations". Ph.D. thesis, M.I.T., Mech. Eng. Dept. (1984).

28. Smithsonian Physical Tables, 9th ed. Smithsonian Institution (1956).

29. Sprague, P.J., Wilkin, S.J., and Coney, M.W.E., "Effects of two-phase flow on wall to fluid mass - transfer in bends and straight pipes". European Two-Phase Flow Group Meeting, Zurich (1983).

30. Sydberger, T. and Lotz, U., "Relation between mass transfer and corrosion in a turbulent pipe flow". Journal of Electrochemical Society, February (1982) pg. 276-283.

31. Vu, H.V., "Erosive-Corrosive wear in steam-extraction lines of power plants". M. Sc. thesis, M.I.T., Mech. Eng. Dept. (1982).

32. Wallis, G.B., "One-dimensional two-phase flow". McGraw-Hill International Book Co. (1969).